

A Monte Carlo Simulation of the SLD Calorimeter
to Study the Decay of the Weak Neutral Boson

by

Eric Young

B.Sc., Université Laval, Quebec City, Que., 1985

A THESIS SUBMITTED IN PARTIAL FULFILLMENT
OF THE REQUIREMENTS FOR THE DEGREE OF
MASTER OF SCIENCE

ACCEPTED
FACULTY OF GRADUATE STUDIES

in the Department
of

Physics and Astronomy

DATE

June 13, 1985

DEAN

We accept this dissertation as conforming
to the required standard

Supervisor Dr. R.K. Keeler

Dr. A. Astbury

Dr. R. Dubois

Dr. T.W. Dingle

©ERIC YOUNG, 1988
UNIVERSITY OF VICTORIA

*All rights reserved. This dissertation may not be reproduced
in whole or in part, by xerography or other means,
without the permission of the author.*

Supervisor: Richard K. Koeler

ABSTRACT

Permission has been granted to the National Library of Canada to microfilm this thesis and to lend or sell copies of the film.

The author (copyright owner) has reserved other publication rights, and neither the thesis nor extensive extracts from it may be printed or otherwise reproduced without his/her written permission.

L'autorisation a été accordée à la Bibliothèque nationale du Canada de microfilmer cette thèse et de prêter ou de vendre des exemplaires du film.

L'auteur (titulaire du droit d'auteur) se réserve les autres droits de publication; ni la thèse ni de longs extraits de celle-ci ne doivent être imprimés ou autrement reproduits sans son autorisation écrite.

ISBN 0-315-46480-1


Dr. R.K. Koeler


Dr. A. Aubury


Dr. R. Dabois

Supervisor: Richard K. Keeler

ABSTRACT

In this thesis we present the implementation of a fast simulation code for the interaction of high energy radiation with matter. The method used is based on a parametrization of the average shape of the electromagnetic and hadronic showers and on the Monte Carlo Method. We show that the code is accurate by satisfactorily reproducing the basic characteristics of the SLD calorimeter's response to showers. Then we give some examples of the application of the code to the analysis of the decay of the weak neutral boson. We measure the angular distribution of the decay products. We show that the identification of the jet's flavour or quark's type is very difficult through an analysis of the sphericity and the aplanarity of the event. We calculate the intrinsic missing energy resolution of the detector and how well the direction of the missing energy can be used to obtain the direction of highly penetrating particles. We also discuss a method used to improve the performance of the calorimeter. This code will be extensively used for the simulation of the SLD experiment.

Examiners:



Dr. R.K. Keeler



Dr. A. Astbury



Dr. R. Dubois

Dr. T.W. Dingle

Contents

1	Introduction	1
1.1	Standard Model	2
1.1.1	Interactions	3
1.1.2	The rules	4
1.1.3	Dynamics of the interactions	8
1.2	Z^0 Physics at an e^+e^- Collider	13
1.3	Z^0 factories	18
1.4	The detection system	21
1.5	Simulation of Z^0 Physics using the SLD Detector	26
2	Shower and Calorimeters	27
2.1	Electromagnetic Interactions	27
2.2	Electromagnetic showers	33
2.2.1	Approximations	34
2.2.2	Simple Model	36
2.3	Hadronic interactions	40
2.4	Hadronic showers	42
2.4.1	'Visible' energy	44
2.5	Calorimeters	44
2.5.1	Detector response	46

2.5.2	Detector parameters	51
3	Simulation	53
3.1	Monte Carlo Method	53
3.2	Simulation environment	57
3.3	Simulation code	57
3.4	Simulation Level	59
3.5	Fast Shower Parametrization	61
1	Introduction	1
1.1	Standard Model	2
1.1.1	Interactions	3
1.1.2	The rules	4
1.1.3	Dynamics of the interactions	8
1.2	Z^0 Physics at an e^+e^- Collider	13
1.3	Z^0 factories	18
1.4	The detection system	21
1.5	Simulation of Z^0 Physics using the SLD Detector	26
2	Showers and Calorimeters	27
2.1	Electromagnetic Interactions	27
2.2	Electromagnetic showers	33
2.2.1	Approximations	34
2.2.2	Simple Model	36
2.3	Hadronic interactions	40
2.4	Hadronic showers	42
2.4.1	'Visible' energy	44
2.5	Calorimeters	44
2.5.1	Detector response	46

2.5.2	Detector parameters	51
3	Simulation	53
3.1	Monte Carlo Method	53
3.2	Computer environment	57
3.3	Simulation code	57
3.4	Simulation Level	59
3.5	Fast Shower Parametrization	61
3.5.1	Electromagnetic parametrization	62
3.5.2	Hadronic parametrization	65
3.5.3	Fluctuations	66
3.5.4	Method	68
3.5.5	Features	78
4	Results	84
4.1	Single particle results	84
4.2	e^+e^- event results	93
4.2.1	Physics analysis	93
4.2.2	Results	96
5	Conclusion	112
5.1	coupling to the Z^0	8
5.2	Diagrams showing the action of a weak charged boson exchange (a) in the leptonic sector and (b) in the quark sector	11
5.3	e^+e^- annihilation into (a) γ , (b) Z^0	13
5.4	Diagrams showing the action of a weak neutral boson exchange (a) in the leptonic sector and (b) in the quark sector	14
5.5	Clear section for the reaction $e^+e^- \rightarrow q\bar{q}$ as a function of the total center-of-mass energy.	16
5.6	Diagram of SLAC Linear Collider	19
5.7	Side view of one quadrant of SLD in the plane including the beamline	21
5.8	Top view of one quadrant of SLD in the plane including the beamline	25

List of Figures

2.1	Curves of the energy loss by collision for pions in lead.	29
2.2	(a) Relative importance for diverse processes for the electron in lead. (b) Relative importance for diverse processes for the	34
3.1	Longitudinal energy distribution of an electromagnetic shower using the function of equation 3.2.	64
1.1	Feynman diagram for the scattering of a positron and electron through (a) the t channel and (b) the s channel.	5
1.2	Gluon interactions (a) the scattering of a blue up quark off a red down quark, (b) the three-gluon vertex, (c) the four-gluon vertex.	6
1.3	Diagram for possible weak reactions. (a) The scattering of an electron neutrino via the charged current. (b) Same as the previous but through the s channel. (c) Same as the first reaction but via the neutral current. (d) Annihilation through the weak neutral boson.	7
1.4	(a) W^+ and W^- coupling to the photon. (b) W^+ and W^- coupling to the Z^0	8
1.5	Diagrams showing the action of a weak charged boson exchange (a) in the leptonic sector and (b) in the quark sector.	11
1.6	e^+e^- annihilation into (a) γ , (b) Z^0	13
1.7	Bhabha scattering also requires t-channel contributions.	14
1.8	Cross section for the reaction $e^+e^- \rightarrow q\bar{q}$ as a function of the total centre-of-mass energy.	16
1.9	Diagram of SLAC Linear Collider	19
1.10	Side view of one quadrant of SLD in the plane including the beams.	21
1.11	SLD WIC	25

2.1	Curve of the energy loss by collision for pions in lead. . . .	29
2.2	(a) Relative importance for diverse processes for the electron in lead. (b) Relative importance for diverse processes for the photon in lead.	34
3.1	Longitudinal energy distribution of an electromagnetic shower using the function of equation 3.2.	64
3.2	Flow chart of the FSP driver section of the FSP code. . . .	68
3.3	Flow chart of the shower driver section of the FSP code. . .	69
3.4	Relation between the vector and the slice plane.	70
3.5	Diagram showing a track and the shower cone along with the appropriate vectors.	71
3.6	Flow chart of the slice driver section of the FSP code. . . .	72
3.7	Figure showing relation between the unsmeared length D_j and the smeared length l_j	74
3.8	Flow chart of the ring driver section of the FSP code. . . .	75
3.9	Axial view of the cone showing how the points are put into a ring a) without smearing and b) with angle smearing. . .	77
3.10	Flow chart of the point driver section of the FSP code. . . .	78
3.11	A 5 GeV π^- simulated using the FSP code with a step size of $5 X_0$	81
3.12	Same as previous section but with no threshold and hits in inactive regions. The coil is an inactive region and is indicated in the figure.	82
3.13	A 5 GeV e^- simulated using the FSP code.	83
4.1	Calorimeter response to 5 GeV electrons.	85
4.2	Energy deposited in first layer vs energy deposited in the second layer of the electromagnetic calorimeter for 5 GeV electrons.	86

4.3	(a) Calorimeter response to 5 GeV pions. (b) $(\pi/e)^m$ as a function of the incident energy.	87
4.4	Energy deposited in the hadronic calorimeter vs the energy in the electromagnetic calorimeter for 5 GeV pions.	87
4.5	Average energy deposited in the calorimeter as a function of the kinetic energy of incoming particles for both pions and electrons.	88
4.6	Energy resolution of electromagnetic showers vs the incident energy.	89
4.7	Energy resolution of hadronic showers vs the incident energy. The line A is the resolution as measured without any cuts. The line B is calculated using the energy in the dead regions and C by using the dead regions and also by demanding an early shower and no muons from pion decay.	89
4.8	(a) Hadronic response as a function of π/e and (b) hadronic response as a function of hadronic energy fluctuations σ for 5 GeV pions. Curves denoted by a W are for a weighted energy scheme.	91
4.9	(a) Resolution as a function of π/e and (b) resolution as a function of hadronic energy fluctuations σ for 5 GeV pions. Note that for both figures the weighted curves overlap the unweighted ones.	92
4.10	(a) $(\pi/e)^m$ as a function of π/e and (b) $(\pi/e)^m$ as a function of hadronic energy fluctuations σ for 5 GeV pions.	92
4.11	A simulated $b\bar{b}$ 2-jet event in SLD showing the jet axis and the sphericity axis. One can see the energy deposited by the showers generated by the FSP code.	94
4.12	Calorimeter map showing which group of towers have energy deposited in them.	94

4.13	Angle between the sphericity axis and the event axis for leptonic final states.	97
4.14	(a) Polar angle (angle between the beam pipe and the event axis) distribution showing a $1 + \cos^2\theta$ behaviour. (b) Azimuthal angle (in the plane perpendicular to the beam axis) distribution showing a flat behaviour.	98
4.15	Plot of the missing energy in e^+e^- events. The small broadening of the spectrum comes from events in which some energy goes into the beam pipe.	99
4.16	(a) Total energy deposited in the calorimeter for the e^+e^- channel. (b) Total energy using weighting scheme.	100
4.17	(a) Total energy deposited in the calorimeter for $u\bar{u}$ 2-jet events at 93 GeV. (b) total energy deposited, corrected using the weighting scheme.	101
4.18	(a) Total energy as a function of π/e for both the weighted and unweighted schemes and for both flavours. (b) Total energy as a function of the hadronic shower fluctuations for $u\bar{u}$ events.	102
4.19	(a) Resolution of the total energy as a function of π/e for u events. (b) Resolution of the total energy as a function of the intrinsic hadronic shower fluctuations for $u\bar{u}$ for both the weighted and the unweighted schemes.	103
4.20	(a) Missing energy spectrum for up quark events. (b) Histogram of the x component of the missing energy for up quark events.	103
4.21	(a) The β parameter gets smaller as π/e ratio approaches unity. (b) β decreases with the hadronic fluctuations, which indicates that the missing energy resolution gets better with the resolution of the hadronic showers.	104

4.22 (a) The angle between the missing energy and the neutrino direction does not exhibit any correlation for $u\bar{u}$ events. (b) Same as (a) but with a 10 GeV cut on the missing energy. 105

4.23 (a) Total energy distribution for $b\bar{b}$ events. (b) Same as (a) but using the weighting correction. 106

4.24 (a) Missing energy spectrum for $b\bar{b}$ events. The solid line represents the intrinsic resolution. One can easily see the neutrino effects above the intrinsic resolution. (b) Spectrum of the x component of the missing energy vector. 106

4.25 (a) Histogram showing the angle between the missing energy and the direction of the neutrino for $b\bar{b}$ events. (b) Same as (a), but using a 10 GeV cut on the missing energy. 107

4.26 (a) Aplanarity distribution for $u\bar{u}$ events. (b) Sphericity distribution for $u\bar{u}$ events. 108

4.27 Angle between the jet axis and the reconstructed axis for $u\bar{u}$ events. 110

4.28 (a) Polar angle distribution of the sphericity axes for $u\bar{u}$ events. (b) The input (actual) distribution of the jet axes. 110

2.2 Table summarizing the dependence of the interaction on the nuclear charge of the medium. 46

3.1 List of regions implemented for the simulation. 70

4.1 Table showing the fraction of events that are within a given angle. 108

4.2 Table giving the sphericity parameters for different types of jets. 109

4.3 Table of θ_{jet-qs} values for different types of jets. 111

ACKNOWLEDGEMENTS

List of Tables

1.1	Physical properties of the fundamental fermions. From left to right the quantum number are charge, isospin, strangeness, charm, bottom, top, baryon number, weak isospin, hypercharge, spin, and finally the mass.	2
1.2	Gauge bosons and their couplings.	5
1.3	Coupling constant and branching ratio for the Z^0 decay modes, where the value $\sin^2 \theta_W = 0.22$ is assumed.	15
1.4	Summary of subsystem properties	23
1.5	LAC geometry parameters. The dimensions of the barrel and the endcap include the cryostat and the vacuum vessel.	24
2.1	Numerical value for material properties	36
2.2	Table summarizing the dependence of the interaction on the nuclear charge of the medium.	46
3.1	List of regions implemented for the simulation.	70
4.1	Table showing the fraction of events that are within a given angle.	108
4.2	Table giving the sphericity parameters for different types of jet.	109
4.3	Table of $\theta_{jet-sph}$ values for different types of jets.	111

ACKNOWLEDGEMENTS

I wish to express my sincere gratitude to Dr. Richard K. Keeler for his advice, encouragement and deliberations during the research and preparation of this thesis.

I also extend my thanks to all the people involved in the software development. In particular, Dr. Richard Dubois, for the cornerstone of this thesis and his helpful assistance, Dr. Paul Poffenberger for his support and also Dr. Anthony Waite.

I wish to acknowledge the Computer Science Centre at SLAC for the availability of their computer.

Much thanks to my wife Marlene for her constant encouragement.

1.1 Standard Model

In the standard model it is believed that there are four fundamental forces: gravity, electromagnetism, weak and strong. These forces act between fun-

damental particles with spin 1/2 that are the building blocks of matter. The elementary fermions can be divided into two groups, called

leptons and quarks. Leptons are relatively light particles that include

the electron e^- , the muon μ^- , the tau τ^- , and their associated neutrinos ν_e , ν_μ ,

ν_τ . The standard model assumes that there are 6 flavours, that is, different types of quarks: the up u , down d , strange s , charm c , bottom b and top t . In the last 20 years much progress has been made in understanding the fundamental interactions between elementary particles. The theory that describes these particles and their interactions, commonly referred to as the *Standard Model* (see [1,2,3,4,5,6]), has been largely verified by experiment. However to probe this model more deeply a new generation of high precision experiments have been planned and are being constructed. They will need large accelerator complexes and use complicated detector systems. The analysis of the data collected by these experiments will require the ability to represent the detector mathematically so that response corrections and background calculations can be made.

The work of this thesis will be a numerical simulation of one important component of one of these new detectors, a liquid argon total energy absorption counter, often referred to as a calorimeter. We will discuss the simulation of a calorimeter and present results on the predicted response of the detector. This calorimeter will be part of the SLD experiment which is being constructed to study the decay of the weak vector bosons or Z^0 's which will be produced in a new e^+e^- collider known as the Stanford Linear Collider (SLC).

In the Standard Model the fermions are grouped into families, or generations. Each member of a given generation has the same properties but a different mass. For instance, the electron e^- and the muon μ^- differ in

1.1 Standard Model

In the standard model it is believed that there are four fundamental forces: gravity, electromagnetism, weak and strong. These forces act between fundamental fermions, particles with spin $1/2$ that are the building blocks of matter. The elementary fermions can be divided into two groups, called *leptons* and *quarks*. The leptons are relatively light particles that include the electron e , the muon μ , the tau τ , and their associated neutrinos ν_e , ν_μ , ν_τ . The standard model assumes that there are 6 flavours, that is, different quarks; they are the up u , down d , strange s , charm c , bottom b and top t quark. Note that the t quark has not yet been discovered. A search for it will be conducted by SLD. In table 1.1 there is an extensive list of the

	Q^*	I_3^*	S^*	C^*	B^*	T^*	B^*	T_3^* L.H.	T_3^* R.H.	Y^* L.H.	Y^* R.H.	S	MASS (MeV)
e	-1						0	-1/2	0	-1	-2	1/2	0.511
μ	-1						0	-1/2	0	-1	-2	1/2	105.7
τ	-1						0	-1/2	0	-1	-2	1/2	1784.2
ν_e	0						0	1/2	0	-1	0	1/2	$< 46eV$
ν_μ	0						0	1/2	0	-1	0	1/2	< 0.25
ν_τ	0						0	1/2	0	-1	0	1/2	< 70
d	-1/3	-1/2	0	0	0	0	1/3	-1/2	0	1/3	-2/3	1/2	~ 100.0
u	2/3	1/2	0	0	0	0	1/3	1/2	0	1/3	4/3	1/2	~ 100.0
s	-1/3	0	-1	0	0	0	1/3	-1/2	0	1/3	-2/3	1/2	~ 300.0
c	2/3	0	0	1	0	0	1/3	1/2	0	1/3	4/3	1/2	~ 1500.0
b	-1/3	0	0	0	-1	0	1/3	-1/2	0	1/3	-2/3	1/2	~ 5000.0
t	2/3	0	0	0	0	1	1/3	1/2	0	1/3	4/3	1/2	~ 40000.0

Table 1.1: Physical properties of the fundamental fermions. From left to right the quantum number are charge, isospin, strangeness, charm, bottom, top, baryon number, weak isospin, hypercharge, spin, and finally the mass.

quantum numbers of the elementary fermions.

Each fermion has an associated antiparticle that has exactly the same mass but has the opposite additive quantum numbers; these are indicated in table 1.1 by an asterisk.

In the Standard Model the fermions are grouped into families, or generations. Each member of a given generation has the same properties but a different mass. For instance, the electron e^- and the muon μ^- differ in

mass but otherwise are largely the same. It is assumed that there are three generations of fermions

$$\begin{pmatrix} e^- \\ \nu_e \end{pmatrix}_L \begin{pmatrix} \mu^- \\ \nu_\mu \end{pmatrix}_L \begin{pmatrix} \tau^- \\ \nu_\tau \end{pmatrix}_L \quad (1.1)$$

where M is the mass of the fermion. Note that this relation agrees with relation 1.2.

$$\begin{pmatrix} u \\ d' \end{pmatrix}_L \begin{pmatrix} c \\ s' \end{pmatrix}_L \begin{pmatrix} t \\ b' \end{pmatrix}_L$$

The fermions carry different quantum numbers, which the electric charge where the particles are subgrouped into weak isospin doublets. The meaning of the L subscript and the primes will be discussed later in the chapter.

1.1.1 Interactions

In the standard model the interactions are assumed to be the result of the exchange of special *bosons*, particles with integer spin, by the fermions. While being exchanged they are called virtual bosons because neither energy nor momentum have to be conserved. In quantum mechanics the Heisenberg uncertainty relation

$$\Delta E \Delta T \geq \hbar \quad (1.2)$$

states that the measurement of the energy is always uncertain unless one takes an infinite time to measure it. In other words it is possible to violate the conservation of energy by an amount ΔE during a time ΔT . So it is possible for a fermion to emit a virtual boson without conserving energy as long as the boson is absorbed by itself or the other fermion within the time limit fixed by the uncertainty relation. Therefore the higher the energy ΔE of the virtual boson the shorter the time it can live without being absorbed. Furthermore, assuming that the virtual boson propagates at the speed of light, then the lower the energy of the virtual boson the further it can go. So if the boson is massless the amount of energy transfer can be infinitesimally

small and therefore the range of the interaction is infinite. It was Yukawa who introduced this idea. He showed that if one generalises the relativistic wave equation for a massive particle then the field corresponding to the particle has a finite range, given by

$$R = \frac{\hbar}{Mc}, \quad (1.3)$$

where M is the mass of the exchange quanta. Note that this relation agrees with relation 1.2.

The fermions carry different kinds of charge, of which the electric charge is one example, each type of charge being associated with one of the interactions. The electric charge, for example, corresponds to electromagnetism. There are also the mass, weak charge and colour corresponding to gravity, weak and strong interactions, respectively. The exchange bosons couple to the charges, that is to say they can interact with any particle, fermion or boson, that has the right charge. The standard model is the set of rules as to which charges are carried by which fermions and which bosons can couple to which charge. It is not a complete theory in the sense that it needs some input from experiments. That is, the model does not predict these rules nor does it predict the absolute strength of the couplings. However it does give some relations between the coupling of the weak and the electromagnetic interaction. The bosons for the four interactions are given in table 1.2 with their corresponding charge, strength, spin and range.

1.1.2 The rules

We will now discuss in more detail each interaction and its associated rules. As a general comment one can note that the bosons of a given interaction only couple to the charge of the interaction. Gravity is very weak (see table 1.2) and is negligible at the elementary particle level.

The boson exchanged in the electromagnetic interaction is the photon. It is massless, corresponding to a force with an infinite range. It couples

	Interaction	spin	range (cm)	mass (GeV)	coupling	value
graviton	gravity	2	∞	0	G	0.53×10^{-38}
photon	electro.	1	∞	0	$e^2/4\pi\hbar c$	1/137
Z^0, W^\pm	weak	1	10^{-16}	93	$g^2/4\pi\hbar c$	1.02×10^{-5}
gluons (8)	strong	1	10^{-13}	0	α_s	~ 1

Table 1.2: Gauge bosons and their couplings.

to the normal electric charge. It is useful to represent the interaction by Feynman diagrams [2]. Two characteristic diagrams for the electromagnetic interaction are shown in figure 1.1. The scattering through the s channel

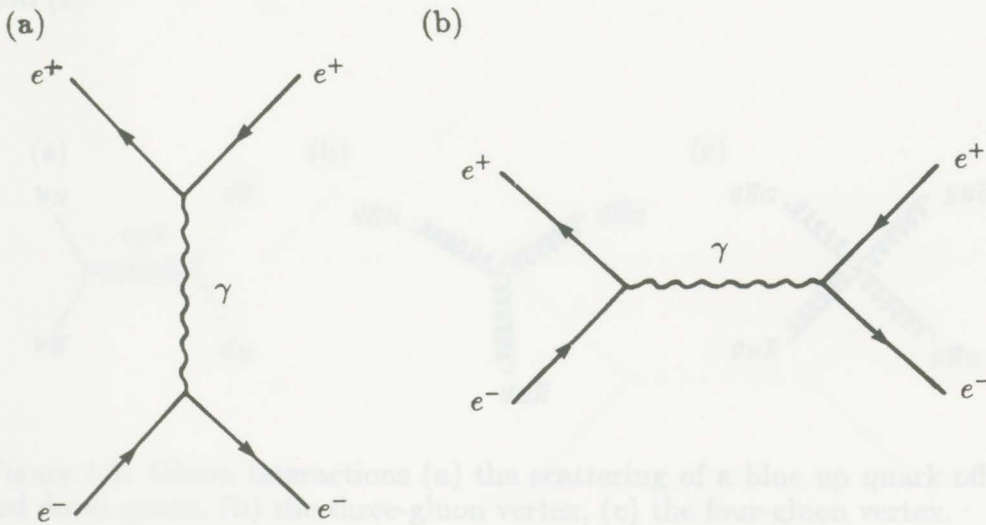


Figure 1.1: Feynman diagram for the scattering of a positron and electron through (a) the t channel and (b) the s channel.

is called annihilation, that is when a particle interacts with its antiparticle and both particles disappear into a boson.

The exchange bosons for the strong interaction are called gluons as shown in figure 1.2(a). The figure shows the scattering of a blue down quark from a red down quark. They are also massless so that the fundamental strong interaction has an infinite range. The charge is called colour; there are three different colours called red (R), blue (B), green (G) and their anticolours: antired (\bar{R}), antiblue (\bar{B}), antigreen (\bar{G}). The strong or

nuclear force we are familiar with acts between hadrons (i.e. colourless objects, either $R + G + B$ or a colour plus its anticolour) by what appears to be exchange mesons. It is now thought to be the residual strong force acting between the constituents of the hadrons, similar to the residual electromagnetic force or Van der Waals force between molecules. The range of the strong nuclear force is finite and is of the order of a hadron radius, that is about 10^{-13} cm. Colour is carried only by the quarks and the gluons. The fact that the gluon carries colour allows the gluon to couple to other gluons by the three-gluon and four-gluon vertex, as shown in figure 1.2(b) and (c).

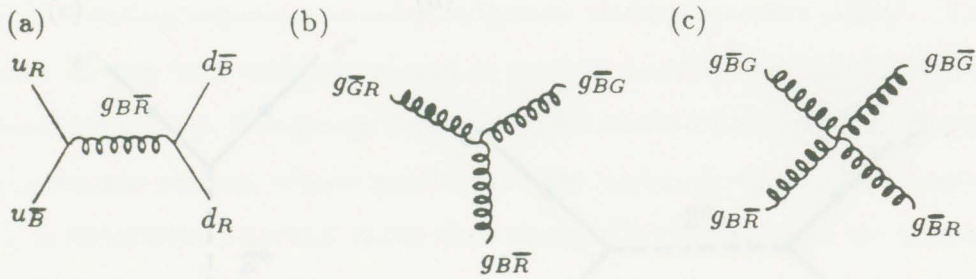


Figure 1.2: Gluon interactions (a) the scattering of a blue up quark off a red down quark, (b) the three-gluon vertex, (c) the four-gluon vertex.

The exchange bosons W^\pm and Z^0 for the weak interaction are massive, $M_{W^\pm} \sim 83$ GeV and $M_{Z^0} \sim 93$ GeV [7], and therefore the range is finite 10^{-16} cm. The weak charge is carried by all the fermions and by the weak bosons. Figure 1.3 shows 4 possible weak interactions via the weak exchange bosons. Furthermore since the W^\pm bosons are electrically charged they also couple to γ as shown in figure 1.4(a) and because the bosons carry the weak charge too it is possible for the Z^0 to couple directly to the W^\pm , as shown in figure 1.4(b).

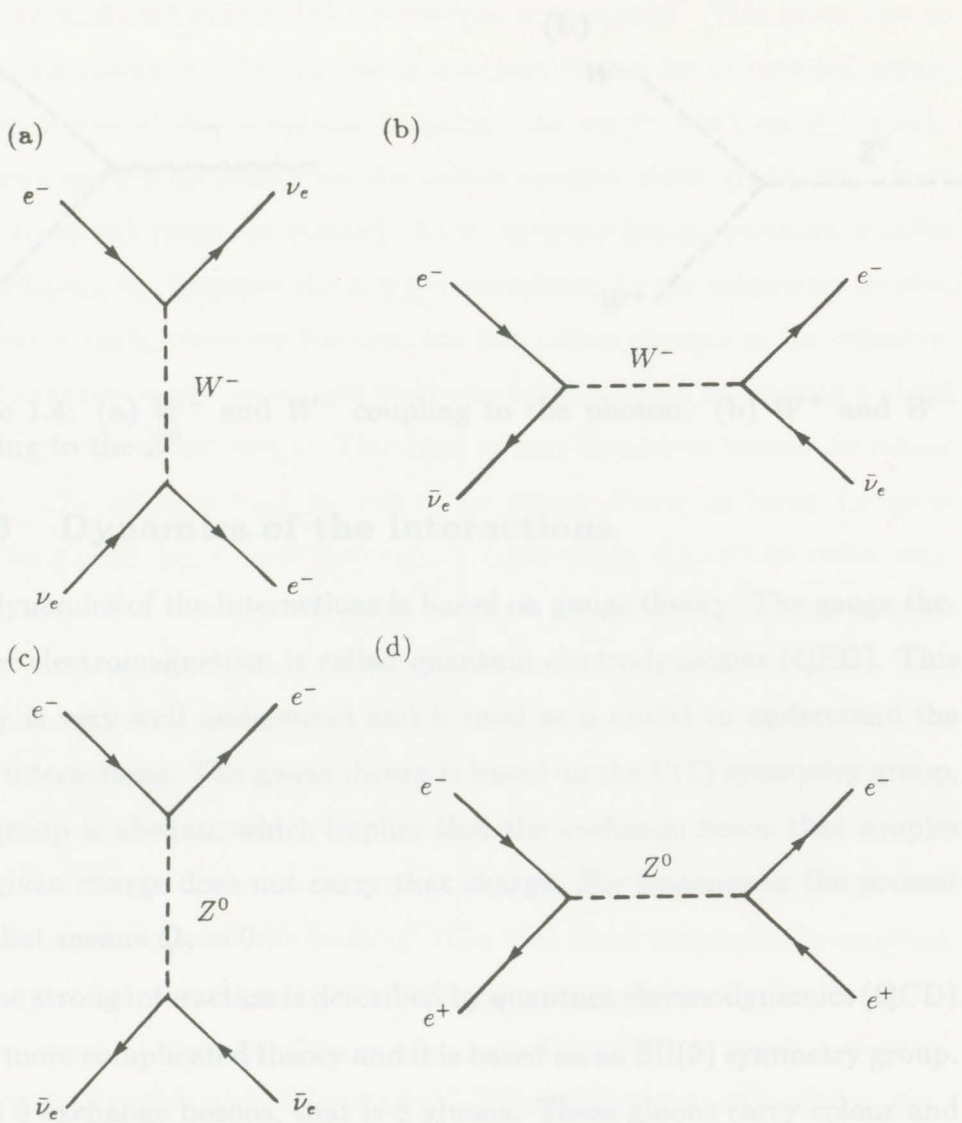


Figure 1.3: Diagram for possible weak reactions. (a) The scattering of an electron neutrino via the charged current. (b) Same as the previous but through the s channel. (c) Same as the first reaction but via the neutral current. (d) Annihilation through the weak neutral boson.

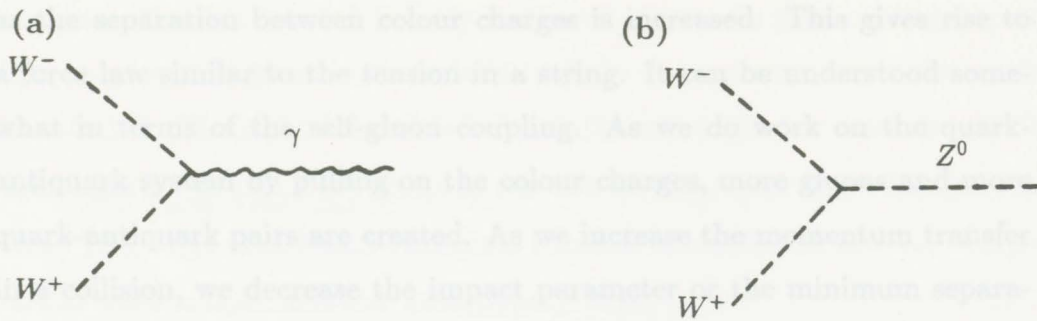


Figure 1.4: (a) W^+ and W^- coupling to the photon. (b) W^+ and W^- coupling to the Z^0 .

1.1.3 Dynamics of the interactions

The dynamics of the interactions is based on gauge theory. The gauge theory for electromagnetism is called quantum electrodynamics (QED). This theory is very well understood and is used as a model to understand the other interactions. The gauge theory is based on the $U(1)$ symmetry group. The group is abelian, which implies that the exchange boson that couples to a given charge does not carry that charge. For instance in the present case that means $Q_\gamma = 0$.

The strong interaction is described by quantum chromodynamics (QCD). It is a more complicated theory and it is based on an $SU(3)$ symmetry group. It has 8 exchange bosons, that is 8 gluons. These gluons carry colour and as mentioned above can couple to themselves via the three-gluon and four-gluon vertex; the theory is therefore non-abelian. This characteristic can be related to the fact that free quarks have never been observed. It is thought to be responsible for making the coupling constant of the strong interaction large, ~ 1 , implying one cannot use the usual methods of perturbation theory. However the strong coupling constant varies with the momentum transfer in the interaction, its value gets smaller for harder impacts, that is for small distance, and conversely the strong force increases its strength

as the separation between colour charges is increased. This gives rise to a force law similar to the tension in a string. It can be understood somewhat in terms of the self-gluon coupling. As we do work on the quark-antiquark system by pulling on the colour charges, more gluons and more quark-antiquark pairs are created. As we increase the momentum transfer in a collision, we decrease the impact parameter or the minimum separation that is being observed between the two colour charges in the collision. The gluons and quark-antiquark pairs can be thought of as forming a cloud about the bare colour charge. The effect of that cloud is to screen the colour charge. The $q\bar{q}$ pairs tend to reduce the colour charge at large distances while the gluons, because of their colour, could affect the system either way. For theories with less than 16 quark flavours, detailed calculations [2] indicate that the gluons act to increase the colour charge with distance. This effect is larger than the $q\bar{q}$ screening. Therefore as one probes the hadrons at smaller distances one sees a reduced colour charge. This is equivalent to a reduced coupling constant for higher momentum transfer.

This 'running' of the coupling constant is associated with the confinement of the quark inside the hadron. That is at small distances the coupling is very weak but as the quark tries to escape a hadron the coupling increases and the quark is trapped. The quarks are said to be free inside a hadron. This confinement is related to jets, or collimated bunches of particles, produced in a hard collision. The jets arise from the hadronization of the quark antiquark system. After the collision the quarks are moving apart and the work done on the system gets large enough to create new $q\bar{q}$ pairs moving in about the same direction as the initial partons [8]. It has been demonstrated that there are jets in final states of the e^+e^- annihilation at high-energy [9].

Finally, the weak interaction theory is based on a $SU(2)\times U(1)$ symmetry, and it is non-abelian. The $SU(2)$ group is associated with the weak

isospin. The left-handed helicity states of all the fermions are grouped into the doublets given in the relation 1.1, i.e. representations of the weak isospin 1/2. The right-handed helicity states are singlets or weak isospin 0 (see table 1.1). The U(1) group is associated with weak hypercharge (see table 1.1). The Gell-Mann-Nishijima relation connects the electric charge to the weak isospin and the weak hypercharge,

$$eQ = e(T_3 + Y/2) \quad (1.4)$$

where Q is the electric charge in units of e , T_3 is the third component of weak isospin and Y is the hypercharge.

Local gauge invariance would imply a total of four gauge bosons, three from the SU(2) part (W^+ , W^0 , W^-) and one from the U(1) part (B^0). The two neutral gauge bosons are a mixture of weak and electromagnetic fields. This was resolved by the ‘‘Higg’s mechanism’’, a process where the manifestly broken symmetry of SU(2) (the electron and neutrino have very different masses) is introduced. The net effect of these calculations is to introduce a linear combination of the W^0 and B^0

$$A^0 = g'W^0 + gB^0, \quad (1.5)$$

that is a massless vector particle which is identified as the photon. Writing the ratio of g and g' as

$$\tan \theta_W = \frac{g'}{g} \quad (1.6)$$

or

$$\cos \theta_W = \frac{g}{\sqrt{g^2 + g'^2}} \quad (1.7)$$

$$\sin \theta_W = \frac{g'}{\sqrt{g^2 + g'^2}} \quad (1.8)$$

where θ_W is called the Weinberg angle, the electromagnetic field 1.5 can now be written as

$$A^0 = W^0 \sin \theta_W + B^0 \cos \theta_W. \quad (1.9)$$

The orthogonal combination to this is the Z^0 , the neutral component of the weak bosons

$$Z^0 = W^0 \cos \theta_W + B^0 \sin \theta_W. \quad (1.10)$$

Detailed calculations let one express the connection between g , the weak coupling constant, and e , the electromagnetic coupling constant, as

$$e = g \sin \theta_W. \quad (1.11)$$

Note that θ_W is not given by the theory and therefore needs to be measured.

The action of the weak charged boson is to raise or lower the third component of the weak isospin. For example in figure 1.5 one has the transformation of a neutrino into an electron by the emission of a W^- and the decay of an u quark into a d quark via a W^+ . It is an observed

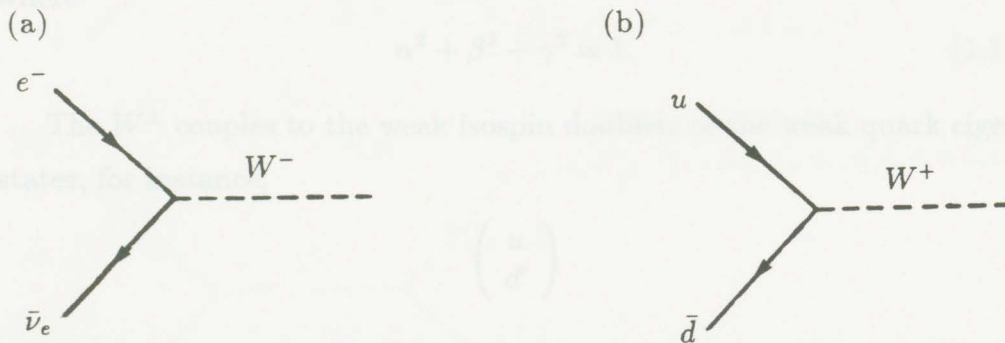


Figure 1.5: Diagrams showing the action of a weak charged boson exchange (a) in the leptonic sector and (b) in the quark sector.

fact that there is no right-handed neutrino and equivalently that weak interactions break parity. This can be expressed by saying that the weak charged current only couples to the left-handed fermions. That is to say that the right-handed fermions are weak isospin singlets. The exchange of

the W^\pm boson can be thought of as a current, which in relativistic quantum mechanics can be characterized by how they transform under parity. The observed parity breaking of the charged weak currents (i.e. W^\pm) is V-A or vector minus pseudovector.

The Z^0 couples to fermion-antifermion pairs and therefore does not couple only to the isospin doublets. This results in a complicated transformation under parity that is an admixture of V and A depending on the weak isospin and charge of the particles.

There is one further complication to the weak interactions when applied to quarks. The eigenstates of the weak interaction are not the same as the mass eigenstates of the quarks but rather a linear combination. The quark flavours are eigenstates of the mass. In relation 1.1, recall the quark flavours d , s , and b had primes. These indicate that they are weak eigenstates and are combinations of the flavour or mass eigenstates

$$d' = \alpha d + \beta s + \gamma b, \quad (1.12)$$

where

$$\alpha^2 + \beta^2 + \gamma^2 = 1. \quad (1.13)$$

The W^\pm couples to the weak isospin doublets of the weak quark eigenstates, for instance,

$$\begin{pmatrix} u \\ d' \end{pmatrix}$$

and

$$\begin{pmatrix} c \\ s' \end{pmatrix}.$$

If an s quark is produced it will be a mixture of $s = \tilde{\alpha}d' + \tilde{\beta}s' + \tilde{\gamma}b'$. Thus the interaction

$$s \rightarrow u + e^- + \bar{\nu}_e. \quad (1.14)$$

is allowed because the s quark has a component of d' which can be changed to u through a W boson exchange.

1.2 Z^0 Physics at an e^+e^- Collider

The basic process at an e^+e^- collider is annihilation to either a photon or a Z^0 . The virtual photon decays electromagnetically producing any charged fermion antifermion pair, whereas the Z^0 interacts weakly making any fermion antifermion pair as illustrated in figure 1.6. The case $e^+e^- \rightarrow e^+e^-$ or Bhabha scattering is special because the initial and final states are identical. It is possible to reach this configuration by exchanging a γ or

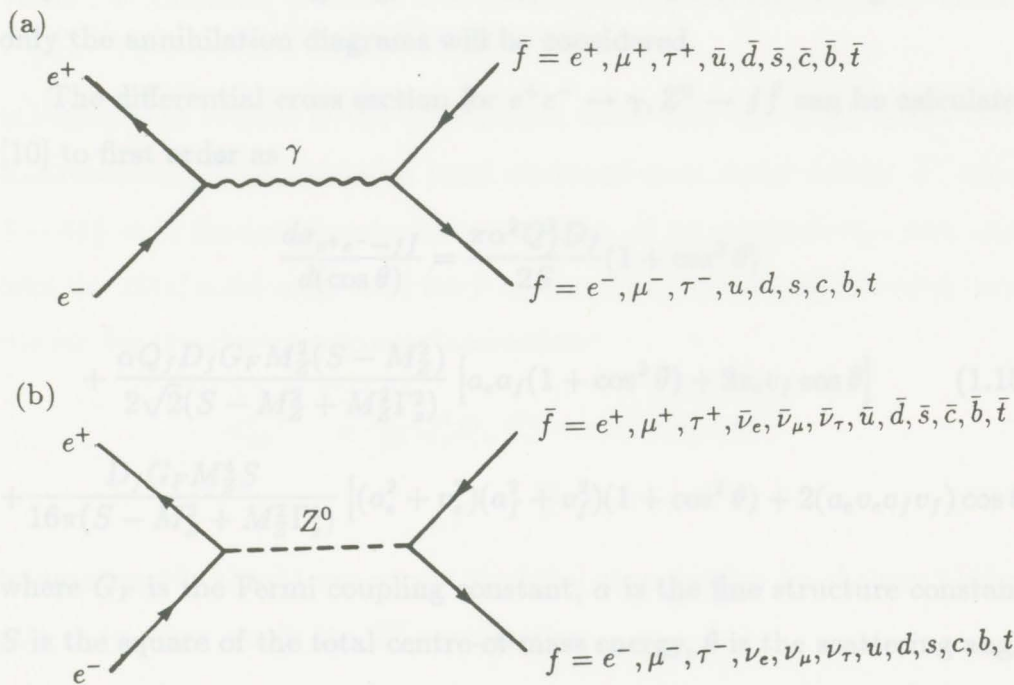


Figure 1.6: e^+e^- annihilation into (a) γ , (b) Z^0 .

Z^0 instead of annihilation as shown in figure 1.7. The effect of these extra diagrams is to enhance the scattering cross section at small angles. It has

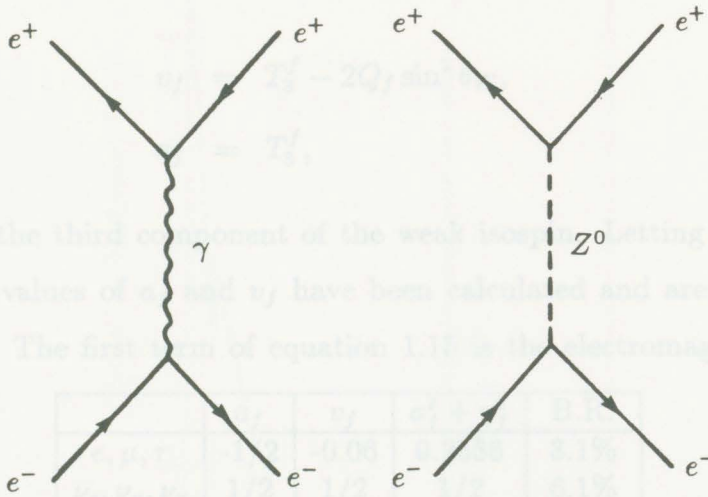


Figure 1.7: Bhabha scattering also requires t-channel contributions.

very little effect at angles greater than 10° . For the remaining discussion only the annihilation diagrams will be considered.

The differential cross section for $e^+e^- \rightarrow \gamma, Z^0 \rightarrow f\bar{f}$ can be calculated [10] to first order as

$$\begin{aligned} \frac{d\sigma_{e^+e^- \rightarrow f\bar{f}}}{d(\cos\theta)} &= \frac{\pi\alpha^2 Q_f^2 D_f}{2S} (1 + \cos^2\theta) \\ &+ \frac{\alpha Q_f D_f G_F M_Z^2 (S - M_Z^2)}{2\sqrt{2}(S - M_Z^2 + M_Z^2 \Gamma_Z^2)} [a_e a_f (1 + \cos^2\theta) + 2v_e v_f \cos\theta] \\ &+ \frac{D_f G_F M_Z^4 S}{16\pi(S - M_Z^2 + M_Z^2 \Gamma_Z^2)} [(a_e^2 + v_e^2)(a_f^2 + v_f^2)(1 + \cos^2\theta) + 2(a_e v_e a_f v_f) \cos\theta] \end{aligned} \quad (1.15)$$

where G_F is the Fermi coupling constant, α is the fine structure constant, S is the square of the total centre-of-mass energy, θ is the scattering angle relative to the incident positron direction, M_Z is the mass of the Z^0 , $D_f = 3$ if f is a quark or $D_f = 1$ if f is a lepton, Q_f is the charge of the fermion, Γ_Z is the Z^0 width

$$\Gamma_Z = \frac{G_F M_Z^3}{6\sqrt{2}\pi} \sum_f (a_f^2 + v_f^2) D_f, \quad (1.16)$$

and

$$\begin{aligned} v_f &= T_3^f - 2Q_f \sin^2 \theta_W, \\ a_f &= T_3^f, \end{aligned}$$

where T_3^f is the third component of the weak isospin. Letting $\sin^2 \theta_W = 0.22$ [7], the values of a_f and v_f have been calculated and are tabulated in table 1.3. The first term of equation 1.15 is the electromagnetic con-

	a_f	v_f	$a_f^2 + v_f^2$	B.R.
e, μ, τ	-1/2	-0.06	0.2536	3.1%
ν_e, ν_μ, ν_τ	1/2	1/2	1/2	6.1%
d, s, b	-1/2	-0.35	0.375	10.6%
u, c, t	1/2	0.21	0.29	13.6%

Table 1.3: Coupling constant and branching ratio for the Z^0 decay modes, where the value $\sin^2 \theta_W = 0.22$ is assumed.

tribution, the second is the interference term, and the third is the weak contribution. Note that at a total centre-of-mass equal to the Z^0 mass, $S - M_Z^2 = 0$, the interference term vanishes. If we integrate the first term over the total solid angle and let f be the muon we obtain the total cross section for the electromagnetic interaction

$$\begin{aligned} \sigma_{\text{em}}^{\mu^+ \mu^-} &= \frac{\pi \alpha^2}{2S} Q_\mu^2 D_\mu \int (1 + \cos^2 \theta) d(\cos \theta) \\ &= \frac{87}{S} \text{ nb.} \end{aligned} \tag{1.17}$$

Integrating the third term we get the total cross section for the weak interaction, in other words the Z^0 contribution

$$\begin{aligned} \sigma_{\text{weak}}^{\mu^+ \mu^-} &= \frac{D_f G_F^2 M_Z^4}{6\pi \Gamma_Z^2} (v_e^2 + a_e^2)(v_\mu^2 + v_\mu^2) \\ &= \frac{13.81}{M_Z^2} \mu\text{b.} \end{aligned} \tag{1.18}$$

We can see that at the total centre-of-mass equal to the mass of the Z^0 the weak contribution is 159 times larger than the electromagnetic. The ratio is

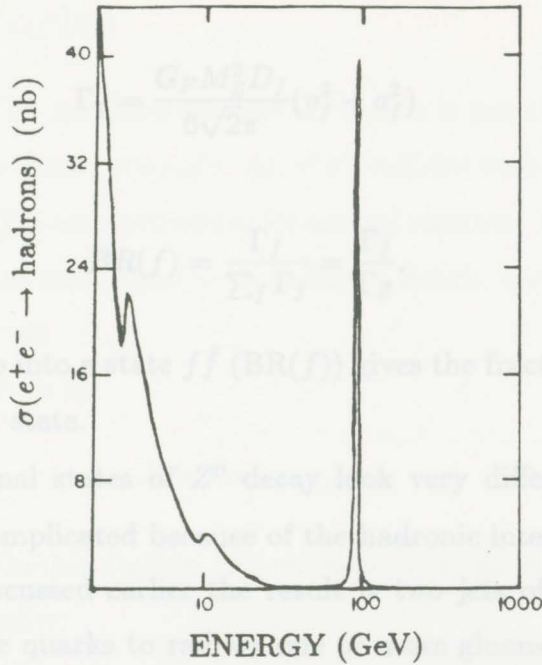


Figure 1.8: Cross section for the reaction $e^+e^- \rightarrow q\bar{q}$ as a function of the total centre-of-mass energy.

even larger for the production of quarks and neutrinos (see figure 1.8). The third term of equation 1.15, annihilation into a Z^0 , therefore dominates at the energies we will be discussing in this thesis. The angular distribution contains a term in $(1 + \cos^2 \theta)$ and $\cos \theta$. The former dominates by at least a factor of 8 for all of the standard model final states and we will use it as the angular distribution

$$\frac{d\sigma^{f\bar{f}}}{d\Omega} = 1 + \cos^2 \theta. \quad (1.19)$$

The $\cos \theta$ term leads to small scattering asymmetries that will not be the subject of this thesis.

The total width of the Z^0 , equation 1.16, is related to its mean lifetime by $\tau = h/\Gamma_Z$. The width can be seen from 1.16 to be a sum of partial widths Γ_f or decay probabilities into the various possible final states. The fraction of the total width of a given final state is known as the “branching

ratio" $BR(f)$

$$\Gamma_f = \frac{G_F M_Z^3 D_f}{6\sqrt{2}\pi} (v_f^2 + a_f^2) \quad (1.20)$$

with

$$BR(f) = \frac{\Gamma_f}{\sum_f \Gamma_f} = \frac{\Gamma_f}{\Gamma_Z}. \quad (1.21)$$

The branching ratio into a state $f\bar{f}$ ($BR(f)$) gives the fraction of Z^0 's that will decay into that state.

The different final states of Z^0 decay look very different. The case $Z^0 \rightarrow q\bar{q}$ is more complicated because of the hadronic interaction between the quarks. As discussed earlier the result is two jets of hadrons. It is also possible for the quarks to radiate one or more gluons that will make additional jets.

Presently studying the Z^0 is difficult. The first evidence for the weak neutral current was from neutrino scattering experiments in 1973 at CERN [11]. Ten years later the first Z^0 and W^\pm were produced in the lab using the CERN proton-antiproton collider, and some of the decay modes were studied [12] and [13]. There are now approximately 100 recorded Z^0 's. So far everything is in agreement with the standard model.

The Z^0 is difficult to study at the hadron colliders because the production mechanism requires a quark from a proton to annihilate with an antiquark from an antiproton. The remaining quarks and antiquarks from the original proton and antiproton form jets that obscure the subsequent decay of the Z^0 . Also the strong interaction produces more jets than the weak interaction. The result is that one can only study the decay of the Z^0 into e^+e^- and $\mu^+\mu^-$. The need for a Z^0 factory that produces large numbers of Z^0 's with little or no background is essential if one wants to make precise measurements of the Z^0 properties.

1.3 Z^0 factories

The high rate of e^+e^- annihilation into Z^0 makes it possible to consider a machine to produce them copiously. An e^+e^- collider with opposing beams of energy $E = M_Z/2$ is very attractive for several reasons. The weak neutral bosons are created at rest, there is no hadronic debris, and the production rate can be made high.

The rate R is given by

$$R = \mathcal{L}\sigma_{e^+e^- \rightarrow Z^0}, \quad (1.22)$$

where $\sigma_{e^+e^- \rightarrow Z^0}$ is the production cross section, $\sigma = 40\text{nb}$ at the Z^0 peak, and \mathcal{L} is the luminosity,

$$\mathcal{L} = \frac{n_{e^-}n_{e^+}f}{\pi r_b^2} \text{ cm}^{-2}\text{s}^{-1}, \quad (1.23)$$

where n_{e^-} is the number of electrons in a beam bunch, n_{e^+} is the number of positrons in the colliding beam bunch, f is the rate at which bunches collide, and r_b is the radius of the beams at the interaction point. The Stanford Linear Collider or SLC is attempting to achieve

$$\begin{aligned} n_{e^-} &= n_{e^+} = 7 \times 10^{10}, \\ f &= 180 \text{ hz}, \\ r_b &= 2 \mu\text{m}, \end{aligned}$$

which corresponds to $\mathcal{L} = 7 \times 10^{30} \text{ cm}^{-2}\text{s}^{-1}$ or a rate at the Z^0 peak of 17 per minute.

The SLC [14] is based on the existing Stanford Linear Accelerator (LINAC). A true linear collider would use two LINAC's facing each other end to end. SLC is a prototype machine that accelerates the electrons and positrons sequentially in the same LINAC. After acceleration they are

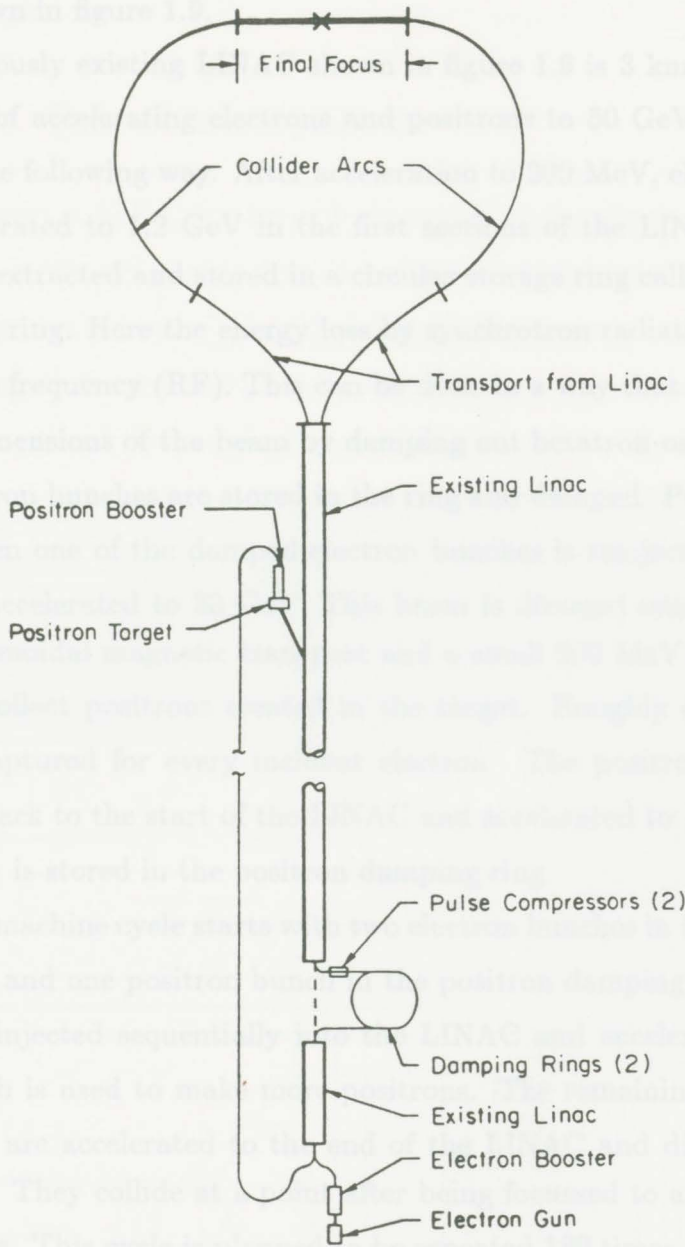


Figure 1.9: Diagram of SLAC Linear Collider

transported in magnetic channels through two opposing arcs into a collision point, as shown in figure 1.9.

The previously existing LINAC shown in figure 1.9 is 3 km long. It is now capable of accelerating electrons and positrons to 50 GeV. The SLC operates in the following way. After acceleration to 200 MeV, electrons are further accelerated to 1.2 GeV in the first sections of the LINAC. These electrons are extracted and stored in a circular storage ring called the electron damping ring. Here the energy loss by synchrotron radiation is made up with radio frequency (RF). This can be done in a way that shrinks the transverse dimensions of the beam by damping out betatron oscillations.

Two electron bunches are stored in the ring and damped. Positrons are produced when one of the damped electron bunches is reinjected into the LINAC and accelerated to 33 GeV. This beam is directed onto a tungsten target. A solenoidal magnetic transport and a small 200 MeV accelerator are used to collect positrons created in the target. Roughly one useable positron is captured for every incident electron. The positron bunch is transported back to the start of the LINAC and accelerated to 1.2 GeV, at which point it is stored in the positron damping ring.

A normal machine cycle starts with two electron bunches in the electron damping ring and one positron bunch in the positron damping ring. Next all three are injected sequentially into the LINAC and accelerated. One electron bunch is used to make more positrons. The remaining positrons and electrons are accelerated to the end of the LINAC and directed into opposite arcs. They collide at a point after being focussed to a beam spot $2 \mu\text{m}$ in radius. This cycle is planned to be repeated 180 times per second.

The SLC has two unique features. The first is the possibility of a polarized electron beam. This enhances the asymmetry of the angular distribution and makes possible very sensitive tests of the standard model. The other important feature is the very small beam radius. This allows a detector to be situated very near the interaction point and thereby signifi-

cantly improves one's ability to discriminate secondary vertices of particles decaying in flight.

1.4 The detection system

A detector known as SLD [15] is being built to exploit the physics of the SLC colliding beams. We will give an overview of the whole detector emphasizing the liquid argon "calorimeter" (LAC) which will be the main interest of this thesis. Starting at the interaction point the detector is built in a series of concentric cylindrical layers (see figure 1.10) centred on the e^+e^- beam

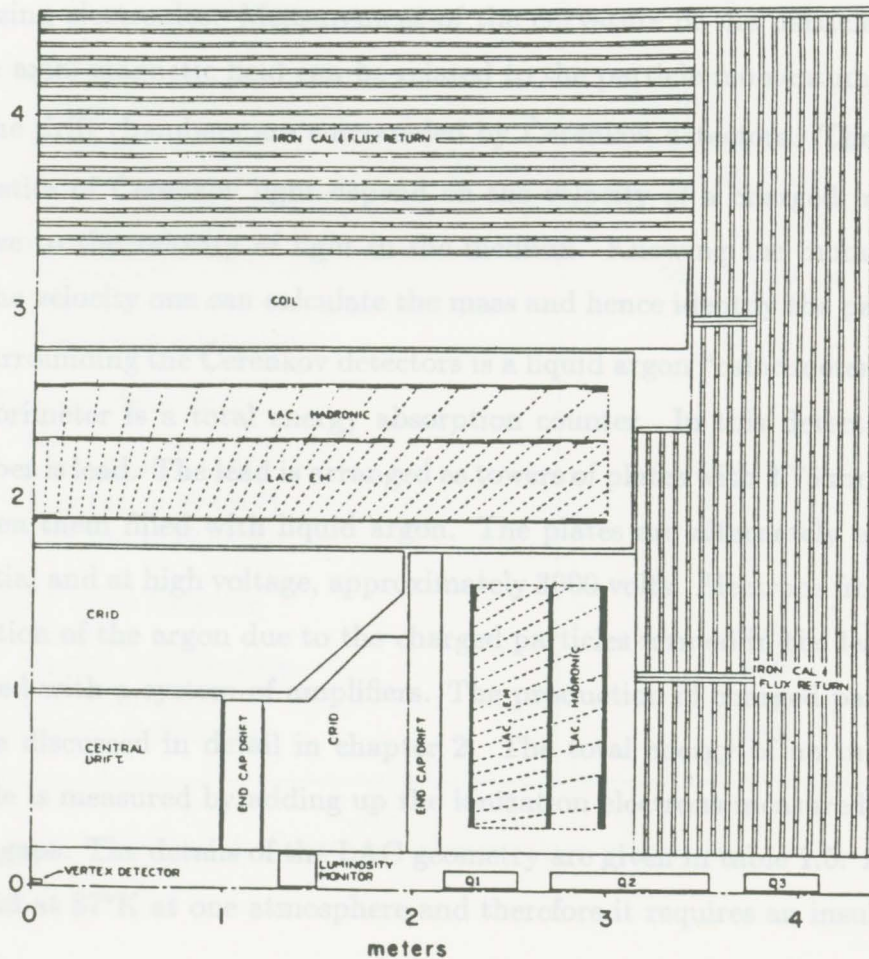


Figure 1.10: Side view of one quadrant of SLD in the plane including the beams.

axis. Table 1.4 contains a summary of the detector subsystem properties. An axial magnetic field of 0.6 T is maintained over the volume inside a diameter of 5.8 m.

The first section is two cylindrical layers of charged coupled devices (CCD's) known as a "vertex detector". Each charged particle will give two space points known with precision of better than $5 \mu\text{m}$. Following the CCD's is a large drift chamber. This is a volume of gas (mixture of argon, CO_2 , and Isobutane) instrumented with wires that provide a uniform electric field gradient. Electrons ionized by charged particles drift to the anode wires where their position and drift time can be recorded by transient analyzing electronics. Measurement of the curvature of the particle track in the axial magnetic field can be related to the particle momentum.

The drift chambers are surrounded by Čerenkov detectors. The characteristics of Čerenkov light depend on the velocity of a charged particle relative to the velocity of light in the medium. Knowing the momentum and the velocity one can calculate the mass and hence identify the particle.

Surrounding the Čerenkov detectors is a liquid argon "calorimeter" [16]. A calorimeter is a total energy absorption counter. In this detector the absorber is lead. The lead is arranged as towers of plates with 2.75 mm gaps between them filled with liquid argon. The plates are alternately at zero potential and at high voltage, approximately 3000 volts. Electrons from the ionization of the argon due to the charged particles formed in the lead are detected with a system of amplifiers. The production of charged particles will be discussed in detail in chapter 2. The total energy of an incident particle is measured by adding up the ionization electrons measured in all of the gaps. The details of the LAC geometry are given in table 1.5. Argon is liquid at 87°K at one atmosphere and therefore it requires an insulating dewar.

The LAC is inside a solenoidal coil that provides an axial field of 0.6 T.

Drift Chamber System	
Spatial Resolution (σ)	$\leq 100 \mu\text{m}$
Magnetic Field	0.6 Tesla
Momentum Resolution	
$\sigma(1/p)$ measurement limit	$1.3 \times 10^{-3} (\text{GeV}/c)^{-1}$
$\sigma(p)/p$ Coulomb scattering limit	$(1-2) \times 10^{-2}$
Two-Track Separation	1 mm
Calorimetry	
Electromagnetic	
Energy Resolution σ_E/E	$8\% / \sqrt{E (\text{GeV})}$
Segmentation	$\sim 33 \text{ mrad} \times 36 \text{ mrad}$
Angular Resolution	$\sim 5 \text{ mrad}$
Hadronic	
Energy Resolution σ_E/E	$\leq 55\% / \sqrt{E (\text{GeV})}$
Segmentation	$\sim 66 \text{ mrad} \times 72 \text{ mrad}$
Angular Resolution	$\sim 10 \text{ mrad}$
Vertex Detector	
Segmentation	$22 \mu\text{m} \times 22 \mu\text{m}$
Precision Transverse to Line of Flight	$4 - 20 \mu\text{m}$
Two-Track separation	$40 \mu\text{m}$
Particle Identification	
e/π	1×10^{-3}
μ/π (above 1 GeV)	2×10^{-3}
K/π (up to 30 GeV)	1×10^{-3}
K/p (up to 50 GeV)	1×10^{-3}
Solid Angle Coverage	
Tracking	97%
Particle Identification	97%
EM Calorimeter	$\geq 99\%$
Hadron Calorimeter	97%

Table 1.4: Summary of subsystem properties

	LAC			
	EM		HAD	
	EM1	EM2	HAD1	HAD2
Unit cell	2.0 mm lead 2.75 mm argon 2.0 mm lead 2.75 mm argon		6.0 mm lead 2.75 mm argon 6.0 mm argon 2.75 mm argon	
number of cell	8	20	13	13
thickness (cm)	7.6	19.0	22.75	22.75
X_0	6.03	15.1	-	-
λ	0.84		1.0	1.0
angle of tower	33 × 36 mrad		66 × 72 mrad	
number of aximuthal segmentations	192		96	
number of polar segmentations	100		50	
π/e	0.85			
	Barrel		End Cap	
R_{\min} (cm)	177		20	
R_{\max} (cm)	292		171	
Z_{\min} (cm)	-		217	
Z_{\max} (cm)	347		361	
number of channels	34400		9600	

Table 1.5: LAC geometry parameters. The dimensions of the barrel and the endcap include the cryostat and the vacuum vessel.

The coil is enclosed in a laminated iron box that acts as a flux return and helps to keep the field lines on axis near the end of the coil. Between the iron laminations argon gas detectors are stacked. These are operated in the limited streamer mode, which means that they act like a Geiger counter with a fast reset time. These tubes can be used to track very penetrating particles such as muons and the energy deposited can be added to the LAC, providing more depth to the calorimeter.

Overall the detector (figure 1.11) is roughly 10 m long and 9.5 m in

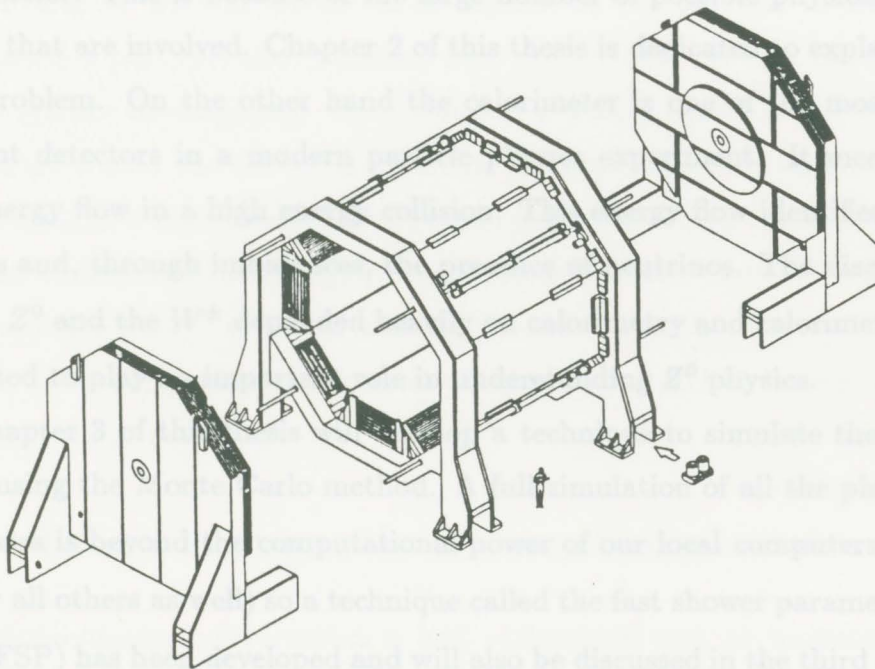


Figure 1.11: SLD WIC

diameter. It weighs in excess of 2000 metric tonnes. It is presently under construction and should be completed near the beginning of 1990.

1.5 Simulation of Z^0 Physics using the SLD Detector

SLD is a large and complex detector. The design and construction of a project on this scale requires the careful study and optimization of many parameters that affect the engineering design and final response and resolution of the device for physical studies. It is not practical to build many full scale prototypes so we resort to computer simulations. The most difficult aspect of a high energy physics experiment to simulate is the response of a calorimeter. This is because of the large number of possible physical processes that are involved. Chapter 2 of this thesis is dedicated to explaining this problem. On the other hand the calorimeter is one of the most important detectors in a modern particle physics experiment. It measures the energy flow in a high energy collision. This energy flow identifies jets, muons and, through imbalances, the presence of neutrinos. The discovery of the Z^0 and the W^\pm depended heavily on calorimetry and calorimetry, is expected to play an important role in understanding Z^0 physics.

Chapter 3 of this thesis will develop a technique to simulate the SLD LAC using the Monte Carlo method. A full simulation of all the physical processes is beyond the computational power of our local computers (and nearly all others as well) so a technique called the fast shower parametrization (FSP) has been developed and will also be discussed in the third chapter.

The methods developed in Chapter 3 will be applied to the case of e^+e^- annihilations at the energy of the Z^0 mass. A number of important aspects of the LAC will be calculated and described in chapter 4. These results will be important when we are eventually trying to understand the analysis of data taken with the actual detector.

the Bethe-Bloch formula, of an incoming particle with speed $\beta = v/c$ and mass $M \gg m_e$ is [18]

$$\text{Chapter 2} \quad \left(\frac{dE}{dx}\right)_{\text{min}} \approx \left(\ln\left(\frac{2m_e c^2 \beta^2}{I(1-\beta^2)}\right) - \beta^2\right) \quad (2.1)$$

I is a constant that groups the electron properties given by

Showers and Calorimeters

In this chapter we will discuss some aspects of the physical interaction of subatomic particles and radiation with matter that play an important role in shower development. By looking at a simple model of the shower we will show that the shower is a natural consequence of the fundamental interactions of a high energy particle with matter and that the shower can be used to measure the energy of incoming particles. We will see that it is possible to parametrize the average behaviour of the shower. Finally we will discuss the general properties of calorimeters and their response to diverse types of particles.

2.1 Electromagnetic Interactions

The electromagnetic interaction is well understood and, as mentioned in the previous chapter, it is described by quantum electrodynamics (see for example B. Rossi [17]). We will not derive the detailed expressions but we will look at the general features so that we can understand how they affect the shower development and the characteristics of a calorimeter.

The important energy loss mechanism for heavy charged particles is by collision with the atoms of the medium. When a particle is moving through matter it interacts with the atomic electrons and ionizes the atoms along its trajectory. The expression for the energy loss per unit length $\frac{dE}{dx}$, called

the Bethe-Bloch formula, of an incoming particle with speed $\beta = v/c$ and mass $M \gg m_e$ is [18]

$$-\frac{dE}{dx} = D_e \left(\frac{Z_{in}}{\beta} \right)^2 n_e \left(\ln \left(\frac{2m_e c^2 \beta^2}{I(1-\beta^2)} \right) - \beta^2 \right). \quad (2.1)$$

D_e is a constant that groups the electron properties given by

$$\begin{aligned} D_e &= \frac{4\pi e^4}{m_e c^2} \\ &= 5.0989 \times 10^{-25} \text{ MeV} - \text{cm}^2, \end{aligned} \quad (2.2)$$

and Z_{in} is the charge of the incoming particle. The constant n_e contains all the information about the medium and is given by

$$n_e = Z_{med} \frac{N_a \rho_{med}}{A}, \quad (2.3)$$

where N_a is the Avogadro number, Z_{med} and A_{med} the atomic number and the atomic mass respectively, and ρ_{med} the density of the medium. The constant I , called the ionization potential, is the average amount of energy required to ionize an atom of the medium. It is given by

$$I \cong 16(Z_{med})^{0.9} \text{ eV}. \quad (2.4)$$

In the derivation of expression 2.1 it is assumed that the Born approximation is valid, that is to say that one can treat the wave function of the incoming particle as a plane wave. This approximation is good for low Z materials. One also has neglected the spin of the incident particle and target. Furthermore the equation is valid only for fast particles, $\beta \gg \frac{1}{137}$.

The curve at low energy, $\beta < 0.96$ or $E < 3Mc^2$, is proportional to $1/v^2$ and then reaches a minimum where the energy loss is about $2 \text{ MeV} \cdot \text{cm}^2/g$, as shown in figure 2.1. This region is called the minimum ionization region.

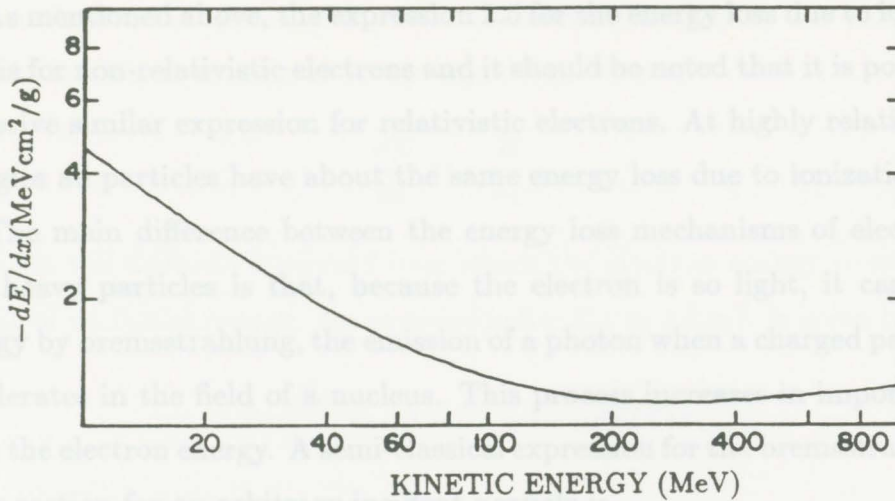


Figure 2.1: Curve of the energy loss by collision for pions in lead.

After the minimum there is a slow rise, called the relativistic rise, with a plateau at $\gamma = \sqrt{\frac{1}{1-\beta^2}} \sim 10^3$, where the energy loss is about 1.5 times the minimum. The plateau is related to a density effect that can be included in equation 2.1. For the purpose of this thesis we will consider the energy loss to be constant at the minimum value. Finally note that the energy loss by collision is proportional to Z_{med} and is not dependent on the mass of the incident particle.

The energy loss by collision for electrons has much the same behavior as for heavy particles. However, in the calculation, one needs to take into account the fact that the electron is much lighter and the particles colliding are identical. The non-relativistic expression for the energy loss due to ionization is [19]

$$-\frac{dE}{dx} = D_e \left(\frac{1}{\beta}\right)^2 n_e \left(\ln \frac{m_e c^2 \beta^2}{2I} - \frac{1}{2} \ln 2 + 0.5 \right), \quad (2.5)$$

so for the same nonrelativistic speed and stopping material an electron and a singly charged heavy particle will loss energy at approximately the same rate.

As mentioned above, the expression 2.5 for the energy loss due to ionization is for non-relativistic electrons and it should be noted that it is possible to derive similar expression for relativistic electrons. At highly relativistic energies all particles have about the same energy loss due to ionization.

The main difference between the energy loss mechanisms of electrons and heavy particles is that, because the electron is so light, it can lose energy by bremsstrahlung, the emission of a photon when a charged particle decelerates in the field of a nucleus. This process increases in importance with the electron energy. A semi-classical expression for the bremsstrahlung cross section for an arbitrary incident particle is

$$\frac{d\sigma}{dk} \simeq 5 \frac{e^2}{\hbar c} Z_{in}^4 Z_{med}^2 \left(\frac{mc}{Mv} \right)^2 \frac{r_e^2}{k} \ln \frac{Mv^2 \gamma^2}{k}, \quad (2.6)$$

where k is the photon energy, m the mass of the electron, and M and v are the mass and the velocity of the incident particle. The classical electron radius r_e is given by

$$r_e = \frac{e^2}{m_e c^2}. \quad (2.7)$$

By examining equation 2.6 one can see that the cross section is proportional to $1/M^2$, and hence important only for electrons. Note also that the cross section increases with Z_{med}^2 . The angle θ of photon emission in the bremsstrahlung process is peaked at

$$\theta \simeq \frac{m_e c^2}{E} \quad (2.8)$$

with E being the electron energy.

The energy at which energy loss by radiation equals that by ionization, and hence above which bremsstrahlung dominates, is known as the critical energy ϵ_0 . An approximate formula for the critical energy is given in section 2.2.1.

Another useful quantity that can be introduced here is the radiation length X_0 . It can be defined by the equation

$$\frac{dE}{dx} = -\frac{E}{X_0}, \quad (2.9)$$

i.e., it is the distance traversed over which the electron energy is reduced to $1/e$ of its initial energy. An expression for X_0 , in g/cm^2 , is given by [17]

$$\frac{1}{X_0} = 4\alpha \frac{N_a}{A_{med}} Z_{med}(Z_{med} + 1)r_e^2 \ln(183Z_{med}^{-\frac{1}{3}}). \quad (2.10)$$

The constant α is the fine structure constant

$$\alpha = \frac{e^2}{\hbar c} \simeq \frac{1}{137}. \quad (2.11)$$

Note that the energy loss by radiation is proportional to Z_{med}^2 .

Multiple scattering is an important effect for electrons. An incident electron with speed v and momentum p can either scatter from atomic electrons or from nuclei. Scattering from electrons, resulting in the loss of energy and small angular deviations, has been treated above. Scattering from a nucleus with charge Z_{med} is described by the Rutherford scattering formula

$$\frac{d\sigma}{d\Omega} = \frac{1}{4} \left(\frac{Z_{med}e^2}{pv} \right)^2 \frac{1}{\sin^4(\frac{\theta}{2})}. \quad (2.12)$$

Since the recoil energy is small, the energy loss by the incident particle is negligible. The angular distribution goes as $1/\sin^4(\frac{\theta}{2})$ and is strongly peaked in the forward direction; that is, most of the scattering is at small angles. Since each individual scattering centre is independent, it can be shown [17] that the end result of many small scatterings is to give a Gaussian distribution with an rms angle of deviation

$$\Phi_{rms} = \frac{E_s}{pv} \sqrt{\frac{t}{X_0}}, \quad (2.13)$$

where t is the thickness of the medium and $E_s \simeq 21$ MeV. Note that the deviation angle Φ_{rms} is proportional to Z_{med} (see equation 2.10). A good derivation of this equation can be found in reference [17]. It is useful to define the Molière Radius R_m as the radial distance to the direction of a particle, of initial energy ϵ_0 , after it has traversed one radiation length,

$$R_m = \frac{E_s}{\epsilon_0} X_0. \quad (2.14)$$

For the photon, one generally speaks of loss of intensity of a photon beam passing through matter, rather than a reduction of energy of the photons. This is because in most cases the photon loses its identity in the interaction. The rate of intensity loss is represented by the linear attenuation coefficient μ . A beam of N photons passing through a material of thickness dx will lose intensity at the rate

$$\frac{dN}{dx} = -\mu N, \quad (2.15)$$

so that the intensity of the beam can be seen to decrease exponentially with the thickness of the material traversed.

There are several different interactions that a photon can undergo. The cross sections for the most relevant of these interactions are illustrated in figure 2.2(b) for lead. At low energies, the photoelectric effect is dominant. This interaction is the absorption of the photon by an atomic electron, with the electron being ejected from the atom and the photon disappearing altogether. At energies comparable to the atomic K shell binding energies, there are sharp discontinuities in the photoelectric cross section. Above this energy range, the cross section becomes smoother and falls off roughly as Z_{med}^5/k .

Compton scattering, the scattering of a photon from an atomic electron, begins to gain importance at intermediate energies. At these energies, the electrons from which the photons are scattered can be considered to be

at rest. Since this is a scattering process, the photon is not destroyed, but rather suffers a loss of energy and so is effectively considered to be removed. The Compton cross section depends linearly on the number of electrons present, that is Z_{med} , and falls roughly as $1/k$.

At energies above $2mc^2$, pair production begins to play a role, and indeed dominates at energies above a few MeV. The pair production process, which is intimately related in QED to the radiation process, is the decay into an e^+e^- pair of a photon passing through the coulomb field of an atom. At photon energies $k \gg m_e c^2 / \alpha Z^{\frac{1}{3}}$, the pair production cross section asymptotically approaches the value of $7/9$ times the cross section for bremsstrahlung. Thus the pair production cross section, like that for bremsstrahlung, is proportional to Z_{med}^2 . The average angle of emission relative to the incident photon momentum for either the electron or the positron of energy E is

$$\theta \simeq \frac{m_e c^2}{E}. \quad (2.16)$$

Now that we have completed a survey of the relevant electromagnetic interactions, we may move on to the discussion of electromagnetic showers.

2.2 Electromagnetic showers

Quantum electrodynamics (QED) is a well understood theory that has been verified over many orders of magnitude. Thus the electromagnetic shower is well understood and can be accurately simulated. We will see later how such a simulation is done, but for the moment we will concentrate on the physics of electromagnetic showers. The important processes in the development of a shower occur at high energy. From figure 2.2(a) and (b) one can see that the important processes at high energy are bremsstrahlung for the electron, and positron and pair production for the photon. Those two processes really generate the shower, that is, the shower arises naturally by

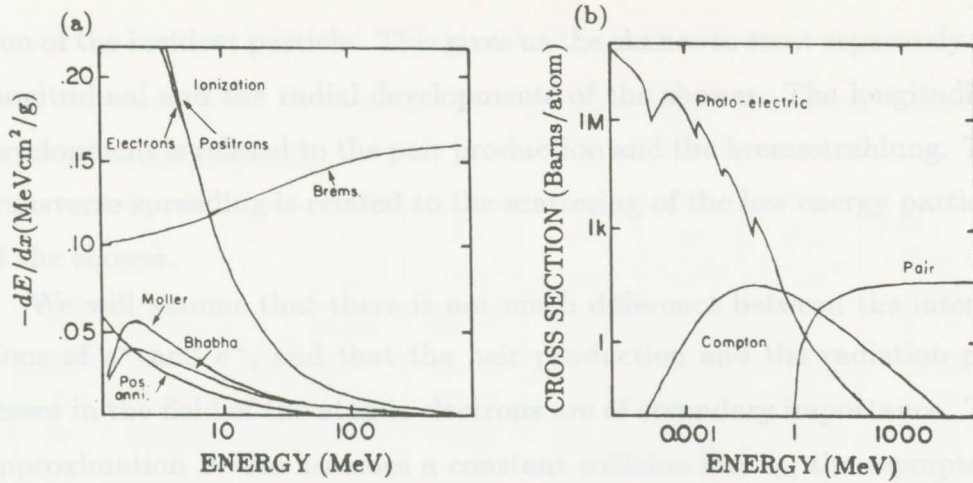


Figure 2.2: (a) Relative importance for diverse processes for the electron in lead. (b) Relative importance for diverse processes for the photon in lead.

the multiplication of the number of particles, each with decreasing energy. As we will see, the processes that are important at low energy, like the photoelectric effect and the energy loss by collision, play a crucial role in the measurement and response of the detector. Multiple scattering and Compton scattering have an influence on the transverse size of the shower and are also important when one wants to understand the detector response. As we will see, the electromagnetic shower is simple because the number of possible interactions is small and the number of particle types is also small. However even if we know all about the individual processes creating the shower, it is difficult to solve the problem exactly. Therefore one needs to simplify, which is the goal of the two next sections.

2.2.1 Approximations

In this section we will discuss what is often referred to as the approximation B, discussed in great detail in [17] along with some other general approximations.

The emission of radiation and the pair production at high energy are at small angles and therefore the shower develops essentially along the direc-

tion of the incident particle. This gives us the chance to treat separately the longitudinal and the radial developments of the shower. The longitudinal development is related to the pair production and the bremsstrahlung. The transverse spreading is related to the scattering of the low energy particles of the shower.

We will assume that there is not much difference between the interactions of e^+ and e^- , and that the pair production and the radiation processes in the field of the atomic electrons are of secondary importance. The approximation B also assumes a constant collision loss ϵ_0 , the asymptotic formulae for pair production and bremsstrahlung are assumed valid, and we neglect Compton scattering. Multiple scattering has also been neglected. The expressions obtained using this approximation are independent of the material, provided that energy is measured in terms of ϵ_0 and length in terms of X_0 . Since the condition $E \gg m_e c^2 / \alpha Z^{1/3}$ needs to be fulfilled in order to use the asymptotic formulae for pair production and bremsstrahlung, this approximation holds better for light material than heavy material.

At the same level of accuracy one can use approximate expressions for the radiation length X_0 , for the constant energy loss ϵ_0 , and the Moliere radius R_m . We have

$$X_0 \simeq 180 \frac{A}{Z^2} \frac{\text{g}}{\text{cm}^2}, \quad (2.17)$$

where the error is $\frac{\Delta X_0}{X_0} < \pm 20\%$ for $13 \leq Z \leq 92$, and

$$\epsilon_0 \simeq \frac{550}{Z} \text{ MeV}, \quad (2.18)$$

where the error is $\frac{\Delta \epsilon_0}{\epsilon_0} < \pm 10\%$ for $13 \leq Z \leq 92$. Recall that ϵ_0 is defined as the energy where the collision loss equals the radiation loss. Finally for the Moliere radius we have

$$R_m \simeq 7 \frac{A}{Z} \frac{\text{g}}{\text{cm}^2}, \quad (2.19)$$

where the error is $\frac{\Delta R_m}{R_m} < \pm 10\%$ for $13 \leq Z \leq 92$. These values are taken from reference [20]. In table 2.1 one can find some numerical values for these material properties.

	A	Z	ρ g/cm ³	X_0 g/cm ²	λ g/cm ²	ϵ_0 MeV	R_m g/cm ²	$\left(\frac{dE}{dx}\right)_{min}$ $\frac{\text{MeV}}{\text{g/cm}^2}$
C	12.01	6	2.265	42.70	86.3	91.67	14.01	1.78
Al	26.98	13	2.70	24.01	106.4	42.31	14.53	1.62
LAr	39.95	18	1.40	19.55	117.2	30.56	15.54	1.51
Fe	55.85	26	7.87	13.84	131.9	21.15	15.04	1.48
Cu	63.54	29	8.96	12.86	134.9	18.97	15.34	1.44
Pb	207.19	82	11.35	6.37	194	6.71	17.69	1.13
U	238.03	92	18.95	6.00	199	5.98	18.11	1.09

Table 2.1: Numerical value for material properties

2.2.2 Simple Model

Given the scaling variables of approximation B we can move on to examine some other properties of the shower. One can learn much from the following simple model [17] about the average behaviour of the shower. As mentioned above, if one expresses the energy in terms of the critical energy ϵ_0 , and the distance in radiation lengths X_0 , then the shower development can be described independently of the material through which it is traversing. In this model we assume that the e^\pm goes one radiation length and then emits a photon that has half the energy, and the photon goes one radiation length and then pair produces, dividing equally its energy between the e^+ and e^- . We will also consider that the energy loss by collision for $E > \epsilon_0$ is negligible and that for $E < \epsilon_0$ the energy loss by radiation is negligible, that is, the energy loss by collision is negligible until the particles are close to ϵ_0 , and then they stop radiating and have only collision losses. We will treat the longitudinal and radial development separately, paying more attention to the longitudinal development.

We will assume that the incident particle is an electron with energy E_0 ; however, the result does not depend on what particle initiates the shower. In the first radiation length X_0 , the electron loses half of its energy to a photon. The number of particles present in the shower is now two, and the average energy is $E_0/2$. Then, in the second X_0 , the photon will pair produce and the initial electron will again emit a photon, so now the number of particles is four and the average energy is $E_0/4$. The process continues similarly for proceeding radiation lengths. It is easy to see that the number of particles in the shower is given by

$$N(t) = 2^t = e^{t \ln 2}, \quad (2.20)$$

where t is the depth of the shower in radiation lengths. The energy of each particle is given by

$$E(t) = \frac{E_0}{2^t} = \frac{E_0}{e^{t \ln 2}}. \quad (2.21)$$

One should note that the number of particles of each type is equal; that is, the number of e^+ 's equals the number of e^- 's equals the number of γ 's. When the average energy of the particles in the shower is approximately ϵ_0 , then the number of particles in the shower reaches a maximum. After this maximum the charged particles lose their energy only by collision and therefore no more particles are generated. So the shower has a maximum at depth

$$t_{max} = \frac{\ln(E_0/\epsilon_0)}{\ln 2}, \quad (2.22)$$

and the number of particles at the maximum is given by

$$N_{max} = e^{t_{max} \ln 2} = \frac{E_0}{\epsilon_0}. \quad (2.23)$$

To get an idea of the energy spectrum one can calculate the number of

particles with an energy exceeding a given energy E , that is

$$\begin{aligned} N(> E) &= \int_0^{t(E)} N dt = \int_0^{t(E)} e^{t \ln 2} dt \\ &\simeq \frac{E_0/E}{\ln 2}. \end{aligned} \quad (2.24)$$

Therefore we have a spectrum

$$\frac{dN}{dE} \propto 1/E^2. \quad (2.25)$$

We know that the calorimeter measures the total track length of the charged particles, this being equivalent to measuring the energy when the energy loss per unit length is constant. We are therefore interested in calculating the total track length of all the charged particles in the shower. The total track length L is obtained by integrating the track length of each charged particle, giving

$$L = \frac{2}{3} \int_0^{t_{max}} N dt \simeq \frac{E_0}{\epsilon_0}, \quad (2.26)$$

where the $2/3$ factor comes from the fact that only $2/3$ of the total number of particles in the shower are charged.

The fundamental unit for the radial development of a shower is the Molière radius R_m . At the beginning of the high-energy shower all the processes have a small angle of emission so the lateral spread is not too important. After the maximum the multiple scattering of low-energy particles becomes more important and so the shower spreads considerably more. Before the maximum the radial dimension is about $1 X_0$ [18], while after the maximum the radius of 95% containment $R_{.95}$ is about $2 R_m$.

Because of the fact that the shower development involves statistical processes, the measurement of the total track length will have intrinsic fluctuations about an average. To estimate the magnitude of the fluctuations, note that the uncertainty in the number N of particles in the shower

is given by \sqrt{N} . By examination of equation 2.26 one can see that the total length of the shower will fluctuate according to

$$\Delta L \propto \sqrt{N} \propto \sqrt{E_0}.$$

So we can already see the average behaviour of the shower energy deposition. At the beginning the shower develops with an exponential rise and then falls down smoothly. Because the shower development involves random processes there will be fluctuations about the average shape of the shower. There are three types of fluctuations that we will consider. The origin of the shower, which we define as the vertex of the first interesting interaction (i.e. pair production or bremsstrahlung), fluctuates according to an exponential distribution. There are also fluctuations in the number of charged particles that are in the shower, hence affecting the apparent energy. The depth of the shower will also fluctuate. We can now draw some conclusion about the average behaviour of the shower:

- the depth of the shower increases logarithmically with the energy E_0 ,
- the total track length (area under dE/dx) is proportional to E_0 ,
- there are fluctuations in the total track length,
- there are fluctuations in the origin of the shower,
- there are fluctuations in the number of particles in the shower,
- there are fluctuations in total depth of the shower,
- resolution is proportional to $\frac{\Delta E}{E} \propto 1/\sqrt{E}$.

It is very important to notice that the total track length is proportional to the initial incident energy, so if one can measure the total track length, one has a signal proportional to the initial energy and the detector response is linear.

2.3 Hadronic interactions

The number and complexity of possible hadronic interactions is such that to discuss them in detail is beyond the scope of this thesis. However one can get a feeling for what is happening in general. The goal of this section will be to look at the features of possible interactions between hadrons and matter in order to understand showers, calorimeters and their limitations.

A simple kind of nuclear interaction is the elastic scattering of a hadron by a nucleus, where the incident hadron keeps its identity and the magnitude of its momentum is not affected in the centre-of-mass frame. Some energy goes into the recoil of the nucleus, the maximum fraction f of the energy transfer to the target being given by [21]

$$f = \frac{1}{A + 1}, \quad (2.27)$$

where A is the nuclear mass of the target. The recoil energy becomes important if the nucleus is light; for instance, if the collision involves a nucleon and a hydrogen nucleus then the incident nucleon will lose up to half of its energy. As we will see, this kind of interaction plays an important role in the calorimeter response to hadrons.

Inelastic collisions can be divided into three energy ranges. In inelastic collisions with a low energy transfer (that is, under the binding energy of a nucleon in the nucleus) the incident hadron leaves the nucleus in an excited state that will decay through the emission of a photon of a few MeV. Here the incoming hadron also keeps its identity. This type of inelastic collision plays a more important role in the detector response than in the shower development.

In the medium energy range, about 10^2 MeV, the inelastic interactions leave the nucleus in higher excited states that decay through the emission of slow nucleons until the excitation energy is less than the binding energy, and then it decays through emission of γ -rays. In these kinds of reactions the

nucleons emitted will be predominately neutrons because of the Coulomb barrier. These interactions are often noted in the literature as (h, xn) , (h, yp) , and $(h, xnyp)$, where x and y are the number of neutrons and protons emitted and h is the incident particle. Note that in this type of interaction, some of the energy used in boiling off nucleons is not detectable by a calorimeter. These so-called “binding energy losses” will be discussed further in section 2.4.1. These binding energy losses are correlated with the kinetic energy that goes into the neutrons.

At medium or high energy the inelastic collisions often cause spallation. Spallation at high energy, about 10^3 MeV and more, can be seen as a two-step process [21], the intranuclear cascade followed by evaporation. The high-energy hadron interacts with a nucleon inside the nucleus, giving the nucleon enough energy to travel inside the nucleus and hit other nucleons, thus generating an intranuclear cascade. If the energy transfer in a collision is large enough, the creation of pions or other hadrons may be possible. If the secondary particles have enough energy, they can escape the nucleus. The cascade is fast and liberates relatively high-energy nucleons, pions, and other hadrons. In this step it is possible that light nuclear fragments may also escape the nucleus; however, this can only happen for high-energy spallation reactions. The ratio of protons to neutrons liberated in this process is the same as the ratio of protons to neutrons in the nucleus.

In the next step after the cascade, the nucleus will generally be left in an excited state that will decay by emission of slow nucleons, mostly neutrons, until the energy of excitation is smaller than the binding energy of a nucleon. Then it will de-excite by the emission of γ -rays. The fission of the intermediate nucleus may also happen. This step is slower than the cascade step. Here again some energy is lost as binding energy.

Another type of relevant interaction is the fission of a nucleus. Fission is usually induced by a slow neutron incident on a heavy nucleus, for example

uranium. On average the fission of uranium liberates about 200 MeV, of which 90% goes into recoil of the nuclei. The remaining energy generates on average about 2.5 neutrons, each with about the same energy as the initial neutron (~ 10 MeV) and a γ -ray of about 7 MeV. The fission is followed by evaporation, as above, for the two final state nuclei.

The last important interaction that we will mention is the charge exchange. When a charged pion hadronically interacts with a nucleus, there is a finite chance that the pion will quasielastically scatter with the nucleus and exchange its charge, thus resulting in a neutral pion. The charge exchange probability is of the order of a few percent and is energy dependent.

2.4 Hadronic showers

In a hadronic shower the processes involved in the cascade development are more complex and numerous than in electromagnetic showers, so an analytic solution for hadronic showers is impossible. One can, however, use Monte Carlo calculations and measurements. Since the shower processes are mostly nuclear interactions of hadrons with nuclei in the medium, the showers scale with the interaction length λ . λ is the mean free path of a particle before undergoing an inelastic collision; for example it is about 17 cm in lead, see table 2.1. One can see an electromagnetic shower develop somewhat more continuously than a hadronic shower because X_0 is generally a lot shorter than λ , indeed the hadronic shower is more discrete.

Using our knowledge of the hadronic interactions we can try to build a simple picture of a hadronic shower. Typically at about one λ the incident hadron interacts in a high energy spallation reaction where it loses about half of its energy. The resulting intranuclear cascade produces neutral and charged pions, fast nucleons, and some light nuclei. The ratio of neutral pions to charged pions varies with the energy, and large fluctuations about the average ratio are found. The average transverse momentum of the sec-

ondary particles is about $350 \text{ MeV}/c$. This implies that for higher energy, the final spallation products will be in a cone that has a small opening angle. The fast pions and nucleons go forward for about another λ , losing energy by ionization, and then interact again through spallation or fission. In the evaporation step there is emission of slow nucleons, mostly neutrons, and some γ -rays. Note that the emission of light nuclei is important only for the first spallation reaction. The slow protons lose energy by ionization and the slow neutrons lose their energy by collision with nuclei until they are captured, usually far from the interaction point, or cause a fission of a nucleus. The slow protons and the light nuclei have a short range, and hence stop close to the interaction point. The neutral pions decay immediately into two photons that initiate electromagnetic showers. The hadronic shower thus has two components, one electromagnetic from neutral pions and one purely hadronic. Also one can see that the hadronic shower will be longer and more spread out than the electromagnetic shower.

An important feature of the hadronic shower is the time that it takes to develop. Some of the processes involved in the shower development are slow; therefore if one wants to measure the energy from all the processes, one has to wait a long time compared to the electromagnetic case. This feature is mainly due to the capture of slow neutrons far from the interaction points. That is, one has to wait about $1 \mu\text{s}$ so that all the slow neutrons are captured [21].

Another important feature of hadronic showers is the fact that a charged pion incident on the detector can sometimes be transformed into a neutral pion which will in turn decay into two photons. Those two photons will then initiate two electromagnetic showers, resulting in a pure electromagnetic signal and thus confusing the pion signal with an electron signal.

As we have seen, there are many more processes and many more possible particle types in a hadronic shower. Most of the information available on this type of shower comes either from direct measurement [22,23] or from

Monte Carlo calculations [24,25].

2.4.1 ‘Visible’ energy

Depending on where the energy goes, the amount of energy that can be detected varies. The ‘visible’ energy is the amount of energy that is detectable in a shower. For instance, on average, some fraction of the initial energy goes into μ 's and ν 's, γ 's from π^0 decay, recoil energy, binding energy that comes from the evaporation step, or de-excitation. The fluctuations among these processes are huge [21]. We will group all these fluctuations under the term hadronic fluctuations. Furthermore, the ionization from the slow nuclear fragments is usually dense and therefore saturates the active medium very easily, and thus does not contribute efficiently to the visible energy.

There is a correlation between the binding energy and the total kinetic energy of the emitted neutrons, so if one cannot efficiently detect the neutrons, the amount of energy that is not visible increases.

The detection of electromagnetic signals is much more efficient since almost all the particles (all the charged ones) contribute to the signal. As we have seen, there is an electromagnetic component from π^0 's in a hadronic shower, and the energy measured from a hadronic shower with a large π^0 component will have a larger response compared to a purely hadronic shower. So the fluctuation in the number of neutral pions in the spallation reactions and the average number of neutral pions are crucial in the determination of the amount of visible energy.

2.5 Calorimeters

Now that we have studied the average behaviour of the shower, we will focus our attention on the shower counter, or calorimeter. As mentioned above, the calorimeter is a block of matter large enough to totally absorb all the

energy of an incoming particle. It measures the energy by degrading the energy of the incident high-energy particle into a large number of particles of lower energy. However, the calorimeter is more than a simple block of matter: it is instrumented to get information on how much energy has been deposited and where the energy has been deposited. The signal is obtained by measuring the total track length, which is the sum of all the tracks of charged particles.

There are many types of calorimeters built of different materials and using different methods to measure the track length. A simple kind of calorimeter is a continuous block of sensitive matter, usually NaI scintillator or Pb-glass (it measures the Čerenkov light emitted by the charged particles of the shower). This kind of calorimeter is usually too expensive for large 4π detectors, but gives the most precise result because it minimizes dead regions and has no sampling fluctuations. The alternative is the sampling calorimeter, one in which the shower is sampled instead of continuously measured. It is made of layers of active material interleaved with passive layers, in terms of radiation lengths, most of the shower takes place in the passive medium and a fraction of the shower is measured in the active layers. On the average, shower fluctuations are higher for sampling devices, because the number of particles that cross a sampling region is smaller than the total number of particles in the shower. Sampling devices are most often used in large experiments since they are cheaper, but one loses on the energy resolution from the fluctuations introduced by the sampling and the dead regions.

The absorber (passive layers) material and the active material can be made of any of several elements. It also depends on physics requirements, physical dimensions, and cost. The materials used for the absorber are usually iron, aluminum, lead, copper, or uranium. For the active layer one can use wire chambers, scintillators, or ion chambers filled with liquid argon

or a warm organic liquid.

2.5.1 Detector response

In this section we will discuss the detector response for the SLD calorimeter, called LAC for Liquid Argon Calorimeter. The LAC uses lead for an absorber and liquid argon as the active layer being read out as an ionization chamber.

Before starting it is a good idea to recall the dependence on Z_{med} for the different interactions that play an important role in the shower development so that we can understand the response to different particle types. This is summarized in table 2.2.

Interaction	dependence
Collision	Z
Bremsstrahlung	Z^2
Multiple scatt.	Z
Pair production	Z^2
Photoelectric	Z^5
Compton	Z

Table 2.2: Table summarizing the dependence of the interaction on the nuclear charge of the medium.

The pattern of energy deposited in the calorimeters depends on the type of particle interacting in it. The energy deposition for the μ is by $\frac{dE}{dx}$ only. The electron will deposit almost all of its energy in the first $20 X_0$ of the calorimeter and the same is true for the photon. The neutrino will not interact at all in SLD for all practical purposes. The charged hadron will have on average a broader and deeper energy deposition ($\lambda/X_0 = 30.5$ for lead) and sometimes they will go through the calorimeter without interacting, i.e. as a minimum ionizing particle. Neutral hadrons are the same as charged except that there is no minimum ionizing track if it does not interact. The hadronic energy is generally deposited over more than 5λ . Often the calorimeter is segmented longitudinally so that one can use

this information to identify the particles that initiate the shower. If there is a charged particle detector in front of the calorimeter identification can be improved.

Furthermore, angular segmentation in the detector is useful for measuring the direction of the incoming particle and, if the segmentation is fine enough, it is possible to measure the energy of individual showers in a multi-track event.

In an ionization chamber the signal is obtained by integrating the collected charge on the plates of the chamber, and then amplifying the signal. The charges are collected by applying a high voltage on the plates. The time that it takes a shower to fully develop is very important; that is, if one chooses a short electronic integration time, the detector response to the hadrons will decrease because of slow processes involved in the shower response. A longer integration time may result in the problem of overlapping of events for high rate experiments. For SLD the rate is much less than the response time of the calorimeter.

The total signal from the readout layers is, as we mentioned above, linear with the energy of the incoming particle. However this signal needs to be calibrated. The signal from a minimum ionizing particle such as the muon can be used. We define the most probable measured pulse height, or response, of the muon spectrum as V_μ . We can also calculate the expected pulse height in the active layers by multiplying the number of active layers by $\frac{dE}{dx}_{min}$ which we will call E_{mip} for (minimum ionization particle). Setting $V_\mu = E_{mip}$ sets the energy scale of the calorimeter.

The observed pulse height of a shower V_{sh} can then be compared to V_μ . The ratio

$$n_{eq} = \frac{V_{sh}}{V_\mu} \quad (2.28)$$

is the number of equivalent minimum ionizing particles which is sometimes

called the number of mip's. The measured energy of the shower becomes

$$E_{sh} = n_{eq} E_{mip}.$$

If we consider the total kinetic energy of the incident particle that forms the shower, the potential number of mip's is

$$n_{eq}^{theory} = \frac{E_{kin}}{E_{mip}},$$

where E_{kin} is the kinetic energy.

One finds by experiment that on average $n_{eq} < n_{eq}^{theory}$ for an electromagnetic shower. We define

$$\frac{e}{\mu} = \frac{n_{eq}}{n_{eq}^{theory}}.$$

Therefore $\frac{e}{\mu}$ is less than one and the fraction of the energy deposited in the active layers for an electron is smaller than for a muon. This is due to the way the low energy photons lose energy. More than 60% [21] of the electromagnetic energy is deposited by particles with energy less than 4 MeV. At this energy the electrons stop in the lead because of their short range, so the energy is mostly deposited by low-energy photons. At low energy the photoelectric effect dominates and is strongly dependent on the atomic charge (see table 2.2) which is higher for lead than argon, so that the photons mostly interact in the absorber. Furthermore, the photoelectron is also at low energy and has a very short range; therefore it will also tend to stop in the absorber plate without contributing to the detectable signal. Thus it can be seen that it is crucial to understand low energy processes in order to understand the detector response.

We also define the ratio π/μ of the hadron shower response to the muon response. Combining e/μ and π/μ ratio we can get the π/e ratio, which is

more useful for analyzing the calorimeter response in experiments. Furthermore, we define $(\pi/e)^{int}$ as the ratio of a purely hadronic shower (without π^0 's) response to a purely electromagnetic shower response; we also find $(\pi/e)^{int} < 1$. The hadronic response is smaller because there is energy carried away by μ 's and ν 's, energy leaking out of the back of the detector, energy going into binding energy, and the ionization of slow charged particles easily saturates the active medium. We also note that $(\pi/e)^{int}$ and π/e are energy dependent. The fluctuation in π^0 multiplicity in a shower has an important effect on the energy resolution of a hadronic shower while the average π^0 multiplicity affects the π/e ratio.

In a hadronic shower the signal is mostly from ionization of the active medium by charged hadrons, e.g. protons and pions. It is possible to compensate the hadron response to make it the same for an electron of the same kinetic energy. To increase the response of a purely hadronic shower one can use the low energy photons produced in the de-excitation processes, the nuclear recoil energy, and the slow neutrons. Since low energy photons tend to interact more in the absorber than in the active layer, they are not very effective. The recoil energy is hard to detect because most of the time the recoil also stays in the absorber, and if it is in the active region it will saturate it. The slow neutrons seem to be the best way to enhance the hadronic signal. As noted before, the energy that goes into binding energy is correlated with the total kinetic energy of the neutrons. Liquid argon is not sensitive to low energy neutrons and so for SLD there is little compensation and π/e is not equal to one.

Because of the statistical nature of shower development the response of two identical particles with the same energy will not be the same. For electromagnetic showers the energy spectrum will be Gaussian [26] in most detectors. The resolution for an electromagnetic sampling calorimeter is dominated by the fluctuations in the sampling and not from shower fluctu-

ations. This is because the total number of particles in the shower is much larger than the average number $\langle N \rangle$ of particles crossing an active layer, so the energy resolution R is proportional to $1/\sqrt{\langle N \rangle}$. It can be shown that the resolution is given by [20]

$$R = \sigma/E = 3.2\% \sqrt{\epsilon_0 t_s / E}, \quad (2.29)$$

where t_s is the thickness of a sampling layer in radiation lengths. The incident energy E is expressed in GeV and ϵ_0 is expressed in MeV. For SLD we have $R \simeq 5\%/\sqrt{E}$.

This expression is the minimum limit that one can expect with a perfect sampling device. However with a practical device many effects arise that spoil the resolution. Landau fluctuations, which come from the fact that the distribution of the energy deposition for a minimum ionizing particle is asymmetric, are important for low density active layers. It will not have a large effect on the resolution of a liquid argon detector. The fluctuations in the path length have little effect on the resolution but do have an effect on the overall signal, that is the e/μ ratio. There are also many effects that are related to imperfections in the detector. The inefficiency of detecting low energy particles, important in Čerenkov calorimeters mostly, spoils the resolution. Saturation of the active medium is a problem for liquid argon and cannot be avoided. The dead regions in the detector created by the instrumentation and cryogenics equipment can only be minimized. The thickness of the calorimeter is also important; that is, if the calorimeter is not thick enough to fully contain the showers then there will be energy leaking out the back which will spoil the resolution. There are also fluctuations coming from the readout; for instance, with a liquid argon ion chamber there is electronic noise in the amplifiers. These kinds of problems will cause the resolution to not scale according to 2.29 and will add a constant term to the expression.

In general the resolution for the hadronic shower is worse than that of the electromagnetic shower. The hadronic resolution is limited by all the same factors as the electromagnetic resolution, but it is also limited by the hadronic fluctuations. Contrary to the electromagnetic shower where the sampling fluctuations dominate, the energy resolution for hadronic showers is dominated by the intrinsic shower fluctuations. It should be mentioned that the factors that spoil the resolution for both the electromagnetic and hadronic showers are worse in the case of hadronic showers.

We will close this section by pointing out that the shower depth fluctuations can also be represented by a Gaussian distribution [27].

2.5.2 Detector parameters

Having reviewed the properties of calorimeters and their limitations, we are left with summarizing the important parameters for these devices. This thesis will attempt to study the effects of some of the following parameters on the measurement of several physical quantities, for instance the axis of the events and the missing energy:

- energy resolution,
- e/π and $(e/\pi)^{int}$,
- sampling fraction,
- containment and dead regions,
- solid angle coverage,
- longitudinal and angular segmentation.

It should be noted that the $(e/\pi)^{int}$ ratio, the sampling fraction, saturation, containment, and dead regions all have an influence on the resolution

and e/π ratio. For instance, we have for the resolution

$$R = cE^{-1/2} + X \left((e/\pi)^{int} - 1 \right) + \alpha, \quad (2.30)$$

where c accounts for the sampling fluctuations and saturation, X accounts for the amount of hadronic fluctuations, and α accounts for containment and dead regions. Note that for electromagnetic showers $X = 0$. It is also possible to have a similar expression for π/e :

$$\pi/e = c_1(\pi/e)^{int} + c_2e\langle f_{\pi^0} \rangle(1 - (\pi/e)^{int}) + c_3, \quad (2.31)$$

In this chapter, we will discuss the computer simulation for the SLD experiment where c_1 , c_2 , and c_3 are parameters to be determined by experiment. Also $\langle f_{\pi^0} \rangle$ is the average fraction of production neutral pions to charged pions in a hadronic shower. The first term in the equation 2.31 accounts for the sampling, the second term for the average π^0 multiplicity or the average fraction of neutral pions to charged pions, and the third term for the dead regions and non-perfect containment.

The solid angle and the segmentation are more related with the detector efficiency and precision.

3.1 Monte Carlo Method

The Monte Carlo Method uses random sampling [28,29,30] to model statistical processes and to evaluate integrals. Consider the expectation value of a function $f(x)$ [28],

$$\langle f(x) \rangle = \int_a^b f(x) \rho(x) dx = \frac{1}{N} \sum_{i=1}^N f(x_i), \quad (3.1)$$

where $p(x)$ is a probability density over the interval (a, b) satisfying the following conditions:

$$p(x) \geq 0, \quad (3.2)$$

$$\int_a^b p(x) dx = 1. \quad (3.3)$$

Chapter 3

Simulation

In this chapter, we will discuss the computer simulation for the SLD experiment. In the first section we will discuss mathematical tools used for simulation of physical events. This will be followed by a brief section on the computer environment in which the work of this thesis has been done. The next section deals with simulation of high energy e^+e^- collisions and detector response to such events. This is followed by a section that discusses how realistic the simulation is, and what was included in the simulation. Finally, the last section describes in detail the method used to implement a fast simulation of a shower, the interaction of high energy radiation with matter. This code is the major contribution of this thesis and will be used to analyze the data taken by SLD.

3.1 Monte Carlo Method

The Monte Carlo Method uses random sampling [28,29,30] to model statistical processes and to evaluate integrals. Consider the expectation value of a function $f(x)$ [28],

$$\langle f(x) \rangle = \int_a^b f(x)p(x)dx \sim \frac{1}{N} \sum_{i=1}^N f(x_i), \quad (3.1)$$

where $p(x)$ is a probability density over the interval (a, b) satisfying the following conditions:

$$p(x) \geq 0, \quad (3.2)$$

$$\int_a^b p(x)dx = 1. \quad (3.3)$$

The expectation value $\langle f(x) \rangle$ is approximated by the arithmetic mean evaluated for a set of χ_i chosen with the distribution $p(x)$. The sum converges to the exact value of the integral as N approaches infinity.

Given the density $p(x)$ of a random variable χ , the probability that the random variable χ lies in the interval (a', b') is given by

$$P(a' < \chi < b') = \int_{a'}^{b'} p(x)dx. \quad (3.4)$$

An important case is the random variable Γ defined on the interval $(0, 1)$ and having a density $p_\Gamma(x) = 1$, i.e. a uniform distribution. In this case the probability that Γ lies in the interval (a', b') is given by

$$P(a' < \Gamma < b') = \int_{a'}^{b'} p_\Gamma(x)dx = b' - a'. \quad (3.5)$$

Using the uniform distribution we can construct other random variables H with a density $p_H(x)$ by solving

$$\int_a^H p_H(x)dx = \Gamma \quad (3.6)$$

for H [28]. As this requires being able to do the integral and invert the result it is not always possible to use equation 3.6. A general method, called Neyman's Method, that is well suited to the computer can be used for densities defined over a finite interval (a, b) that is bounded

$$\rho(x) \leq M, \quad (3.7)$$

where M is a finite constant. We can generate a random variable H with the density $p_H(x)$ by generating pairs of random numbers (x_i, y_i) using

$$x_i = (b - a)\Gamma + a, \quad (3.8)$$

$$y_i = M\Gamma. \quad (3.9)$$

If the point satisfies

$$y_i < p_H(x_i) \quad (3.10)$$

then

$$H = x_i \quad (3.11)$$

otherwise reject the pair and generate a new pair of random numbers.

Now to evaluate an integral

$$I = \int_a^b g(x)dx \quad (3.12)$$

by the Monte Carlo Method we have to convert equation 3.12 into the form 3.1. Consider an arbitrary density distribution $p_V(x)$, where the random variable V can be calculated from $p_V(x)$ using equation 3.6 or by Neyman's Method, and another new random variable H defined as

$$H = \frac{g(x)}{p_V(x)}, \quad (3.13)$$

then we have

$$\langle H \rangle = \int_a^b \left(\frac{g(x)}{p_V(x)} \right) p_V(x) dx, \quad (3.14)$$

and therefore

$$I = \langle H \rangle \sim \frac{1}{N} \sum_{i=1}^N \frac{g(V_i)}{p_V(V_i)}. \quad (3.15)$$

A more straightforward application of the Monte Carlo Method is for stochastic processes, where one knows a probability density for a given

process. Random variables can be generated that are distributed according to that density by the methods outlined above. As an example consider an e^+e^- collision producing $Z^0 \rightarrow \mu^+\mu^-$. As discussed in chapter 1 the angular distribution for this process is given by

$$\frac{d\sigma}{d\Omega} = \frac{d\sigma}{\sin\theta d\theta d\phi} \propto 1 + \cos^2\theta. \quad (3.16)$$

To generate random pairs of muons with the correct angular distribution one could apply equation 3.6 to get the variable Φ

$$\Phi = 2\pi\Gamma \quad 0 < \Phi < 2\pi \quad (3.17)$$

and Neyman's Method to get the random variable Θ , to the density

$$p_{\Theta}(\theta) = \frac{3}{8}(1 + \cos^2\theta)\sin\theta \quad 0 < \Theta < \pi \quad (3.18)$$

Therefore one muon would have the angles Θ and Φ and the other muon would have to be in the opposite direction by conservation of momentum $\Theta' = \Theta + \pi$ and $\Phi' = 2\pi - \Phi$.

We refer to each instance of 2 muons that we generated as an event. Of course there are usually many more internal degrees of freedom in a physically interesting problem.

The real advantage of the Monte Carlo Method is not apparent in the above examples because of their simplicity. This method can easily be extended to multiple integrals and stochastic processes with many random variables. Even more important, one does not require an analytic function. If necessary the density functions can be defined numerically. Therefore step functions, difficult cuts in three dimensions, and other non-analytic boundary conditions can be handled with no modification to the procedure.

In this analysis the Monte Carlo Method is used to generate the four vectors of the multiparticle final state of a Z^0 decay. It is also used to simulate the interaction of these particles with the detector.

3.2 Computer environment

The code discussed in this thesis was developed and tested on an IBM main frame 3083 BX at the University of Victoria. However, the actual running of the code was done at SLAC on a main frame 3081 K because the latter is faster and more available. The SLAC computing environment was duplicated here at the University of Victoria to allow the user to develop and run programs at UVic.

3.3 Simulation code

We want to simulate full Z^0 events through e^+e^- collisions, as created by SLC, and the response of SLD to understand what actual Z^0 decays will look like in the detector and to understand how well we can expect to measure the physics features of the Z^0 and its decays. This means that we have to be able to generate all possible decay modes. We also want to have events that can be used to test the simulation and the analysis code. The generator for the final states, called an event generator, was implemented in three ways described below. All of them are based on the Monte Carlo Method discussed above.

The simplest event generator is the single track generator. It generates a single particle with given initial conditions. The initial conditions are the origin, the direction, and the momentum of the particle. This generator is mostly used to test the simulation code or to answer specific questions about the performance of the detector (see chapter 4).

There is also a generator for leptonic decays of the weak neutral boson, it generates a lepton and its antiparticle in opposite directions. The input conditions are the direction of the particles, the energy of the system, and what particle is to be generated. Note that the origin of the event is assumed to be at the SLC interaction point. The leptonic decays are very simple

because of their multiplicity and therefore they can be used to test the analysis code for the experiment. This generator can also be used to do some simple physics (see chapter 4).

The simulation of hadronic decays, e^+e^- annihilation to hadrons in the final states, is done by JETSET [31], a program that is based on electroweak and QCD calculations. That is, JETSET can generate $q\bar{q}$ states in opposite directions in the centre-of-mass using the branching ratio given by the electroweak theory, and it calculates the fragmentation of quarks using the LUND string model [31] and calculates the probability of radiating a gluon according to second-order perturbative QCD. The fragmentation function used was the LUND symmetric fragmentation function [31]. JETSET comes with default parameters and options that can be modified by the user. The minimum input parameters are the centre-of-mass energy of the event, and the flavour generated. However, it is possible to specialize the run to study a specific problem. This is the most useful generator; it allows one to address important questions on the physics of the Z^0 (see chapter 4).

The definition of the detector geometry, the tracking of particles, and the detector response is taken care of by another package called GEANT [32]. This simulation code takes the input tracks given by a generator and propagates them through the geometry. After all the particles are tracked, the user generates the response of the detector to the event through the user written GEANT digitization section. The code presented in this thesis is part of the digitization section.

The propagation of particles is based on the Monte Carlo Method. As it tracks a particle, GEANT will randomly choose the next interaction from a set of probability distributions.

If we track all the particles and include all possible interactions, the shower is generated automatically. However, as will be discussed below,

the time required for the full simulation of a shower is very long. Therefore a simplification or approximation will have to be done, this is discussed in the rest of this chapter.

3.4 Simulation Level

In this section we will discuss the levels of simulation planned and coded. The simulation of the full shower with the full geometry will be good to address precise detector studies; however, it is very slow. Because we will be interested in speeding up the simulation we will have to make some assumptions, or approximations, so we can simplify the problem. Furthermore, to simplify the data generated by the program we will also simplify some physics issues. This section is designed to give a general picture of what exactly is taken into account in the simulation; that is, how realistic is the simulation.

For the purpose of the simulation the geometry of SLD has been considerably simplified: the only subsystems present are the LAC, the WIC, and the coil. All the other subsystems are absent and replaced with air. Note that the cryostat and the vacuum vessel for the LAC are implemented with aluminum concentric cylinders surrounding the LAC and centred on the interaction point. Furthermore, the LAC is implemented as four concentric cylinders filled with a homogeneous material; that is, the tiles and the argon gaps are all replaced by homogeneous material having the weighted average properties (A , Z , X_0 , and λ) of both materials. The effective radiation length of a layer is given by the ratio of the total radiation length (see table 1.5 and table 2.1) of the layer to the actual thickness (in cm) of the layer. The same is true for the absorption length λ . The same kind of simplification for the WIC is applied. That is, the WIC is also made up of a homogeneous material that has the correct weighted average properties of iron and gas (a mixture of 30% argon and 70% isobutane). This kind

of simplification reduces the number of boundaries between regions which speed up the code. We are allowed to do this simplification because, from the shower's point of view, the energy deposition scales with the radiation and absorption lengths. These assumptions will not greatly affect the results if one is not interested in knowing the sharing of the energy between the active and the passive media. The latter question can be addressed using the full simulation.

The towers are not directly implemented. At the tracking stage there are no towers, and the energy sharing between the individual towers is calculated at the digitization stage; that is, when the detector response to a given particle is generated.

Note that this simple geometry can be used by both the fast and full shower simulation, but that for the full shower it is possible to use a more complete and precise geometry. However this geometry was never used for the work presented in this thesis.

As with any other physical detector there is electronic noise in the energy measured in each tower, and sometimes a tower will record a hit even if no particle actually hit the tower. Furthermore, energy deposited in a tower may induce cross-talk, a signal on a neighbouring tower. Neither of these two features has been implemented in the simulation yet.

Through the parameters provided by LUND the user has great control on the type of events that are being generated. This is one advantage of a simulation code. In the analysis presented in chapter 4, only a subset of the possible decays of the weak neutral boson were used, that is, only the final states e^+e^- , $q\bar{q}$, and $q\bar{q} + q\bar{q}g + \dots$ were possible, and where q is either a u or a b quark. Note that when SLC will be running, all of these types of events will be mixed and other flavours will be created. However, distinguishing between two types of jets might be hard to do in the real experiment.

At the physics level there are more simplifications made, not only in order to reduce the execution time but also to simplify some of the analysis

so that the results obtained can be easily interpreted. The short lived ($\tau < 10^{-8}$ sec) particles are decayed by LUND and the vertex of the decay will be the same as the vertex of the e^+e^- collision. In other words, there are no secondary vertices. For the fragmentation of the quarks it is possible to use models other than the LUND string model [31]. In the simulation presented in the next chapter the initial state corrections were not taken into account; that is, the emission of a photon by the initial e^+e^- was not allowed. Finally, the angular distribution of the final states, as mentioned above, is randomly distributed according to the distribution 1.19. Note that the top quark was not included in the calculations. Only u and b quarks were used in the analysis because they are at each end of the quark mass spectrum.

3.5 Fast Shower Parametrization

In principle, the simulation of physical events is very straightforward, if one tracks every particle and includes all interactions the code will naturally simulate a shower. However, due to the large number of particles and interactions involved in a shower, this is not practical and therefore we need a faster method. In this section we will discuss the Fast Shower Parametrization (FSP) code. Along with the description of the FSP code, we will give the relevant default values for the various parameters of the code.

It is very time consuming to run GEANT with the full shower to simulate Z^0 events. Furthermore we are interested in having a number of Monte Carlo events of the same order as the number of Z^0 's produced in a year; that is, about 10^6 events. To give an idea of the numbers, it takes about 80 msec to track a particle up to the calorimeter, then about 40 msec to generate the shower for a 3 GeV pion, or about 1.6 seconds for a 3 GeV electron. Using the FSP code it takes about 16 msec for a 3 GeV pion,

and 23 msec for a 3 GeV electron. Note that the shower simulation times are strongly energy dependent. Assuming an average multiplicity of about 30 for a $u\bar{u}$ 2-jet event, each shower with an average energy of 3 GeV, it is reasonable to expect that it might take about 35 seconds of CPU time per event for a full shower; whereas, with the fast simulation it would take about 0.6 sec, for shower simulation only. Note also that this estimate assumes a simple geometrical description, with no tiles, plates, argon gaps, and no other subsystem as mentioned above. One should note that the time required to simulate a shower is shorter than the time required to track a particle up to the calorimeter. Furthermore the regions before the LAC are very simple and filled with air, therefore the tracking time will increase some more when all the subsystems are present. As well as unacceptably long CPU times, attempting to run complex events with full simulation also runs into limitations of available computer memory. It is these considerations that motivated the writing of the fast shower code. With the fast code it takes about 4.5 seconds to generate and analyze an event similar to the one discussed above.

As we will see, the method used is basically a numerical integration of the shower energy distributions, equations 3.19 and 3.24.

3.5.1 Electromagnetic parametrization

We know that a shower, when expressed in suitable units, is independent of the material properties so it is reasonable to expect that one can parametrize the average behaviour of an electromagnetic shower. The fluctuation about the average value can be reproduced by smearing the energy, the length of the shower, and the origin, and will be discussed in more detail in section 3.5.3.

$$\Lambda = (0.12 + 0.02s) R_{0.05} \quad (3.23)$$

Longitudinal

To find an analytic function representing the longitudinal energy distribution of a shower, we use the fact that the shower starts with a fast rise, reaches a maximum, and is followed by an exponential fall. The function used is [33]

$$dE = ks^{\alpha-1}e^{-\beta s} ds, \quad (3.19)$$

where s is the depth of the shower expressed in radiation lengths and k is a normalization constant given by

$$k = E_i\beta^\alpha/\Gamma(\alpha),$$

where E_i , the initial energy, is given in GeV. The parameters α and β are empirical and energy dependent and have been measured by the UA1 group [35] as:

$$\begin{aligned} \alpha &= 2.284 + 0.7136 \ln E_i, \\ \beta &= 0.5607 + 0.0093 \ln E_i. \end{aligned} \quad (3.20)$$

It is important to note that these parameters are given for the UA1 calorimeter, a device made of iron-lead and scintillator. Figure 3.1 shows the distribution of the energy as a function of depth.

Transverse

The transverse distribution is assumed to be exponential [27]. We have

$$dE = -\frac{E(s)}{\Lambda} e^{-r/\Lambda} dr, \quad (3.21)$$

where $E(s)$ is the energy as a function of the depth s of the shower, r is the radial distance, in cm, from the axis of the shower, and Λ a parameter characteristic of the distribution. The factor $E(s)/\Lambda$ is a normalization factor. The parameter Λ is given by

$$\Lambda = (0.12 + 0.02s) R_m, \quad (3.22)$$

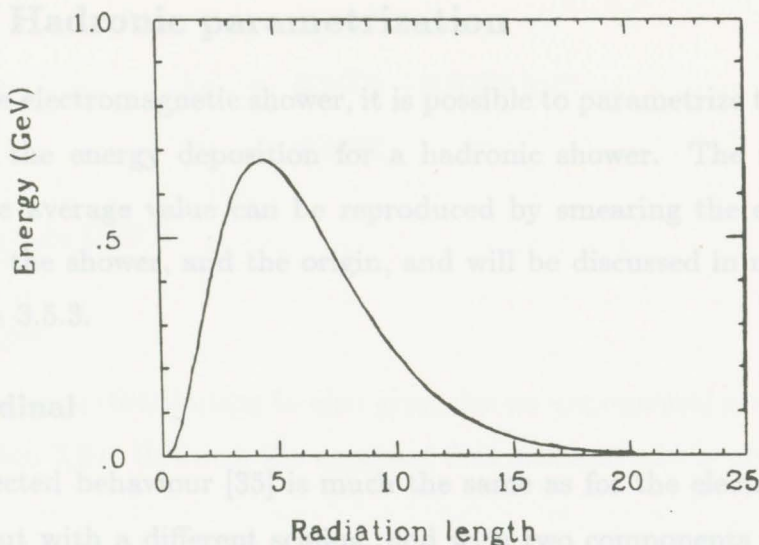


Figure 3.1: Longitudinal energy distribution of an electromagnetic shower using the function of equation 3.2.

where R_m is the Molière radius expressed in cm and s is in radiation lengths. We note that the distribution 3.21 does not depend on the initial energy of the shower; it only depends on Λ . Therefore the transverse dimension increases linearly with the depth. That is, the radius $R_{.95}$ of 95% containment, given by

$$R_{.95} = -\Lambda \ln 0.05, \tag{3.23}$$

is linear with the shower depth (see equation 3.22). Geometrically we have that the energy is deposited in a cone with an opening angle related to Λ and independent of the energy of the shower [34]. It is important to stress the characteristics of showers:

- the transverse distribution is normalized with the energy at a given depth,
- the energy is deposited in a cone,
- the opening angle of the cone is independent of the energy of the shower.

3.5.2 Hadronic parametrization

As for the electromagnetic shower, it is possible to parametrize the average shape of the energy deposition for a hadronic shower. The fluctuation about the average value can be reproduced by smearing the energy, the length of the shower, and the origin, and will be discussed in more detail in section 3.5.3.

Longitudinal

The expected behaviour [35] is much the same as for the electromagnetic shower but with a different scaling, and with two components to account for the fact that there is some fraction of the energy that goes into neutral pions, and thenceforth into an electromagnetic shower from the two-photon decay of the π^0 . Therefore we can use the same type of analytic function as for the EM shower, so we have

$$dE = k_{em} w s^{\alpha-1} e^{-\beta s} ds + k_{had} (1-w) t^{\mu-1} e^{-\nu t} dt, \quad (3.24)$$

where s and t are the depth of the shower in radiation lengths and in absorption lengths respectively, and w is the relative weight of the electromagnetic component. Note that each term has its own scaling. The electromagnetic and hadronic parts are normalized separately and therefore there are two normalization constants k_{em} and k_{had} given by

$$k_{em} = E_i \beta^\alpha / \Gamma(\alpha)$$

and

$$k_{had} = E_i \nu^\mu / \Gamma(\mu).$$

The measured parameters for the UA1 calorimeter are given by [35]

$$\alpha = 0.6165 + 0.3183 \ln E_i,$$

$$\beta = 0.2198,$$

$$\begin{aligned}
 \mu &= \alpha, \\
 \nu &= 0.9099 - 0.0237 \ln E_i, \\
 w &= 0.4634,
 \end{aligned}
 \tag{3.25}$$

where E_i is in GeV.

Transverse

The transverse distribution is also given by an exponential and therefore by equation 3.21. However the constant Λ is different and is given by

$$\Lambda = (39.4 + 0.25x\rho) \frac{1}{2.99\rho},
 \tag{3.26}$$

where ρ is the density, in g/cm^3 , of the medium in which the shower is developing, and x is the depth, in cm, of the shower.

The geometrical form of the parametrized hadronic shower is the same as for the electromagnetic shower. However, the transverse size of the hadronic shower is much greater than the electromagnetic one.

3.5.3 Fluctuations

The parametrizations just discussed for the electromagnetic and hadronic showers describe the average behaviour of those showers. If one was to investigate a number of real showers, one would of course find fluctuations around the average. There are three types of fluctuations that we will consider:

- the origin of the shower,
- the visible energy deposited,
- the length of the shower.

The first type of fluctuation, the fluctuation in shower origin, is naturally simulated by GEANT at the tracking stage. As discussed in section 3.3, GEANT steps each particle through the calorimeter, calculating the various probability distributions deciding which interaction the particle will undergo next. Thus, when the particle does begin to shower, it has already been subjected to the random fluctuations governing the point of the shower origin. With this in mind, it can be noted that the fluctuations in shower origin for the FSP will be identical to those of the full shower simulation.

The second type of fluctuation considered is the energy fluctuation, and it is handled by the FSP code. This fluctuation is handled by using the actual incident energy E_i in calculating the shower distribution, but then fluctuating by a factor f_E the energy deposited at the various points in the detector. These fluctuations are taken to be Gaussian, with standard deviations of $0.10\sqrt{E_i}$ for electromagnetic and $0.55\sqrt{E_i}$ for hadronic showers, where E_i is in GeV. Those values were chosen to reproduce the expected detector resolution for both sections (see table 1.4).

The third type of fluctuation considered is in the length of the shower. The length fluctuation factor f_l is also taken to be a truncated Gaussian about 1, with a standard deviation of 0.10 for electromagnetic showers and 0.50 for hadronic showers; those values were obtained from [36]. To keep the step size reasonable f_l is constrained to $0.25 < f_l < 2.00$. The way the FSP code handles the actual shower length is essentially either to increase or decrease the longitudinal density of energy deposited per computational step, thus resulting in a decreased or increased shower length, respectively. This will be discussed further in the next section.

It should be noted that both the length fluctuation f_l and the energy fluctuation factor f_E are determined only once per shower.

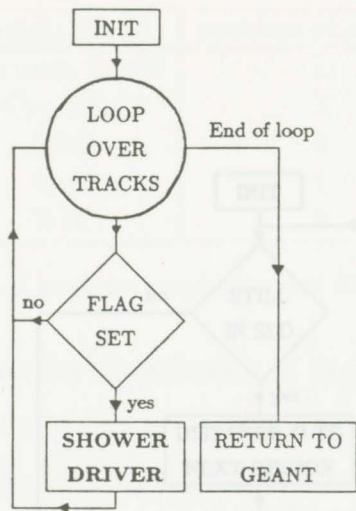


Figure 3.2: Flow chart of the FSP driver section of the FSP code.

3.5.4 Method

As mentioned above, the interface to the FSP code is in the “ digitization ” section of GEANT. To assist in the following discussion, a flow chart describing the logic flow of the FSP code is given in figures 3.2, 3.3, 3.6, 3.8 and 3.10. The boxes in these figures do not necessarily correspond to individual routines, but rather to important points in the logic of the code.

The strategy used to simulate a shower is to create a grid of points having the shape of a cone whose axis is along the direction \hat{n} of the particle when it begins to shower. Each grid point is given a fraction of the incoming particle energy determined by the integration of the appropriate distribution function, equations 3.19, 3.21 and 3.24.

Once all tracks have been calculated, GEANT will call the FSP driver. The FSP driver will loop over all the tracks calling the shower driver for those tracks that need to be showered (see figure 3.2).

The shower driver’s first task (see figure 3.3) is to initialize variables such as the starting point and direction of the current shower. It gets the energy fluctuation factor f_E , the length fluctuation factor f_l , and the value of the π/e ratio. If the particle is a charged pion, the code determines,

region name	number of regions
Vacuum vessel	1
Cryostat	1
LAC	4
Coil	1
WC	1

Table 3.1: List of regions used for the simulation.

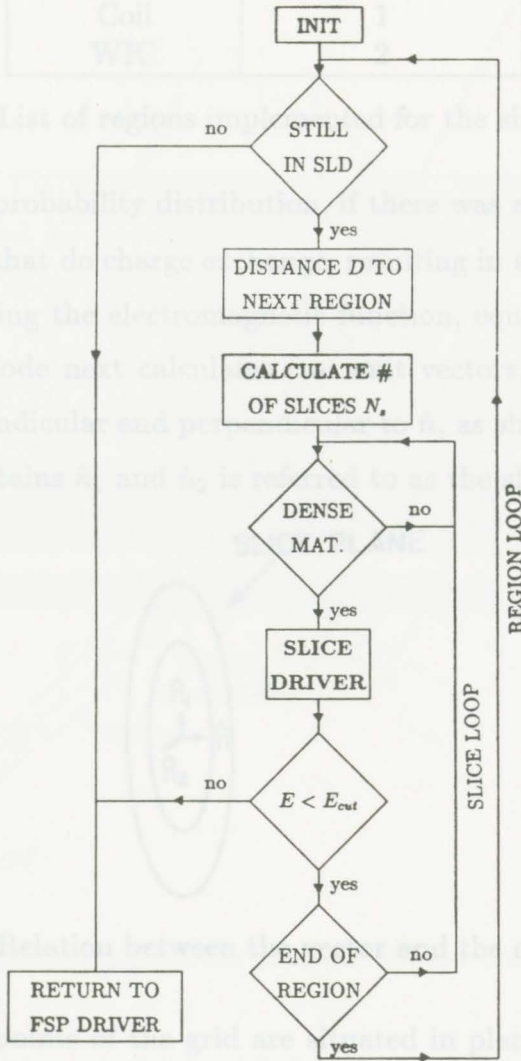


Figure 3.4: Relation between the region boundaries and the slice planes.

Figure 3.3: Flow chart of the shower driver section of the FSP code.

called regions; table 3.1 lists the regions that were implemented in the simulation. Once the detector region loop is entered, the code checks that the shower is within a subsystem of SLD. The code then calculates the distance D between two boundaries of the current region along the vector \hat{n}_i , as shown in figure 3.3. From the knowledge of the current material

region name	number of regions
Vacuum vessel	1
Cryostat	1
LAC	4
Coil	1
WIC	2

Table 3.1: List of regions implemented for the simulation.

by an appropriate probability distribution, if there was a charge exchange process. For pions that do charge exchange, resulting in a π^0 , the code will shower the pion using the electromagnetic function, equation 3.19. From the vector \hat{n} , the code next calculates two unit vectors, \hat{n}_1 and \hat{n}_2 , that are mutually perpendicular and perpendicular to \hat{n} , as shown in figure 3.4. The plane that contains \hat{n}_1 and \hat{n}_2 is referred to as the slice plane. As will

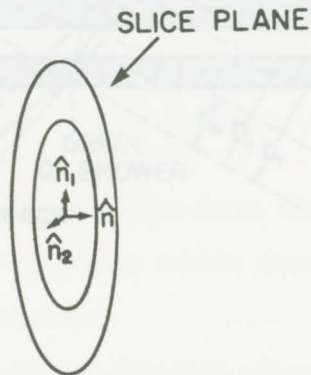


Figure 3.4: Relation between the vector and the slice plane.

be seen below, all points of the grid are situated in planes parallel to the slice plane. The code then enters the region loop.

In GEANT all the subsystems are represented by geometrical volumes, called regions; table 3.1 lists the regions that were implemented in the simulation. Once the detector region loop is entered, the code checks that the shower is within a subsystem of SLD. The code then calculates the distance D between two boundaries of the current region along the vector \hat{n} , as shown in figure 3.5. From the knowledge of the current material

properties the code then calculates N_s , the integer number of steps for the current region; i.e., in figure 3.5 the region LAC1 has $N_s = 3$. This is done

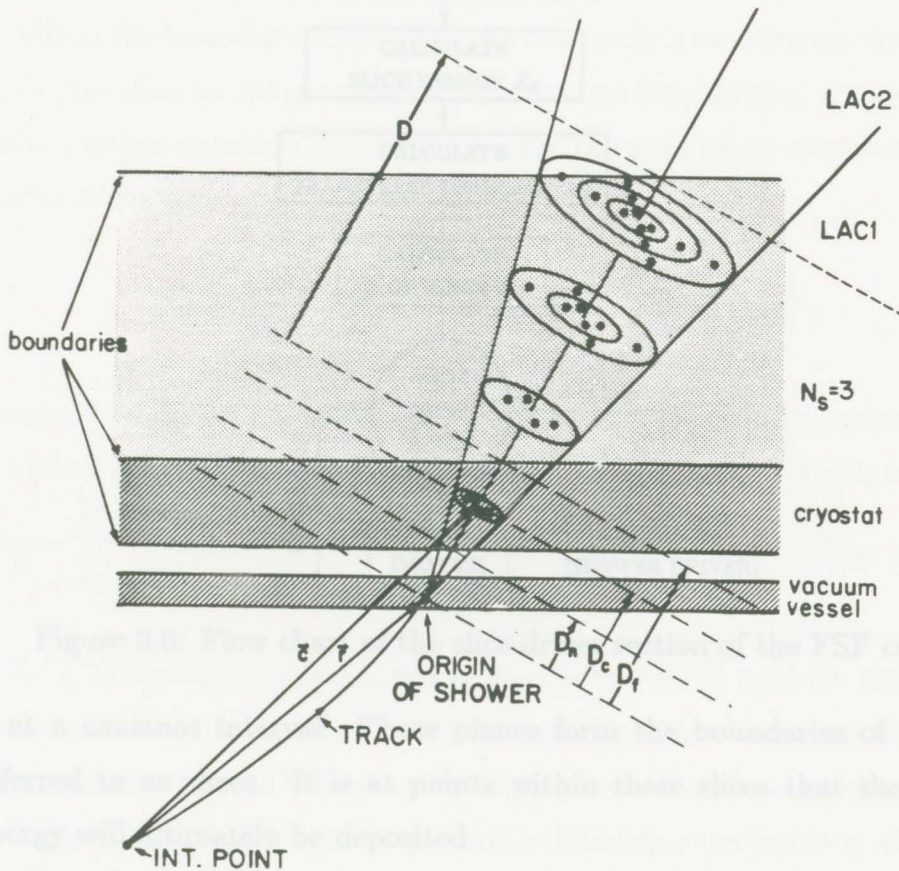


Figure 3.5: Diagram showing a track and the shower cone along with the appropriate vectors.

by performing an integer division of D by a default step size, $2.5 X_0$ for an electromagnetic shower or $15 X_0$ for a hadronic shower, then calculating the actual step size by dividing D by N_s .

The code then enters the slice loop where the first task is to test whether the current medium is air or a dense material. If it is air, the code simply exits the slice loop. If it is a dense material, the slice driver is entered.

There are $N_s + 1$ planes, the faces of N_s slices, each of which is parallel to the slice plane and therefore perpendicular to \hat{n} and each of which intersects

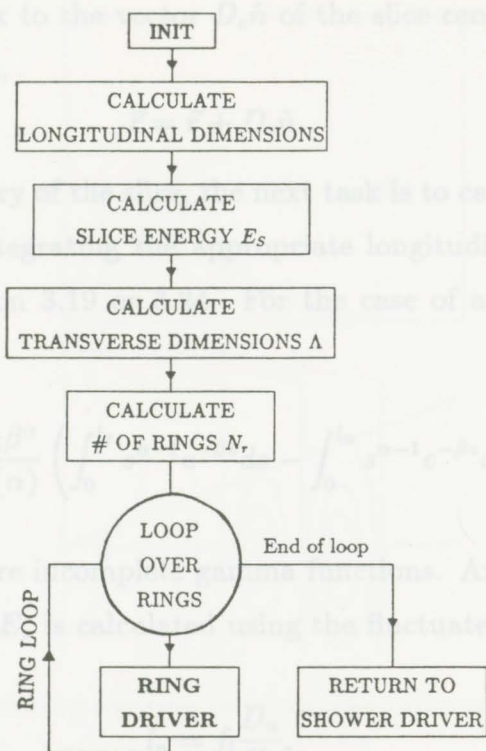


Figure 3.6: Flow chart of the slice driver section of the FSP code.

\hat{n} at a constant interval. These planes form the boundaries of volumes referred to as slices. It is at points within these slices that the shower energy will ultimately be deposited.

The slice driver (see figure 3.6) first initializes the various variables for the current slice. After initialization, the vector \vec{c} from the coordinate system origin (SLC interaction point) to the centre of the current slice is calculated. If we denote by D_n and D_f the respective distances, in cm, along \hat{n} from the shower origin to the nearest and farthest plane boundaries of the current slice, as shown in figure 3.5, then the distance D_c to the centre of the current slice is given by

$$D_c = \frac{D_f - D_n}{2} + D_n.$$

As shown in figure 3.5, \vec{c} is now found simply by adding the vector position

\vec{r} of the shower vertex to the vector $D_c \hat{n}$ of the slice centre relative to the shower vertex; that is,

$$\vec{c} = \vec{r} + D_c \hat{n}.$$

Given the boundary of the slice, the next task is to calculate the energy E_s in the slice by integrating the appropriate longitudinal energy distribution, either equation 3.19 or 3.24. For the case of an electromagnetic shower we have

$$E_s = \frac{E_i \beta^\alpha}{\Gamma(\alpha)} \left(\int_0^{l_f} s^{\alpha-1} e^{-\beta s} ds - \int_0^{l_n} s^{\alpha-1} e^{-\beta s} ds \right), \quad (3.27)$$

where the integrals are incomplete gamma functions. An important point to make here is that E_s is calculated using the fluctuated length l defined as

$$l_n = f_l \frac{D_n}{X_0},$$

where l_n is expressed in radiation lengths, while D_n is used for the energy deposition. The fluctuation factor, as mentioned above, has a truncated Gaussian distribution. The smeared length l is used in the calculation of E_s , while the unsmeared length D is used to determine the position of energy deposition in the detector. Thus a fluctuation factor less than 1 results in a longer shower (higher number of steps), and vice versa. Figure 3.7 shows the relation between the unsmeared length in the shower position and the smeared length in the shower energy distribution. Due to the finite step size we cannot calculate the integral of the longitudinal distribution exactly. For this reason, the shower is assumed to be terminated once 0.999 of its energy has been accounted for.

Once the energy in the slice is calculated, the transverse size of the slice is calculated using either equation 3.22 or 3.26. As in the case of the longitudinal distribution, the transverse distribution is divided into many regions, concentric volumes called rings. Because the transverse dimension

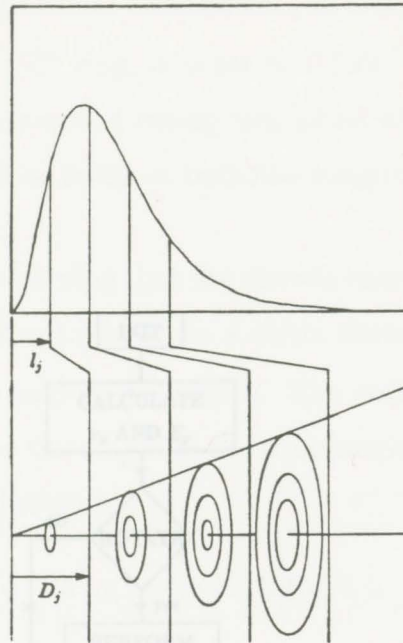


Figure 3.7: Figure showing relation between the unsmeared length D_j and the smeared length l_j .

of the shower depends on the depth in the shower of the slice, the number of rings is dependent on the slice depth. The number N_r of rings in the j^{th} slice is given by $N_r = 0.4j + 1$, with N_r constrained to be between the values 1 and 3. In figure 3.5 one can see the rings in a slice.

At this point the code loops over the N_r rings, calling the ring driver in each loop. In the ring driver (see figure 3.8), the code does some initialization for the current ring. The boundaries of a given ring can be calculated exactly since the transverse shower distribution has a simple analytic form, as seen in equation 3.21. The radii r are calculated such that the energy for the rings of a given slice are constant, that is $E_r = E_s/N_r$. The boundaries of the i^{th} ring are given by

$$r_{in} = -\Lambda \ln(1 - \alpha(i - 1)/N_r),$$

$$r_{out} = -\Lambda \ln(1 - \alpha i/N_r),$$

where α is the fraction of the transverse energy that is to be deposited.

As in the case of the longitudinal distribution, in order to avoid an infinite outer ring radius for the N^{th} ring, α is set to 0.999. It should be pointed out here that the total amount of energy deposited will typically be about 0.998 E_0 due to the cutoff of 0.999 in both the longitudinal and transverse distributions.

It is at points within each ring that the shower energy is to be deposited. Each point in a given ring is given by a circle centred on \hat{n} of radius r_p and equally spaced at an angle θ_p . The radius r_p is calculated in such a way that it divides the ring into two concentric sub-rings with each half of the ring energy; that is, $r_p = \sqrt{E_p/E_0}$ (where $E_p = 0.5/N_r$).

The point position \vec{r} is given by $\vec{r} = r_p(\cos\theta_p\hat{x} + \sin\theta_p\hat{y})$. The energy deposited at each point is E_p/N_p where N_p is the number of points in the ring.

By default, each ring contains N_p points with equal energy. It is at this stage of the code that a rotation vector \hat{r}_p is used, so the energy of each point is given by $E_p/N_p \cos^2(\theta_p)$.

The energy deposited at each point is $E_p/N_p \cos^2(\theta_p)$ where θ_p is the angle between the rotation vector and the point position vector. The energy deposited at each point is $E_p/N_p \cos^2(\theta_p)$.

for electromagnetic showers and $E_p/N_p \cos^2(\theta_p)$ for hadronic showers.

In order to avoid possible problems with the topology of energy deposition, each set of points in each ring can be randomly rotated, as shown in figure 3.9.

The code now enters the points loop over N_p points, where the first task is to calculate the absolute position vector in SLD of the current point

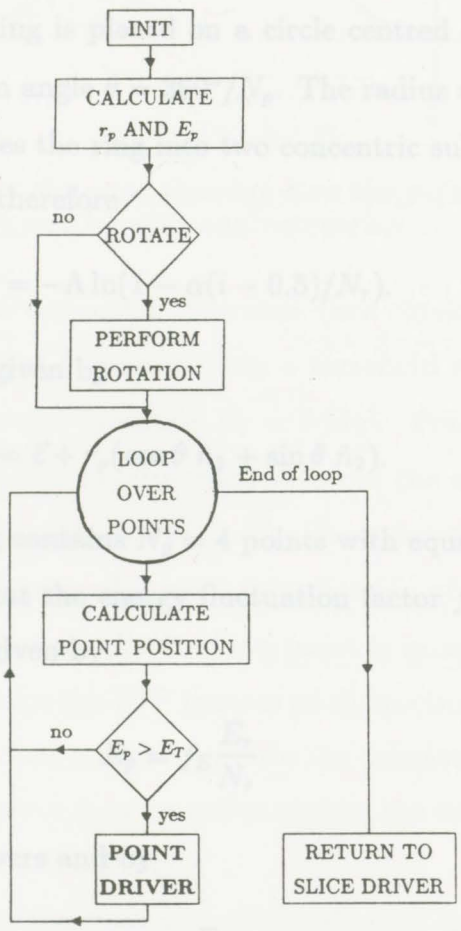


Figure 3.8: Flow chart of the ring driver section of the FSP code.

As in the case of the longitudinal distribution, in order to avoid an infinite outer ring radius for the N_r^{th} ring, α is set to 0.999. It should be pointed out here that the total amount of energy deposited will typically be about $0.998 E_i$ due to the cutoff of 0.999 in both the longitudinal and transverse distributions.

It is at points within each ring that the shower energy is to be deposited. Each point in a given ring is placed on a circle centred on \hat{n} of radius r_p and equally spaced at an angle $\theta = 360^\circ/N_p$. The radius r_p is calculated in such a way that it divides the ring into two concentric sub-rings with each half of the ring energy; therefore

$$r_p = -\Lambda \ln(1 - \alpha(i - 0.5)/N_r).$$

The point position \vec{p} is given by

$$\vec{p} = \vec{c} + r_p(\cos \theta \hat{n}_1 + \sin \theta \hat{n}_2).$$

By default, each ring contains $N_p = 4$ points with equal energy. It is at this stage of the code that the energy fluctuation factor f_E is used, so the energy of each point is given by

$$E_p = f_E \frac{E_r}{N_r} \quad (3.28)$$

for electromagnetic showers and by

$$E_p = f_E \frac{E_r}{N_r} \pi / e \quad (3.29)$$

for hadronic showers. In order to avoid possible problems with the topology of energy deposition, each set of points in each ring can be randomly rotated, as shown in figure 3.9.

The code now enters the points loop over N_p points, where the first task is to calculate the absolute position vector in SLD of the current point

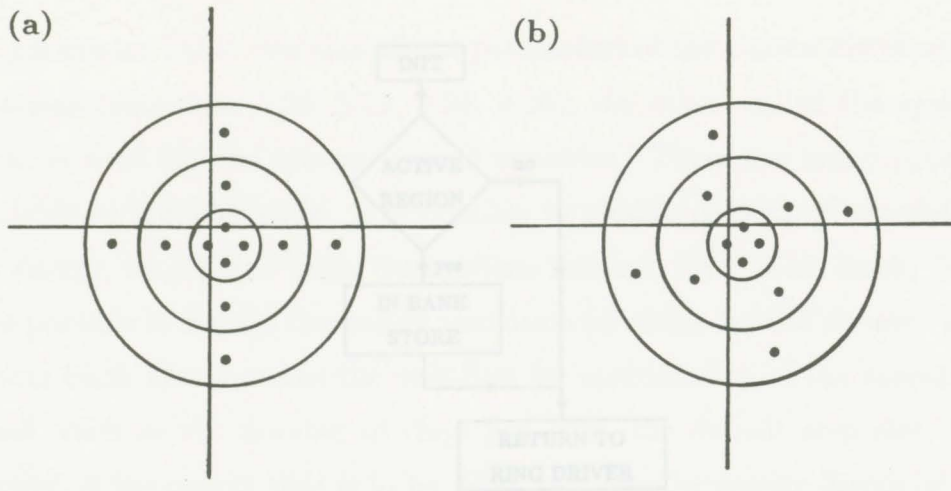


Figure 3.9: Axial view of the cone showing how the points are put into a ring a) without smearing and b) with angle smearing.

where the energy is to be deposited. The code then checks that the energy E_p deposited at each point is greater than a threshold energy E_T , which corresponds to the electronic threshold $E_T = 2$ MeV. Points with $E_p < E_T$ are not deposited. This was implemented to avoid the energy deposition of points with very low energy. For $E_p > E_T$, the code will enter the point driver (see figure 3.10) where after some initialization of various variables for the current point, the code checks if the point is in an active region of the detector. Recall that for the FSP there is no distinction between plates, tiles, and argon gaps, so that anywhere within the calorimeter is considered an active region. If the point is in an active region, the energy E_p is stored in memory, otherwise it is discarded.

After all the points in the rings and all the rings of the slice have been looped through, the code returns to the shower driver and checks if the energy deposited by the current shower is smaller than $E_{cut} = 0.999E_i$. If $E < E_{cut}$, the code will check if the boundary of the current region has been reached, in which case it will branch to the beginning of the region loop. If the region boundary has not been reached, the code loops back to the beginning of the slice loop. If $E > E_{cut}$, the code terminates the current

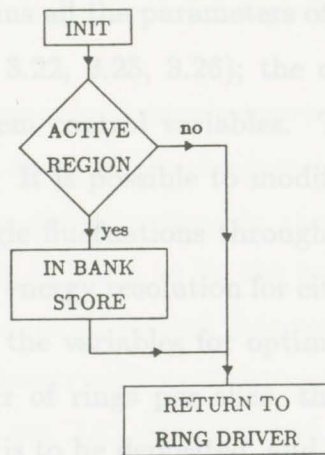


Figure 3.10: Flow chart of the point driver section of the FSP code.

There are a number of features and parameters which are not directly shower and returns to the beginning of the track loop to look for further tracks which require showering. Once all the tracks have been showered, GEANT will proceed with further digitization.

In figure 3.11, one can see the shower of a 5 GeV pion incident on the SLD calorimeter, as described with the simple geometry. The step size here is $5 X_0$. One can easily see the slice plane, and at some places the individual points. In figure 3.12 one can see the same shower, but this time with a zero energy threshold, $E_T = 0.0$, and with hits recorded in both active and inactive regions. In figure 3.13 one can see an electron shower of 5 GeV. It is easy to see here that the size of the electromagnetic shower is much smaller than the hadronic shower.

3.5.5 Features

In this section we will summarize and discuss some of the features of the FSP code, as well as the parameters available to control these features. In addition we will point out some areas where the prospective user must use caution. We will close with a discussion of possible future improvements to the code.

There are two arrays that control the FSP code execution: one, called

the parameter bank, contains all the parameters of the shower distribution functions (equations 3.20, 3.22, 3.25, 3.26); the other, called the system bank, is used for the system control variables. There are many options available in the FSP code. It is possible to modify or turn off separately the energy, length and angle fluctuations through the system bank. It is thus possible to change the energy resolution for either type of shower. The system bank also contains the variables for optimization of the execution speed, such as the number of rings per slice, the default step size, the fraction of the energy that is to be deposited, and the energy threshold for a shower hit.

There are a number of features and parameters which are not directly controlled by bank variables, but which can easily be modified by minor changes to the code. As discussed earlier in section 2.5.1, a hadronic shower signal is suppressed relative to the electromagnetic signal by the energy dependent ratio

$$\pi/e = 0.85 + 0.0009E_i.$$

The FSP code takes this into account by reducing the amount of energy deposited at each point by the appropriate amount (see equation 3.29). The probability P_{ce} of charge exchange is assumed to be constant in the code with a value of 3%. This value could easily be made energy dependent. As presently written, the default step size is a constant. This could, however, easily be modified so that the step size would be a function of the shower depth. One could then, for instance, use a larger step size in the tail of the shower where the energy density is low. Note that it is also possible to change the parametrization functions of the shower shape quite easily.

It is worth pointing out here a few areas where the user must use caution. It is difficult to reduce the time for simulating a shower by using a large step size without losing the gaussian character of the length and energy distributions. Therefore one has to choose carefully the default step size so

that one has a fast code while still maintaining realistic physical quantities of the shower.

The FSP code still has room for future improvements which will enable it to better simulate showers in the SLD calorimeter. One such improvement would be the introduction of fluctuations in the transverse distribution. The WIC energy resolution is taken to be the same as the hadronic part of the LAC; this is not true in the actual detector, but the difference was not implemented. The parametrizations of the various shower distributions are presently derived from the UA1 detector data. Those parameters were not tuned for the LAC. However test data with a prototype similar in construction to the LAC support the use of the UA1 parameters.

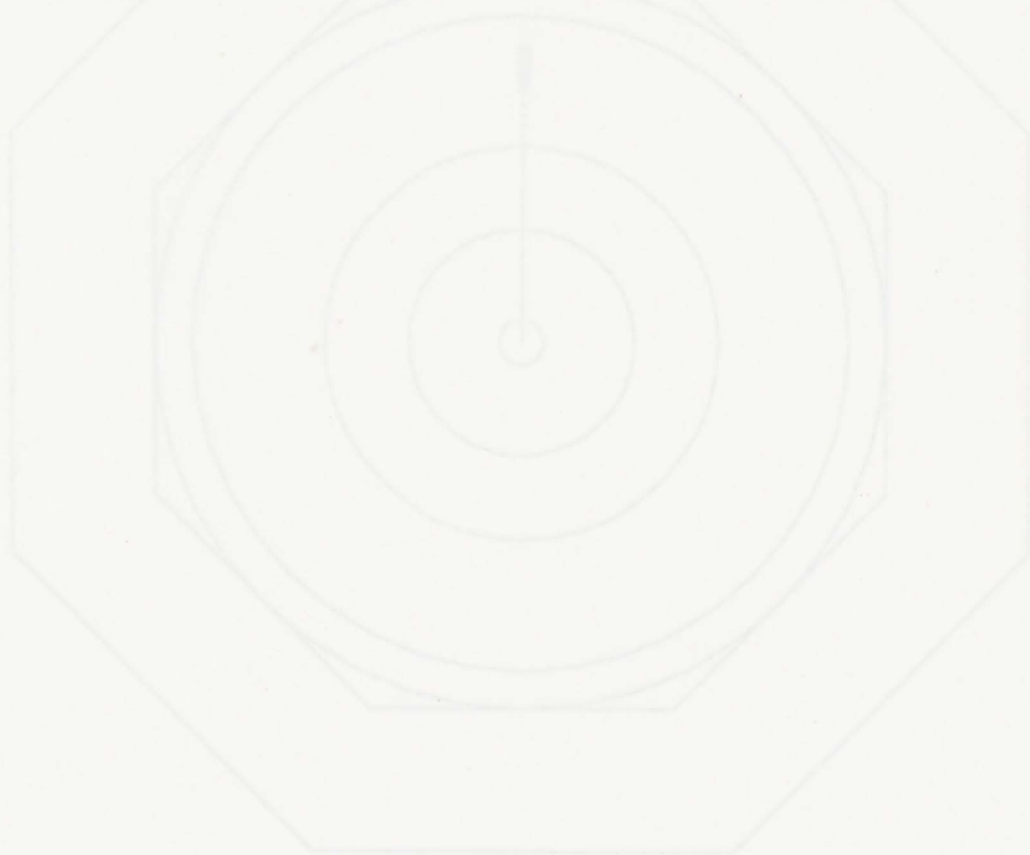


Figure 3.11: A 5 GeV e^- simulated using the FSP code with a step size of 5×10^{-3} cm.

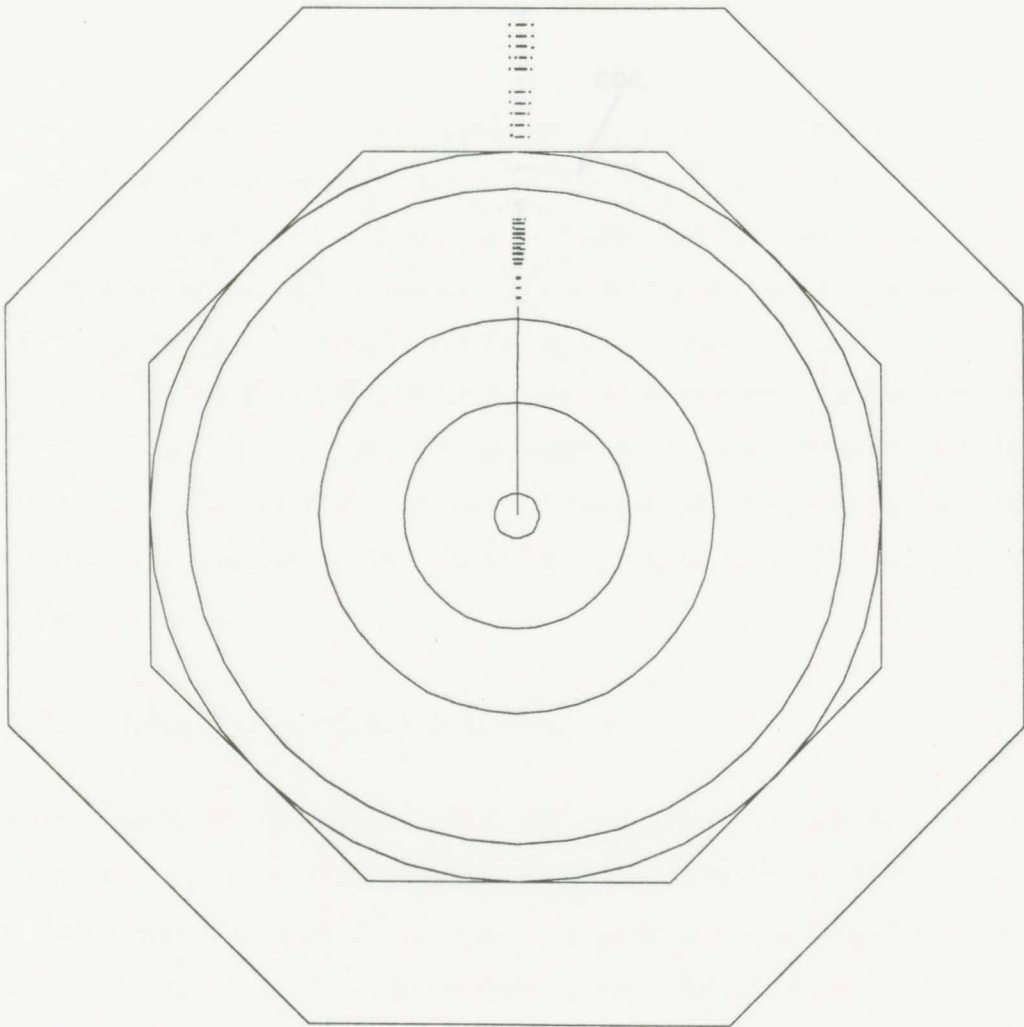


Figure 3.11: A 5 GeV π^- simulated using the FSP code with a step size of $5 X_0$.

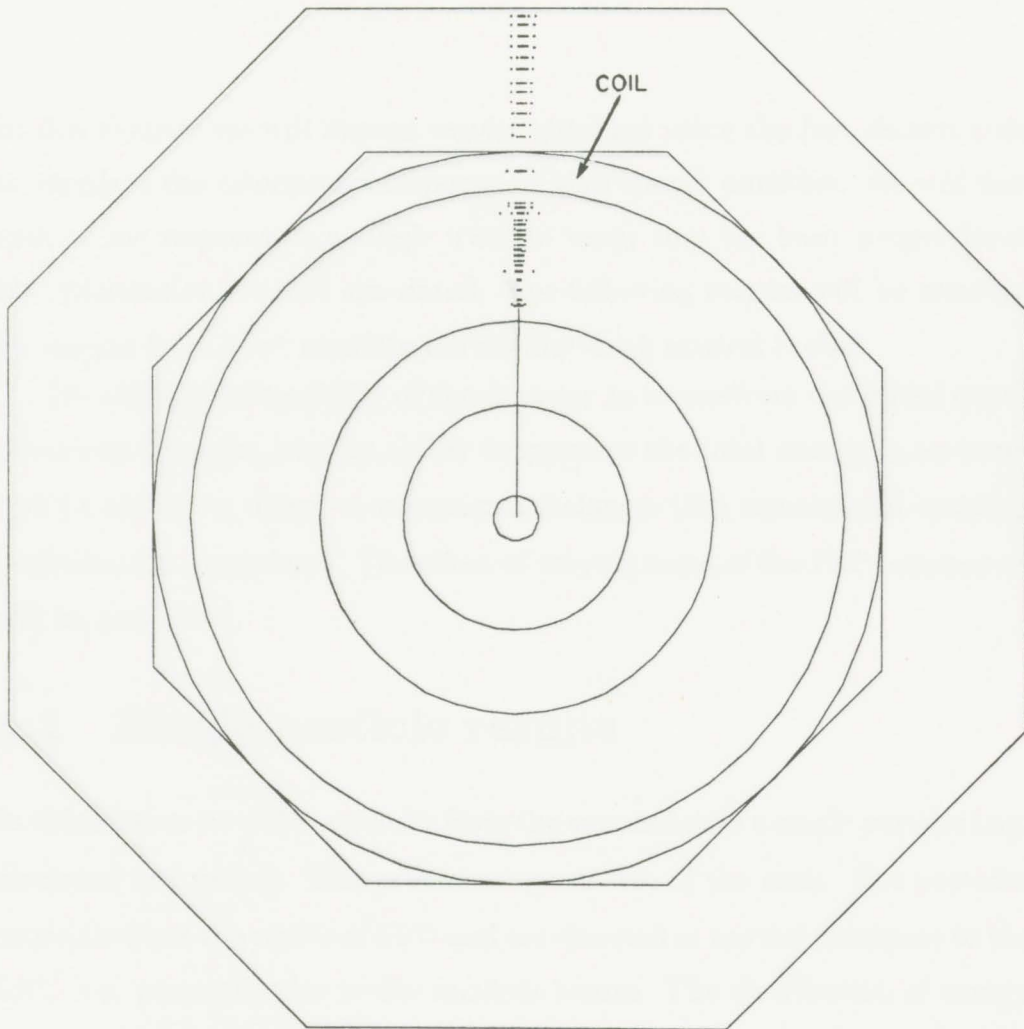


Figure 3.12: Same as previous section but with no threshold and hits in inactive regions. The coil is an inactive region and is indicated in the figure.

Chapter 4

Results

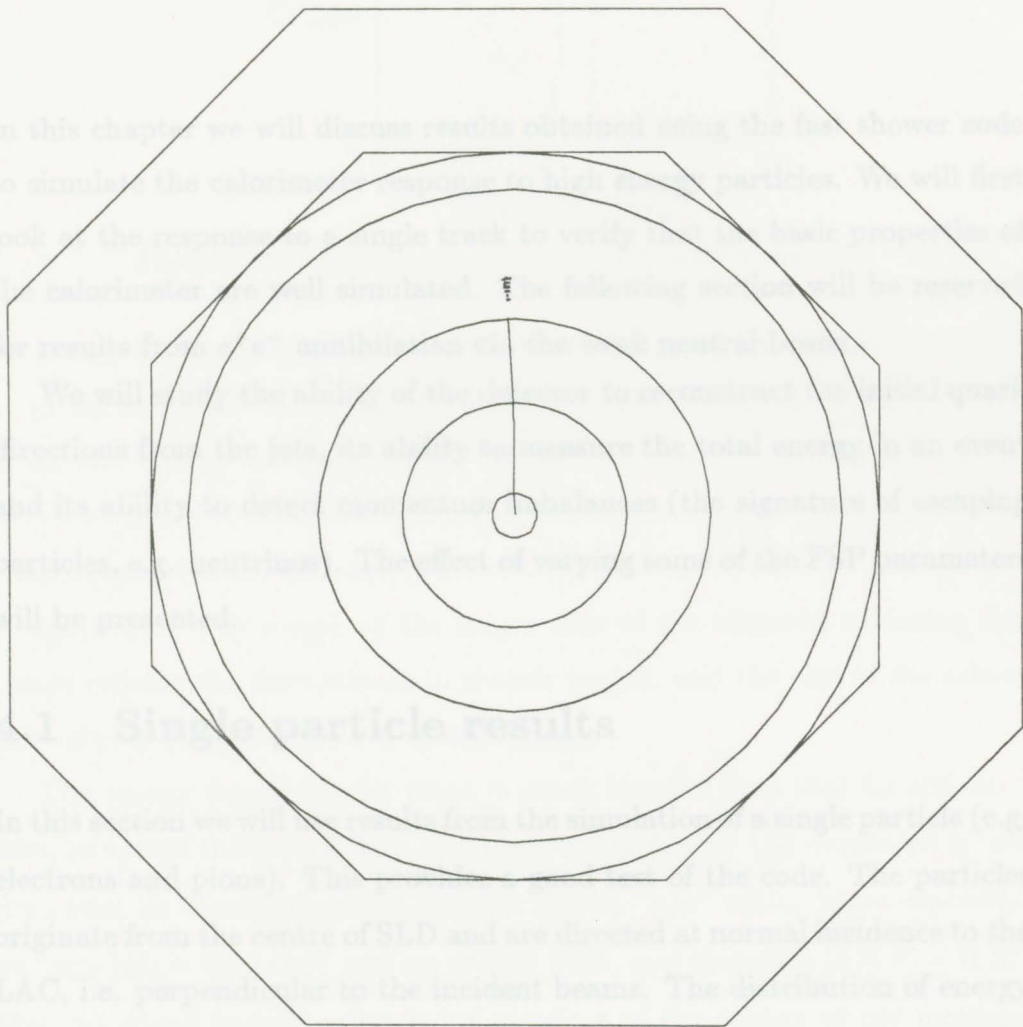


Figure 3.13: A 5 GeV e^- simulated using the FSP code.

Chapter 4

Results



In this chapter we will discuss results obtained using the fast shower code to simulate the calorimeter response to high energy particles. We will first look at the response to a single track to verify that the basic properties of the calorimeter are well simulated. The following section will be reserved for results from e^+e^- annihilation via the weak neutral boson.

We will study the ability of the detector to reconstruct the initial quark directions from the jets, its ability to measure the total energy in an event and its ability to detect momentum imbalances (the signature of escaping particles, e.g. neutrinos). The effect of varying some of the FSP parameters will be presented.

4.1 Single particle results

In this section we will use results from the simulation of a single particle (e.g. electrons and pions). This provides a good test of the code. The particles originate from the centre of SLD and are directed at normal incidence to the LAC, i.e. perpendicular to the incident beams. The distribution of energy deposited in the calorimeter for 5 GeV electrons is shown in figure 4.1. The average energy is $\langle E \rangle = 4.95$ GeV with a standard deviation $\sigma_E = 0.22$ GeV. It is interesting to look at the energy deposition in the individual longitudinal segments of the calorimeter. The electron deposits almost all

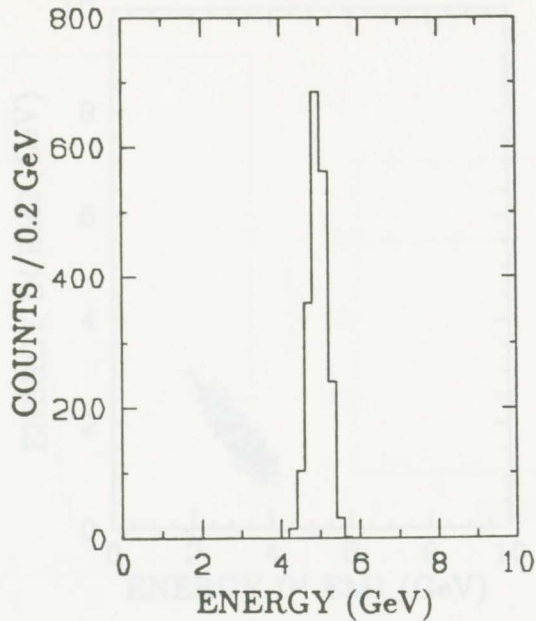


Figure 4.1: Calorimeter response to 5 GeV electrons.

its energy in the first 2 layers (total depth $21X_0$) of the calorimeter, that is, in the so called “electromagnetic calorimeter”. Even at 10 GeV, 99.9% of all the energy is contained in the electromagnetic calorimeter. It is also interesting to look at the energy correlation between the first and the second layers ($EM1=6X_0$ and $EM2=15X_0$); the results for 5 GeV are shown in figure 4.2. The length of the major axis of the ellipsoid enclosing the points reflects the fluctuations in shower length, and the size of the minor axis reflects fluctuations in detected energy.

The energy deposition for pions is much broader than that for the electron, as shown in figure 4.3(a), and the average energy $\langle E \rangle$ deposited is less than that for electromagnetic showers by the “ π/e ” ratio. More explicitly we have $\langle E \rangle = 3.63$ GeV and $\sigma_E = 0.95$ GeV, and therefore $(\pi/e)^m = 0.73$. This measured $(\pi/e)^m$ value is independent of the energy of the incident particle, as shown in figure 4.3(b). Since most of the time pions will deposit energy in the hadronic calorimeter it is interesting to look at the correlation between the energy in EMC ($EM1 + EM2 = 0.84\lambda$) and in HADC

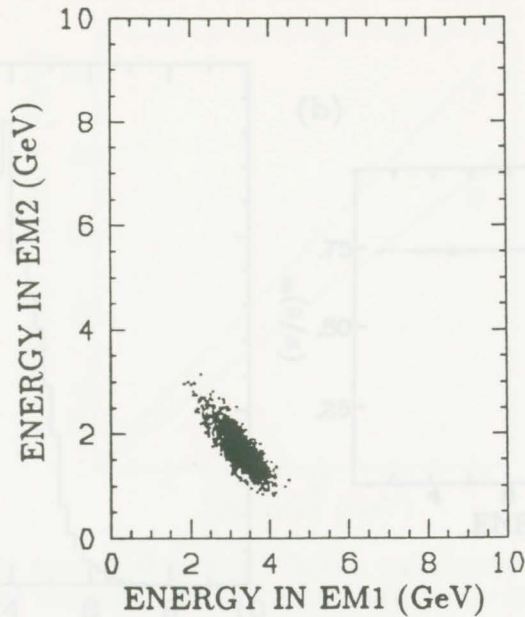


Figure 4.2: Energy deposited in first layer vs energy deposited in the second layer of the electromagnetic calorimeter for 5 GeV electrons.

($HAD1 + HAD2 = 2.0\lambda$), as shown in figure 4.4. Here we see a vertical stripe with little energy in EMC. These are events that passed through the first two calorimeter sections as minimum ionizing particles. The entries in this stripe at low values of HADC energy also failed to interact in the next two layers of the calorimeter. The width of the remaining distribution reflects the poorer hadronic resolution. The points at high values of EMC energy and very low energy in HADC are events where a pion exchange reaction produces a π^0 and hence only electromagnetic energy.

We can study the response of the detector as a function of the incident energy. As mentioned in the previous chapter, $\langle E \rangle$ should be linear with the kinetic energy E_i of the incoming particle. This is well reproduced by the code for both electromagnetic and hadronic energy, as shown in figure 4.5. Furthermore the resolution R of the shower, given by

$$R = \sigma_E / E_i, \quad (4.1)$$

should be linear with $E_i^{-1/2}$. In figure 4.6 one can see that for electrons the

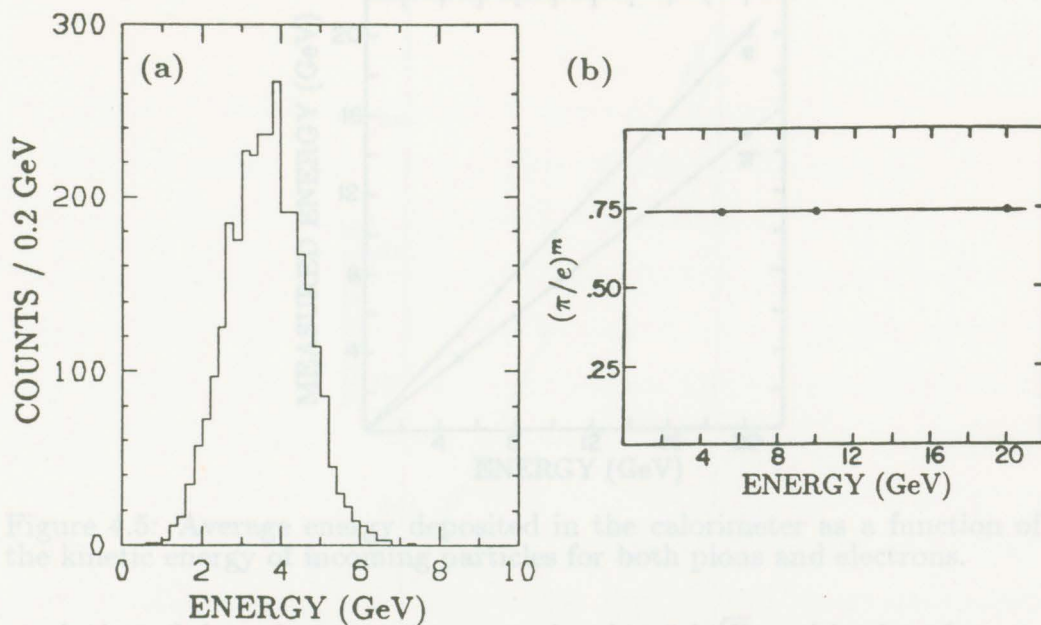


Figure 4.3: (a) Calorimeter response to 5 GeV pions. (b) $(\pi/e)^m$ as a function of the incident energy.

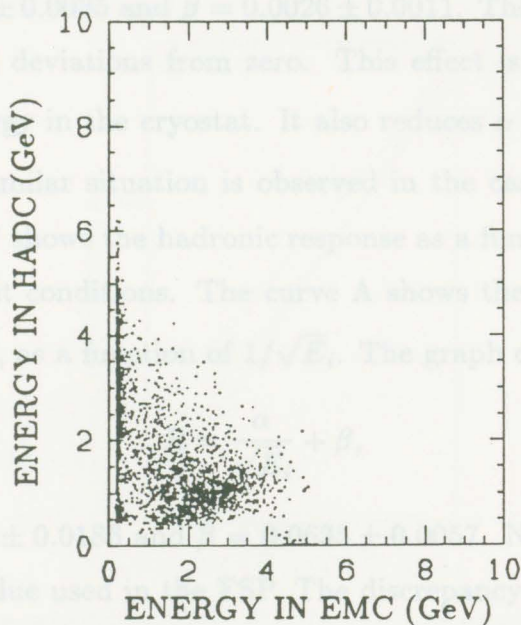


Figure 4.4: Energy deposited in the hadronic calorimeter vs the energy in the electromagnetic calorimeter for 5 GeV pions.

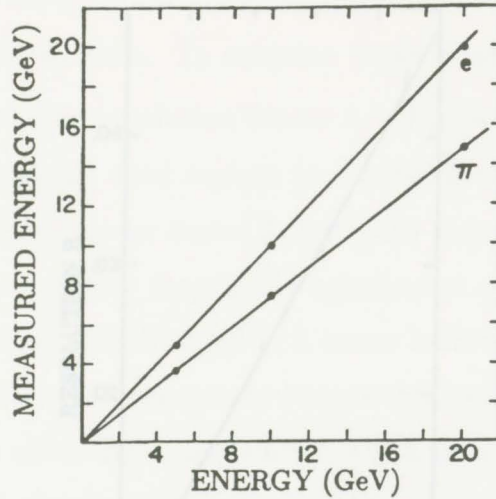


Figure 4.5: Average energy deposited in the calorimeter as a function of the kinetic energy of incoming particles for both pions and electrons.

resolution of the calorimeter is proportional to $1/\sqrt{E_i}$ and is given by

$$R = \frac{\alpha}{\sqrt{E_i}} + \beta, \quad (4.2)$$

where $\alpha = 0.0922 \pm 0.0035$ and $\beta = 0.0026 \pm 0.0011$. The intercept is more than 2.5 standard deviations from zero. This effect is significant and is due to loss of energy in the cryostat. It also reduces α from $10\%/\sqrt{E_i}$ to $9.2\%/\sqrt{E_i}$. A similar situation is observed in the case of the hadronic shower. Figure 4.7 shows the hadronic response as a function of the initial energy for different conditions. The curve A shows the resolution, calculated with no cuts, as a function of $1/\sqrt{E_i}$. The graph can be fitted by

$$R = \frac{\alpha}{\sqrt{E_i}} + \beta, \quad (4.3)$$

where $\alpha = 0.4397 \pm 0.0186$ and $\beta = 0.0635 \pm 0.0057$. Note that the slope is not 0.55, the value used in the FSP. The discrepancy between the measured and expected resolution can be explained by the fact that there is some energy lost in dead regions, there is some energy lost before the beginning of the shower, and there is some energy lost out the back of the

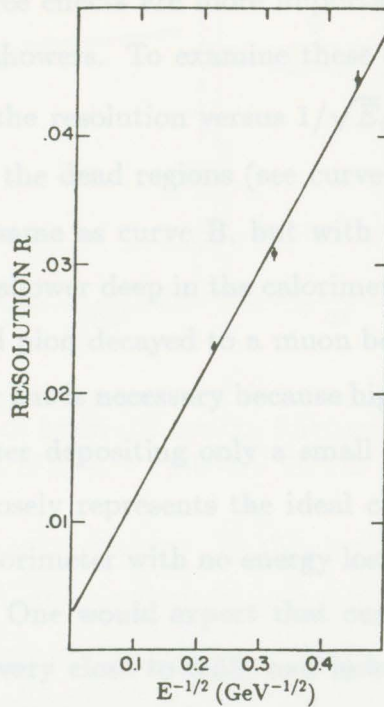


Figure 4.6: Energy resolution of electromagnetic showers vs the incident energy.

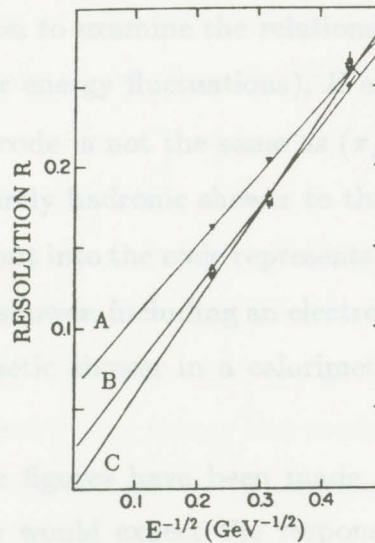


Figure 4.7: Energy resolution of hadronic showers vs the incident energy. The line A is the resolution as measured without any cuts. The line B is calculated using the energy in the dead regions and C by using the dead regions and also by demanding an early shower and no muons from pion decay.

calorimeter. These three effects are more important for hadronic showers than electromagnetic showers. To examine these effects we have plotted, for hadronic showers, the resolution versus $1/\sqrt{E_i}$, but with the addition of energy deposited in the dead regions (see curve B of figure 4.7). Curve C of figure 4.7 is the same as curve B, but with a cut to exclude events where a pion began to shower deep in the calorimeter, and a cut to exclude events where a charged pion decayed to a muon before initiating a shower (about 1%). The latter cut is necessary because high energy muons usually escape the detector after depositing only a small fraction of their energy. Thus curve C most closely represents the ideal case where the shower is fully contained in a calorimeter with no energy lost before the showers and with no dead regions. One would expect that curve C would have a zero intercept and a slope very close to 0.55, and indeed the measured values for the slope and intercept are 0.576 ± 0.036 and 0.0008 ± 0.011 , respectively. We have thus demonstrated that the code successfully simulates the expected behaviour for the resolution as a function of energy.

We will now move on to examine the relationship between parameters such as σ (the hadronic energy fluctuations), R and π/e . Recall that the π/e ratio put into the code is not the same as $(\pi/e)^{int}$, which is the ratio of the response to a purely hadronic shower to that of an electromagnetic shower. The π/e ratio put into the code represents the ratio of the response of an average hadronic shower, including an electromagnetic component, to that of an electromagnetic shower in a calorimeter of infinite depth and having no dead regions.

The following three figures have been made using 5 GeV pions. In a real calorimeter, one would expect the response to a hadronic shower to be linear with $(\pi/e)^{int}$ and constant with σ . As seen in figures 4.8(a) and (b), this behaviour is reproduced well by the code. One can also see from the figure that the response becomes more independent of π/e when

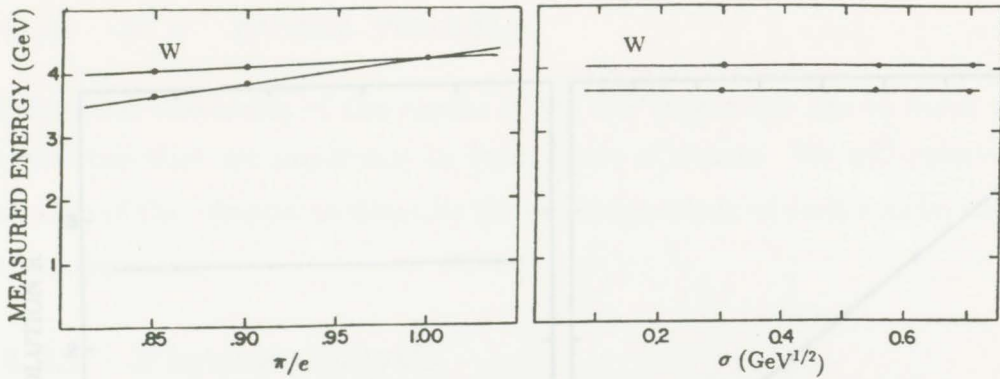


Figure 4.8: (a) Hadronic response as a function of π/e and (b) hadronic response as a function of hadronic energy fluctuations σ for 5 GeV pions. Curves denoted by a W are for a weighted energy scheme.

one uses a weighted energy scheme. In this method one realizes that it is very unlikely for a photon or electron to produce a shower deeper than EM1 and EM2. Therefore all the energy in HADC is weighted by $1/(\pi/e)$. This compensates the hadronic energy in HADC but hadronic energy in EMC is still underestimated. Since the parameters σ and π/e are totally independent in the code, one would expect the resolution to be constant with π/e and linear with σ . This behaviour is confirmed in figures 4.9(a) and (b). It should be pointed out, however, that in a real calorimeter the resolution should improve as $(\pi/e)^{int}$ approaches 1. This discrepancy does not pose a problem in the simulation as long as the parameters σ and π/e are kept at their physical values. In figures 4.10(a) and (b) are plotted the measured π/e ratio, denoted $(\pi/e)^m$, as a function of π/e and as a function of σ . We see that $(\pi/e)^m$ is linear with π/e as expected. The non-zero intercept can be explained by the energy loss mechanisms discussed earlier in this section. We also see that $(\pi/e)^m$ is constant with σ , which is what one would expect from the code.

Now that we understand the response of the code to single particle events, we can move on in the next section to investigate the simulation of full e^+e^- events.

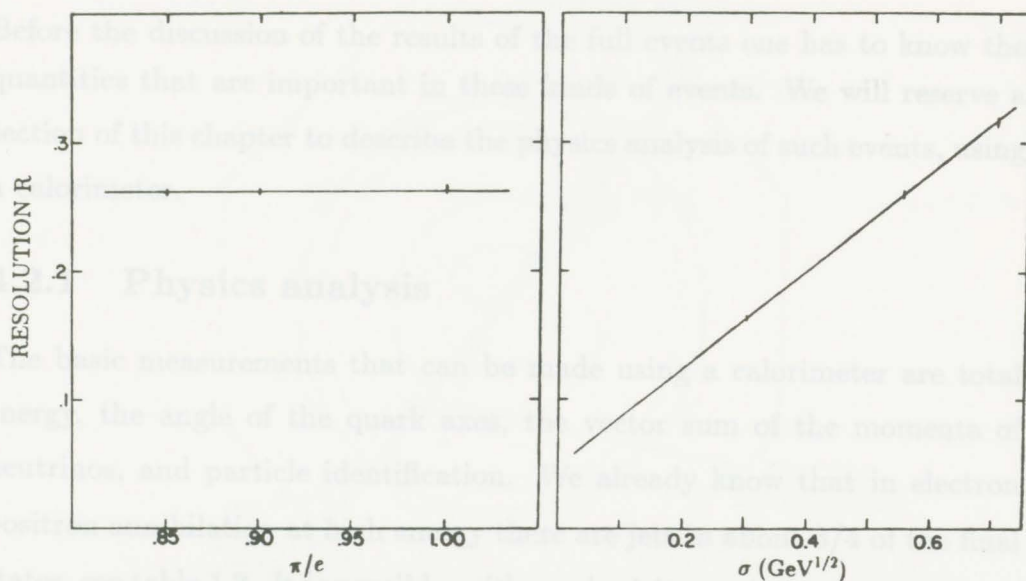


Figure 4.9: (a) Resolution as a function of π/e and (b) resolution as a function of hadronic energy fluctuations σ for 5 GeV pions. Note that for both figures the weighted curves overlap the unweighted ones.

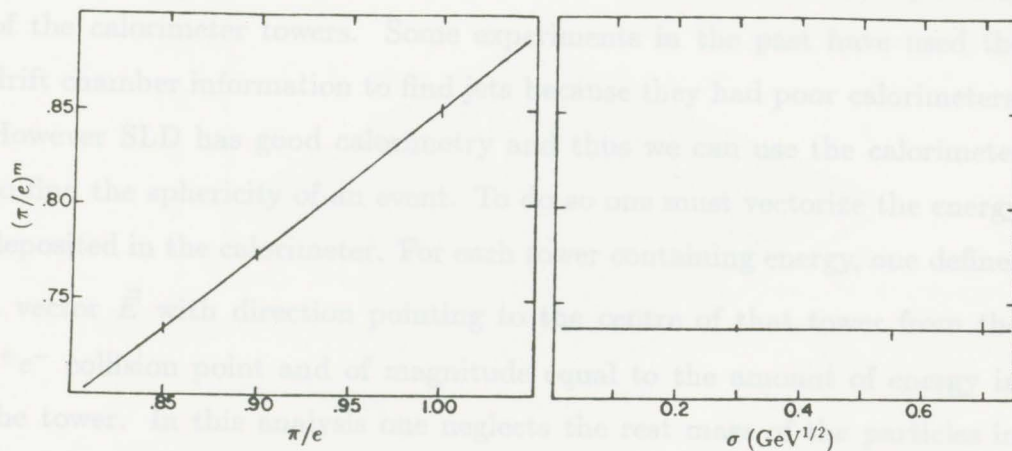


Figure 4.10: (a) $(\pi/e)^m$ as a function of π/e and (b) $(\pi/e)^m$ as a function of hadronic energy fluctuations σ for 5 GeV pions.

4.2 e^+e^- event results

Before the discussion of the results of the full events one has to know the quantities that are important in these kinds of events. We will reserve a section of this chapter to describe the physics analysis of such events, using a calorimeter.

4.2.1 Physics analysis

The basic measurements that can be made using a calorimeter are total energy, the angle of the quark axes, the vector sum of the momenta of neutrinos, and particle identification. We already know that in electron positron annihilation at high energy there are jets in about 3/4 of the final states, see table 1.3. It is possible, with a sphericity analysis, to reconstruct the axis of the quarks that initiated the jets. In the figure 4.11 one can see a simulated $b\bar{b}$ 2-jet event at 93 GeV, with the axis of the quarks plotted along with the calculated sphericity axis (to be defined later). One can also notice the showers generated by the FSP code. The jets can easily be seen in this picture and in figure 4.12 which shows a theta-phi map of the calorimeter towers. Some experiments in the past have used the drift chamber information to find jets because they had poor calorimeters. However SLD has good calorimetry and thus we can use the calorimeter to find the sphericity of an event. To do so one must vectorize the energy deposited in the calorimeter. For each tower containing energy, one defines a vector \vec{E} with direction pointing to the centre of that tower from the e^+e^- collision point and of magnitude equal to the amount of energy in the tower. In this analysis one neglects the rest mass of the particles in the jets. These vectors are then used to calculate the sphericity the same way as the momentum vectors which are measured by the drift chamber. Note that, unlike the drift chamber, a calorimeter is sensitive to neutral particles, therefore the information obtained with the calorimeter is more

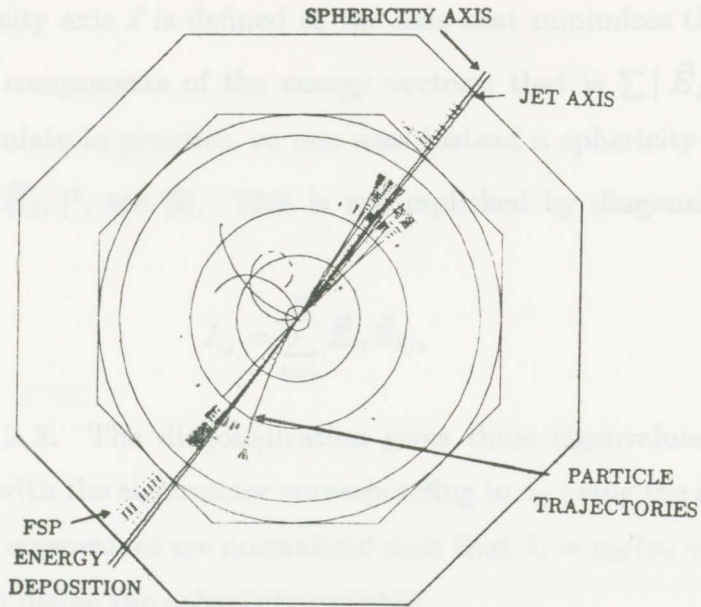


Figure 4.11: A simulated $b\bar{b}$ 2-jet event in SLD showing the jet axis and the sphericity axis. One can see the energy deposited by the showers generated by the FSP code.

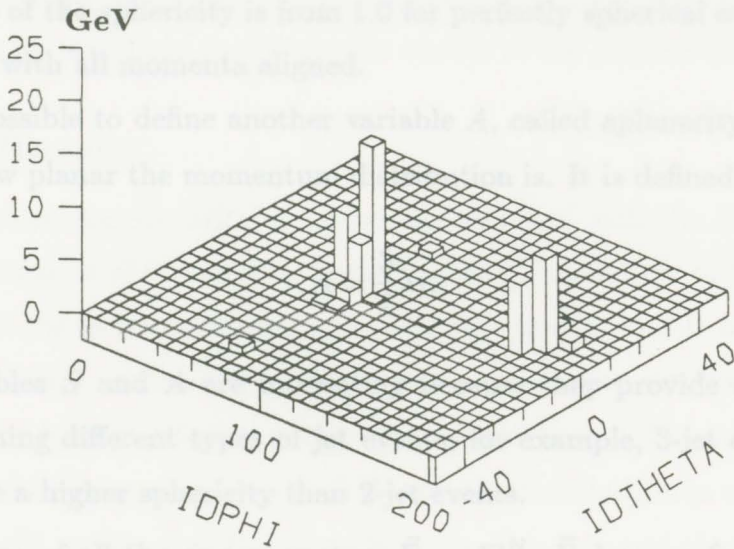


Figure 4.12: Calorimeter map showing which group of towers have energy deposited in them.

complete.

The sphericity axis \vec{s} is defined as the axis that minimizes the sum of perpendicular components of the energy vectors; that is $\sum |\vec{E}_{\perp i}|$. This is hard to calculate in practice, so one uses instead a sphericity axis that minimizes $\sum |\vec{E}_{\perp i}|^2$, see [8]. This is accomplished by diagonalizing the matrix

$$I_{ij} = \sum_{k=1}^N \vec{E}_{ki} \vec{E}_{kj}, \quad (4.4)$$

with $i, j = 1, 2, 3$. The diagonalization gives three eigenvalues denoted $n_1 \geq n_2 \geq n_3$, with the eigenvector corresponding to n_1 being the sphericity axis. Once the eigenvalues are normalized such that $\lambda_i = n_i / (n_1 + n_2 + n_3)$, it is possible to define the sphericity variable

$$S = \frac{3}{2}(\lambda_2 + \lambda_3). \quad (4.5)$$

The range of the sphericity is from 1.0 for perfectly spherical events to 0.0 for events with all momenta aligned.

It is possible to define another variable A , called aplanarity, which indicates how planar the momentum distribution is. It is defined as [37]

$$A = \frac{3}{2}\lambda_3. \quad (4.6)$$

The variables S and A are interesting because they provide a means of distinguishing different types of jet events; for example, 3-jet events have on average a higher sphericity than 2-jet events.

The sum of all the energy vectors $\vec{E}_s = \sum_{i=1}^N \vec{E}_i$ in a perfect hermetic calorimeter should give $\vec{0}$ for an event having no missing energy from neutrinos or other leaking particles. If there are neutrinos in the event then

there will be missing energy \vec{E}_m , given by

$$\vec{E}_m = - \sum_{i=1}^N \vec{E}_i. \quad (4.7)$$

Assume that in a given event there is only one neutrino, with momentum \vec{p}_ν given by

$$\vec{p}_\nu \cong \vec{E}_m, \quad (4.8)$$

and energy E_ν given by

$$E_\nu = E_m. \quad (4.9)$$

If there is more than one particle leaking energy in the event, then the vector sum of the leaking particles equals \vec{E}_m . However, because of the fluctuations in the energy measurement of events even without leaking particles, there will be some missing energy. This is defined as the intrinsic missing energy resolution.

Now that we know how to find the axis of jets and the momentum of neutrinos, we are ready to discuss the results of the physics analysis.

4.2.2 Results

In this last section we will discuss results obtained with the FSP code for the simulation of e^+e^- events at the Z^0 mass. The analysis of the events is made with the information from the calorimeter only and is based on the methods already outlined. We will divide the discussion into two parts, the leptonic and hadronic decays of the weak neutral boson. The total available energy in the centre-of-mass is 93 GeV and the distribution in $\cos \theta$ is given by $1 + \cos^2 \theta$, where θ is the angle between the axis and the beam pipe. 3000 events were used in the leptonic decay analysis and 1000 events were used in the hadronic decay analysis.

Leptonic decays

We know that about 28% of the time the Z^0 will decay into a pair of leptons and of these 11% decay through the e^+e^- channel. Because of its simplicity we use the e^+e^- channel to test the analysis program.

The signature of these events is two tracks diametrically opposed in the drift chamber with opposite charge and most of the energy deposited in the electromagnetic calorimeter. Sphericity analysis can be used to find the axis of the electron. In figure 4.13 one can see the angles between the calculated sphericity axes and the true event axes. As one can see, the axis can be found accurately with the calorimeter, with $\langle\theta\rangle = 0.47^\circ$ and $\sigma_\theta = 0.21^\circ$. One can use the sphericity axis to measure the θ distribution of

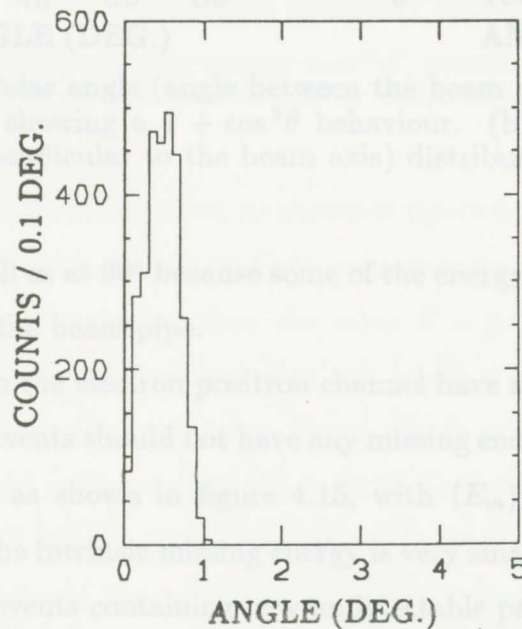


Figure 4.13: Angle between the sphericity axis and the event axis for leptonic final states.

the events. Using only information from the calorimeter it is not possible to determine the charge of the particle associated with each shower. This consequently leads to a forward/backward scattering ambiguity, so that the angle ranges only from 0° to 90° . The results are given in figure 4.14 and

show a $1 + \cos^2\theta$ behaviour. One should note that angles close to 0° cannot

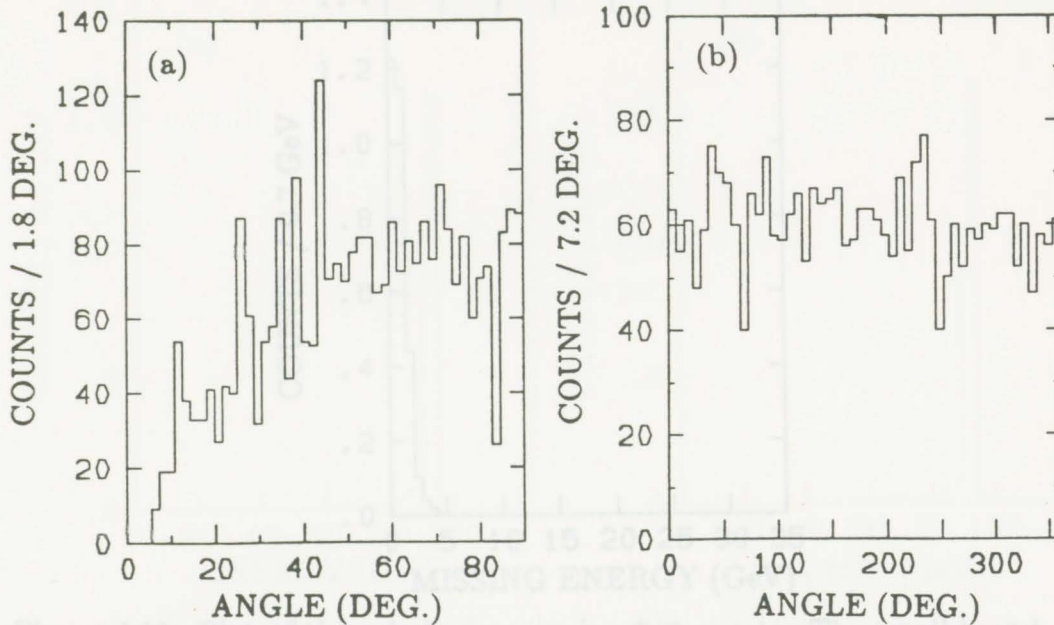


Figure 4.14: (a) Polar angle (angle between the beam pipe and the event axis) distribution showing a $1 + \cos^2\theta$ behaviour. (b) Azimuthal angle (in the plane perpendicular to the beam axis) distribution showing a flat behaviour.

be measured as well as at 90° because some of the energy escapes the active calorimeter down the beam pipe.

Decays through the electron positron channel have no leaking particles and therefore the events should not have any missing energy. This is indeed what is observed, as shown in figure 4.15, with $\langle E_m \rangle = 0.98$ GeV and $\sigma_m = 0.75$ GeV. The intrinsic missing energy is very small, making it easier to look for exotic events containing new undetectable particles.

The total amount of energy in the calorimeter should be 93 GeV, the mass of the Z^0 . However, many factors influence the amount of energy deposited in the calorimeter, such as ionization along the track and radiation emitted before interacting. These factors will act to reduce the average energy available for the showers. Furthermore if θ is small, much energy can be lost down the beam pipe. This can be seen in the plot of the total

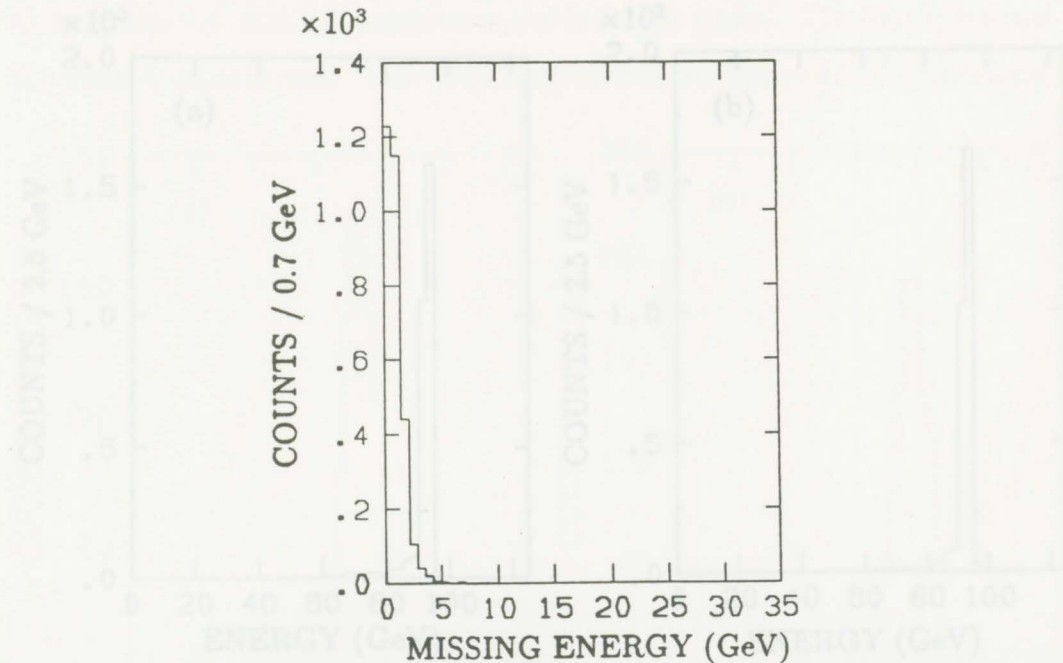


Figure 4.15: Plot of the missing energy in e^+e^- events. The small broadening of the spectrum comes from events in which some energy goes into the beam pipe.

energy deposited in the calorimeter, as shown in figure 4.16(a). The average energy is 91.45 GeV with $\sigma_E = 4.80$ GeV, corresponding to a resolution of $R = 0.053$. This is a lot higher than the value $R = 0.016$ predicted from equation 4.2. This is due to the low energy tail, which is largely attributable to energy leaking down the beam pipe. If one selects only events that have showers in the barrel region we get $\langle E \rangle = 92.88$ GeV and $\sigma_E = 0.98$ GeV, therefore, $R = 0.015$ which agrees with the single track run.

Figure 4.16(b) shows the total energy histogram corrected using the weighting scheme outlined above. There is a slight high energy tail that comes from the corrections. One of course would not expect a significant change in the histograms since almost all of the energy here is deposited in the electromagnetic calorimeter. Other than the slight modification to the total energy histogram, there are no noticeable effects from the weighting scheme. The leptonic events seem to be understood and we can now move

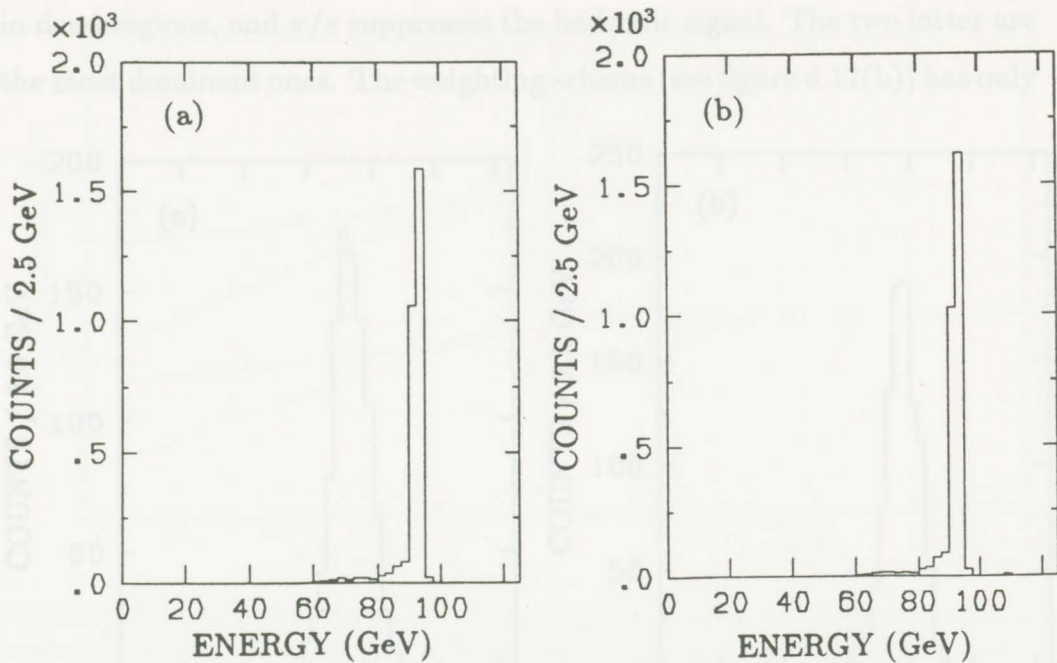


Figure 4.16: (a) Total energy deposited in the calorimeter for the e^+e^- channel. (b) Total energy using weighting scheme.

on to analyze more complex hadronic events.

Hadronic decays

In this section we will look at the detector response to hadronic events for specific final states of the Z^0 decay. We will focus our attention on 2-jet events, and will also look at the effects of gluon emission by one of the leading quarks, which leads to 3-jet events. We will look at two different quark flavours, a low mass $u\bar{u}$ and a high mass $b\bar{b}$, to get an idea of how much this changes the measured physical quantities.

The total energy deposited in the calorimeter for $u\bar{u}$ 2-jet events is shown in figure 4.17(a) with $\langle E \rangle = 72.6 \pm 0.2$ GeV. The total energy does not peak at 93 GeV because some of the energy is lost by collision or radiation before the particle reaches the calorimeter, the energy of the rest mass is not taken into account, there is energy leaking from the detector, there is energy loss

in dead regions, and π/e suppresses the hadronic signal. The two latter are the most dominant ones. The weighting scheme (see figure 4.17(b)) has only

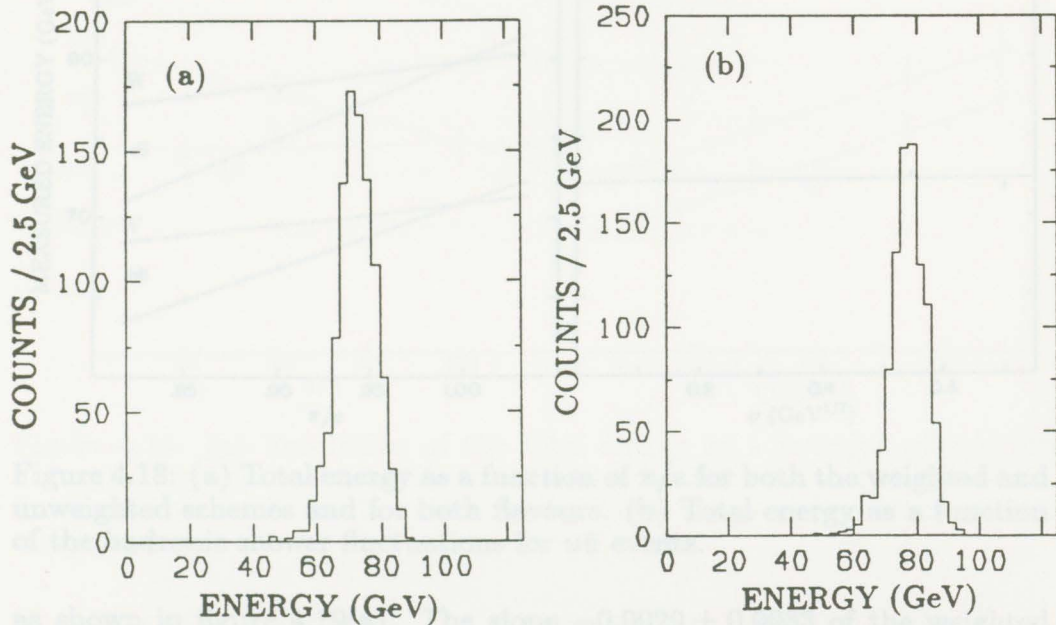


Figure 4.17: (a) Total energy deposited in the calorimeter for $u\bar{u}$ 2-jet events at 93 GeV. (b) total energy deposited, corrected using the weighting scheme.

a partial effect on the total energy, $\langle E \rangle_W = 77.4 \pm 0.2$ GeV, since some of the hadronic energy is deposited into the EM calorimeter and therefore not corrected. On average about 63% of the energy is deposited in the electromagnetic section. Figure 4.18(a) shows the average total energy deposited as a function of π/e for both the weighted and unweighted schemes. If the correction was perfect the slope for the weighted plot should be zero. As one can see, however, the slope is not zero for the same reason as explained above. As expected, the average energy $\langle E \rangle$ deposited is independent of hadronic shower fluctuations, as shown in figure 4.18(b). As shown in figure 4.18(a) the average energy deposited is lower for $b\bar{b}$ than $u\bar{u}$ because in b events there are high-energy neutrinos escaping the detector; the high energy neutrinos are discussed in more detail below.

There is only a small dependence of the resolution on the π/e ratio,

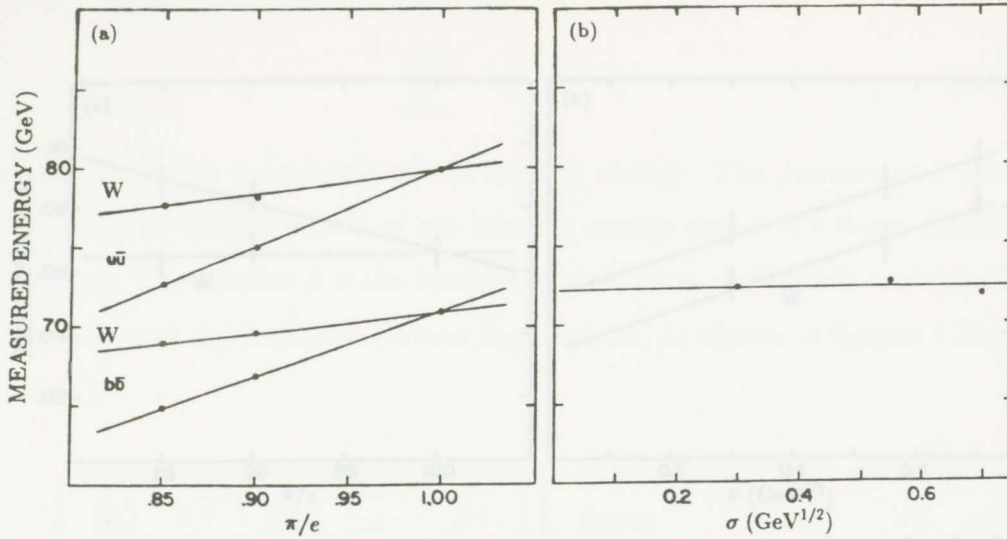


Figure 4.18: (a) Total energy as a function of π/e for both the weighted and unweighted schemes and for both flavours. (b) Total energy as a function of the hadronic shower fluctuations for $u\bar{u}$ events.

as shown in figure 4.19(a). The slope -0.0029 ± 0.0033 of the weighted curve indicates that the effect is corrected by the weighting scheme. This shows again that the two parameters are independent in the FSP code. The resolution of the total energy gets better when one decreases the hadronic fluctuations, as expected. This can be seen in figure 4.19(b).

The missing energy spectrum, as shown in figure 4.20(a) for $u\bar{u}$ events, shows the intrinsic resolution for the missing energy, where there should not be any high energy neutrinos. The Standard Model does not predict high energy neutrinos in $u\bar{u}$ events. Each component of the missing energy vector has a Gaussian distribution. This can be seen, for example, in figure 4.20(b) for the x component for $u\bar{u}$ events. Note that the distribution is centred about the origin, $\langle E_x^m \rangle = 0$. We have also found that the magnitude of the vector sum of the three components, as expected from the Central Limit Theorem, will result in an exponential distribution. We can fit the missing

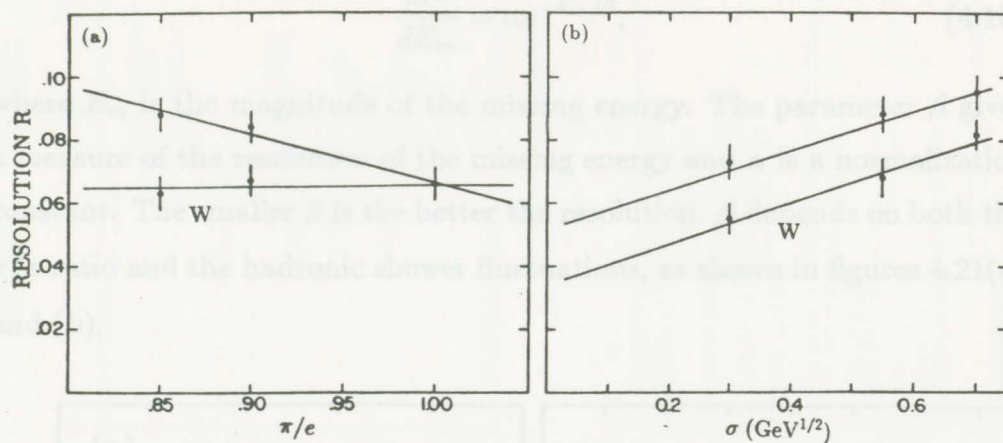


Figure 4.19: (a) Resolution of the total energy as a function of π/e for u events. (b) Resolution of the total energy as a function of the intrinsic hadronic shower fluctuations for $u\bar{u}$ for both the weighted and the un-weighted schemes.

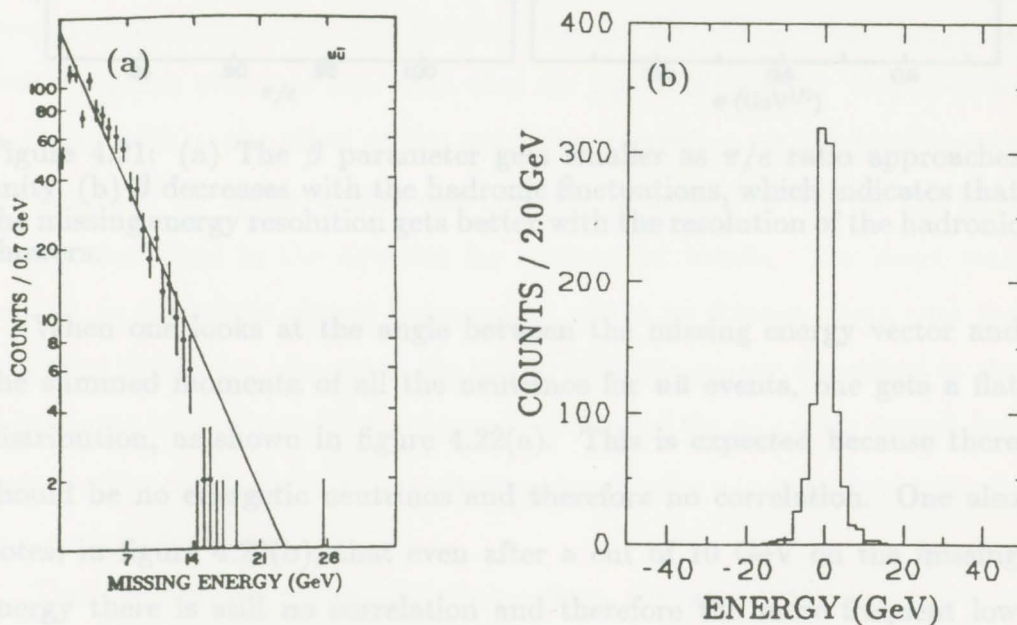


Figure 4.20: (a) Missing energy spectrum for up quark events. (b) Histogram of the x component of the missing energy for up quark events.

energy distribution with the function

$$\frac{dN}{dE_m} = \alpha e^{-E_m/\beta}, \quad (4.10)$$

where E_m is the magnitude of the missing energy. The parameter β gives a measure of the resolution of the missing energy and α is a normalization constant. The smaller β is the better the resolution. β depends on both the π/e ratio and the hadronic shower fluctuations, as shown in figures 4.21(a) and (b).

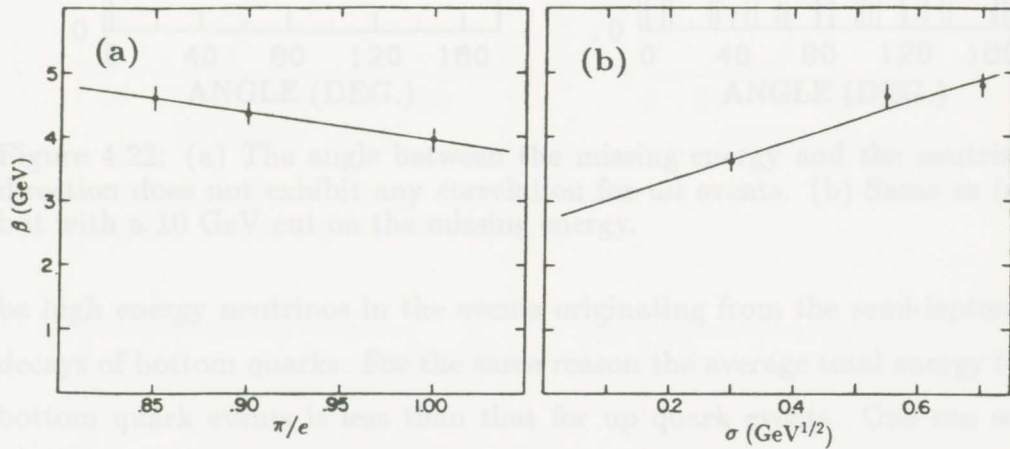


Figure 4.21: (a) The β parameter gets smaller as π/e ratio approaches unity. (b) β decreases with the hadronic fluctuations, which indicates that the missing energy resolution gets better with the resolution of the hadronic showers.

When one looks at the angle between the missing energy vector and the summed momenta of all the neutrinos for $u\bar{u}$ events, one gets a flat distribution, as shown in figure 4.22(a). This is expected because there should be no energetic neutrinos and therefore no correlation. One also notes, in figure 4.22(b), that even after a cut of 10 GeV on the missing energy there is still no correlation and therefore the more frequent low energy neutrinos are not obscuring a possible signal.

The total energy for $b\bar{b}$ events has a more pronounced low energy tail than for $u\bar{u}$ events, as shown in figure 4.23(a). This is because there can

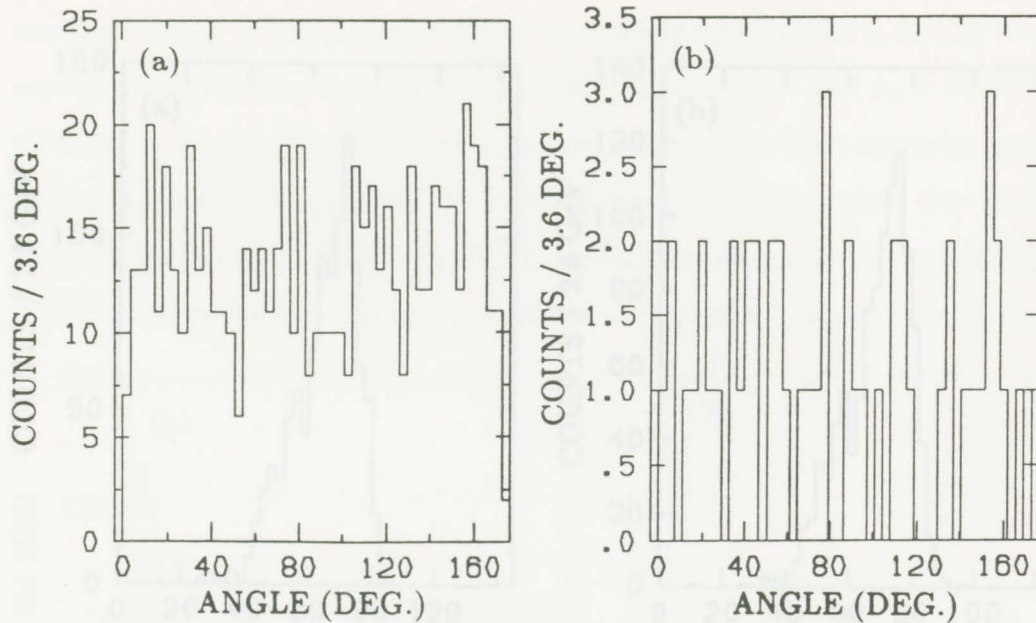


Figure 4.22: (a) The angle between the missing energy and the neutrino direction does not exhibit any correlation for $u\bar{u}$ events. (b) Same as (a) but with a 10 GeV cut on the missing energy.

be high energy neutrinos in the events originating from the semi-leptonic decays of bottom quarks. For the same reason the average total energy for bottom quark events is less than that for up quark events. One can see in figure 4.23(b) the effect of the weighting correction on the total energy distribution. In figure 4.18(a) one can see the effects of π/e on the total energy deposited in the detector for bottom jet events. The slope with respect to the π/e is almost independent of the jet flavour. Note that the weighted slopes are also much the same, with the energy deposited in the calorimeter increasing with the increasing value of the π/e ratio though less steeply. The resolution for $b\bar{b}$ events improves as the π/e ratio goes towards one, as for $u\bar{u}$ events.

The high-energy neutrinos coming from the semi-leptonic decays in bottom quark events can easily be seen in the missing energy plots, figures 4.24(a) and (b). The distribution of each component of the missing energy for $b\bar{b}$ events is broader than for $u\bar{u}$ events. The angle θ between the

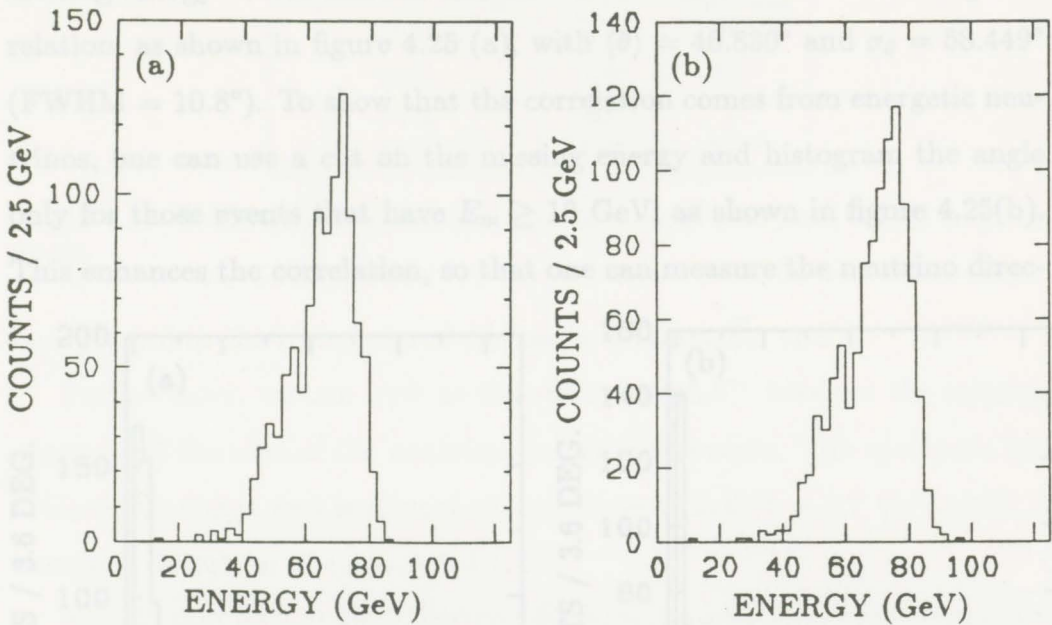


Figure 4.23: (a) Total energy distribution for $b\bar{b}$ events. (b) Same as (a) but using the weighting correction.

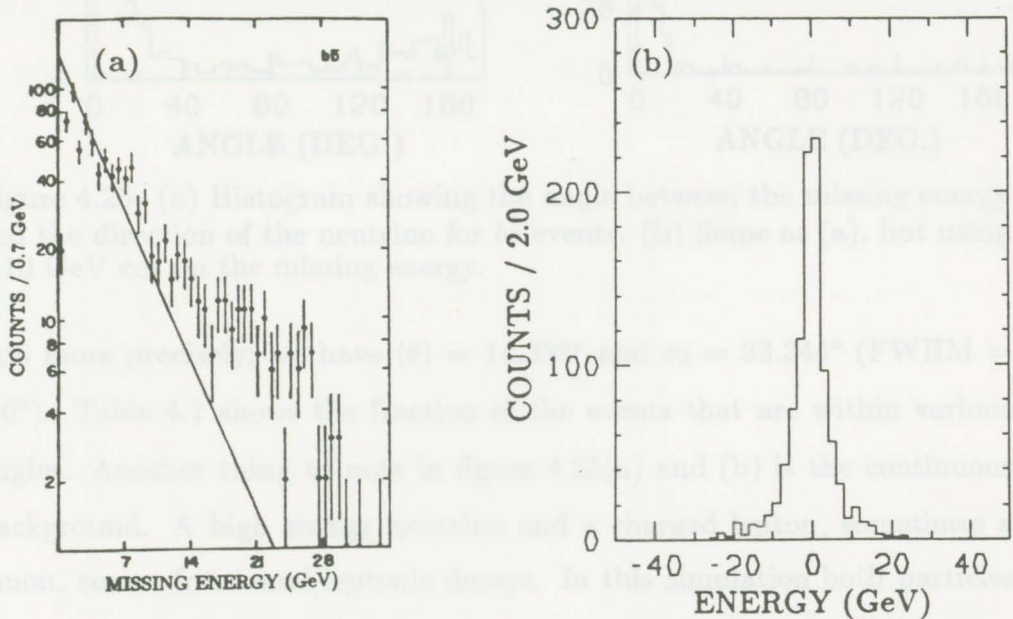


Figure 4.24: (a) Missing energy spectrum for $b\bar{b}$ events. The solid line represents the intrinsic resolution. One can easily see the neutrino effects above the intrinsic resolution. (b) Spectrum of the x component of the missing energy vector.

missing energy vector and the neutrino momentum exhibits a strong correlation, as shown in figure 4.25 (a), with $\langle\theta\rangle = 46.830^\circ$ and $\sigma_\theta = 58.449^\circ$ (FWHM = 10.8°). To show that the correlation comes from energetic neutrinos, one can use a cut on the missing energy and histogram the angle only for those events that have $E_m \geq 10$ GeV, as shown in figure 4.25(b). This enhances the correlation, so that one can measure the neutrino direc-

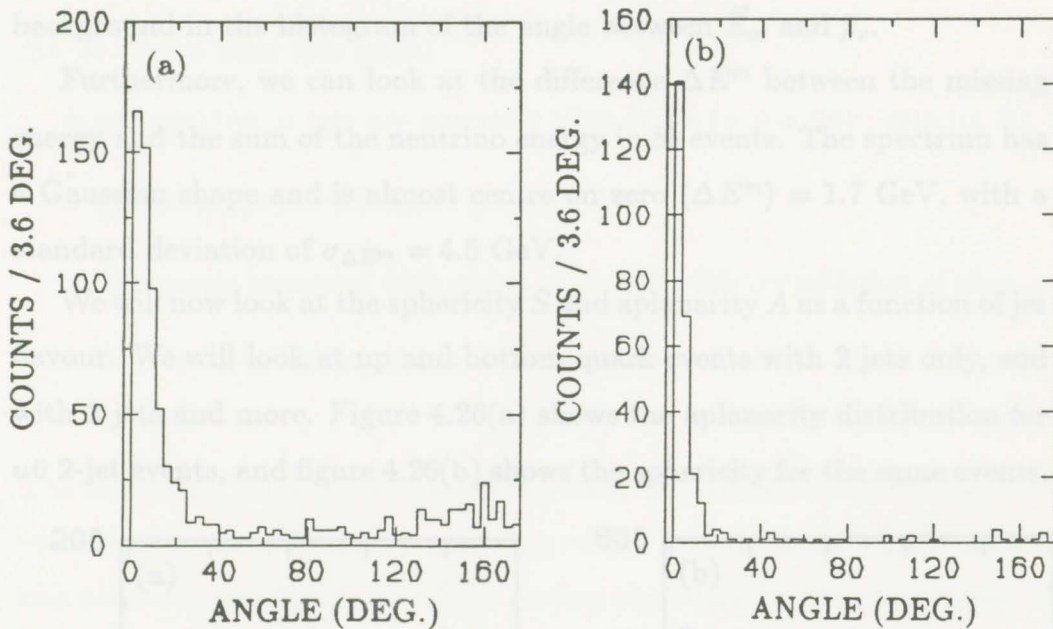


Figure 4.25: (a) Histogram showing the angle between the missing energy and the direction of the neutrino for $b\bar{b}$ events. (b) Same as (a), but using a 10 GeV cut on the missing energy.

tion more precisely; we have $\langle\theta\rangle = 14.338^\circ$ and $\sigma_\theta = 33.344^\circ$ (FWHM = 3.6°). Table 4.1 shows the fraction of the events that are within various angles. Another thing to note in figure 4.25(a) and (b) is the continuous background. A high energy neutrino and a charged lepton, sometimes a muon, comes from semi-leptonic decays. In this simulation both particles are penetrating because there is no muon momentum detector. If the muon carries a large fraction of the momentum compared to the neutrino, the missing energy vector will be correlated with the muon momentum rather than with the neutrino momentum. This will contribute to a continuous

fraction of events	no cut	with cut
90%	151°	25°
80%	119°	11°
75%	86°	7°
50%	10°	3.5°

Table 4.1: Table showing the fraction of events that are within a given angle.

background in the histogram of the angle between \vec{E}_m and \vec{p}_ν .

Furthermore, we can look at the difference ΔE^m between the missing energy and the sum of the neutrino energy in $b\bar{b}$ events. The spectrum has a Gaussian shape and is almost centre on zero $\langle \Delta E^m \rangle = 1.7$ GeV, with a standard deviation of $\sigma_{\Delta E^m} = 4.5$ GeV.

We will now look at the sphericity S and aplanarity A as a function of jet flavour. We will look at up and bottom quark events with 2 jets only, and with 2 jets and more. Figure 4.26(a) shows the aplanarity distribution for $u\bar{u}$ 2-jet events, and figure 4.26(b) shows the sphericity for the same events.

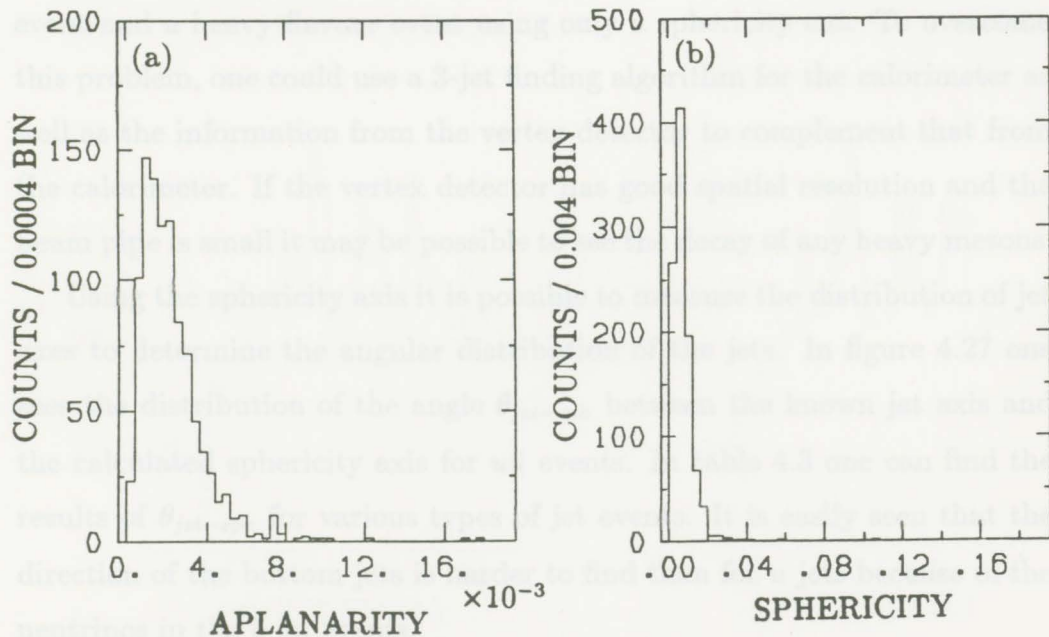


Figure 4.26: (a) Aplanarity distribution for $u\bar{u}$ events. (b) Sphericity distribution for $u\bar{u}$ events.

A summary of this analysis can be found in table 4.2. Some observations

event type	$\langle S \rangle$	σ_S	$\langle A \rangle$	σ_A
$u\bar{u}$	0.00761	0.00034	0.00213	0.00005
$u\bar{u}g$	0.03459	0.04261	0.00432	0.00351
$b\bar{b}$	0.01697	0.00055	0.00465	0.00013
$b\bar{b}g$	0.05111	0.04733	0.00756	0.00016

Table 4.2: Table giving the sphericity parameters for different types of jet.

can be drawn from this table:

- as expected, u jets are narrower than b jets (u jets have smaller S);
- gluons make the jet fatter (larger S);
- aplanarity increases with quark mass and with the addition of gluons;
- it is hard to distinguish a b jet from a u jet with a gluon from this analysis.

The last point shows that it would be hard to distinguish between a 3-jet event and a heavy flavour event using only a sphericity cut. To overcome this problem, one could use a 3-jet finding algorithm for the calorimeter as well as the information from the vertex detector to complement that from the calorimeter. If the vertex detector has good spatial resolution and the beam pipe is small it may be possible to see the decay of any heavy mesons.

Using the sphericity axis it is possible to measure the distribution of jet axes to determine the angular distribution of the jets. In figure 4.27 one sees the distribution of the angle $\theta_{jet-sph}$ between the known jet axis and the calculated sphericity axis for $u\bar{u}$ events. In table 4.3 one can find the results of $\theta_{jet-sph}$ for various types of jet events. It is easily seen that the direction of the bottom jets is harder to find than for u jets because of the neutrinos in the b jet events.

The distribution of the polar angle θ of the axes for up quark events is given in figure 4.28(a) and can be compared with the actual distribution of

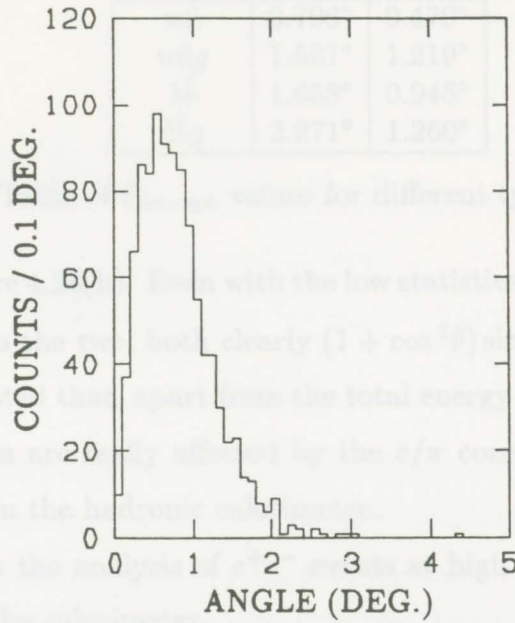


Figure 4.27: Angle between the jet axis and the reconstructed axis for $u\bar{u}$ events.

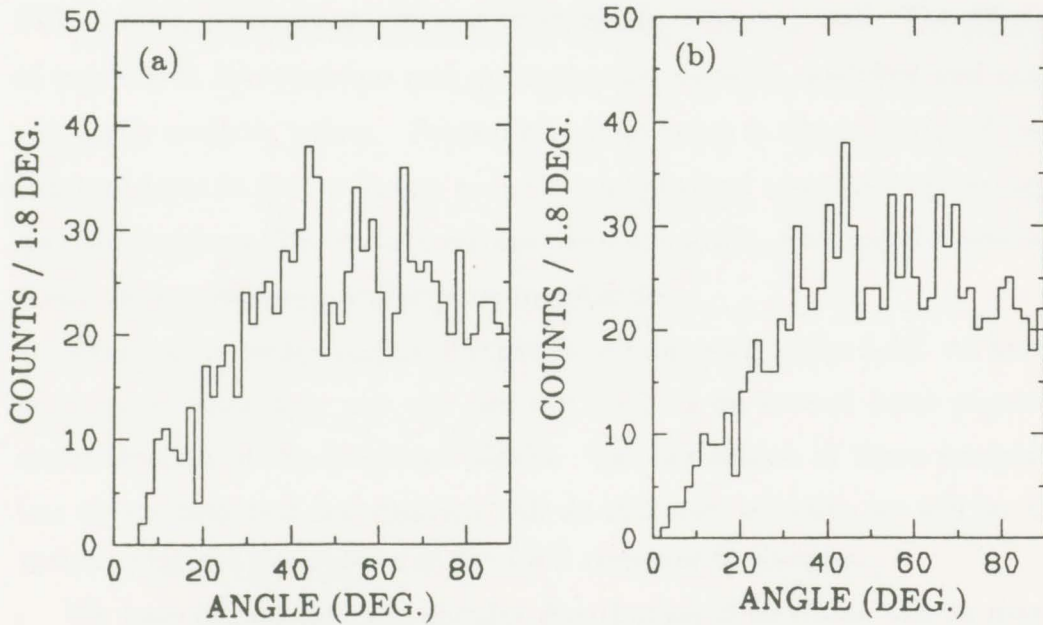


Figure 4.28: (a) Polar angle distribution of the sphericity axes for $u\bar{u}$ events. (b) The input (actual) distribution of the jet axes.

jet type	$\langle\theta\rangle$	σ_θ
$u\bar{u}$	0.796°	0.479°
$u\bar{u}g$	1.581°	1.219°
$b\bar{b}$	1.658°	0.945°
$b\bar{b}g$	2.271°	1.260°

Table 4.3: Table of $\theta_{jet-sph}$ values for different types of jets.

the jet axes in figure 4.28(b). Even with the low statistics there is reasonable agreement between the two, both clearly $(1 + \cos^2\theta) \sin\theta$.

It should be noted that, apart from the total energy and the resolution, no other quantities are really affected by the e/π correction made to the energy deposited in the hadronic calorimeter.

This completes the analysis of e^+e^- events at high energy using information based on the calorimeter.

Chapter 5

Conclusion

We have successfully implemented a fast simulation code for the interaction of high energy radiation with matter. The code is 2.5 times faster than the full simulation for 3 GeV hadronic showers and about 70 times faster for 3 GeV electromagnetic showers. Note that the time to simulate a shower using the full simulation program is linear with the incident energy whereas with the FSP it is almost constant. We have shown that this implementation of our fast shower parametrization reproduces the response of the SLD LAC to electromagnetic and hadronic showers very well. The effects of resolution, π/e response and geometry are correctly modelled and give physically realistic values. Particularly impressive is the addition of the constant term to the resolution as in the real physical case due to geometry and dead regions. The code is versatile and adaptable, allowing the user to easily vary parameters and explore possibilities.

Given an accurate means of reproducing showers in the LAC we have gone on to show how one can use the LAC to do several basic physics measurements of the Standard Model. The simulation of these analyses lets us see how well our detector will do and how sensitive we will be to various physical parameters of the LAC response to showers.

We have shown that the angular distribution of electrons can be measured with $\langle\theta\rangle = 0.5^\circ$, where θ is the angle between the axis measured with the calorimeter and the axis used to generate the event. This is a funda-

mental prediction of the Standard Model and comparison of the muon and electron angular distribution is an important test of lepton universality. Similarly, but more difficult to measure, the quark-antiquark angular distribution can be measured with $\langle\theta\rangle = 1.6^\circ$ for light quarks and $\langle\theta\rangle = 2.3^\circ$ for heavy quarks. There is no sensitivity to the π/e ratio or realistic values of the resolution for the angle measurements.

The identification of quark types through an analysis of the sphericity and the aplanarity looks very marginal. It may be possible to identify top decays if they do exist and have a mass on the order of 40 GeV. It looks most likely that heavy quarks can be tagged by an energetic neutrino in the case where they decay semi-leptonically. We have shown that the neutrinos can be detected by using the missing energy technique based on the conservation of momentum. Light quark-antiquark events were used to determine the missing energy resolution $\beta = 4.5$ GeV. As expected, We see that the resolution improves as π/e goes to 1 and as the hadronic energy resolution σ_H improves.

The heavy quark-antiquark events do show a clear excess of missing energy. If a cut on missing energy of 10 GeV is used to isolate a clean sample of semileptonic decays we find the direction of the neutrino can be measured with $\langle\theta_m\rangle = 14.3^\circ$, where θ_m is the angle between the missing energy vector and the total neutrino momentum.

We have shown that the fast shower parametrization code reproduces known physics well and can be used to study the response of the LAC to more complicated Z^0 final states.

[1] J. M. Doolin, *Rep. Prog. Phys.*, Vol. 46, 1983.

[9] Hanson, G. et al., *Physical Review Letters*, 35(1975) 1038.

[10] Doolin, J. M., SLAC PUB-3407(1984).

[11] Hanson, G. et al., *Phys. Lett.* 46(1973) 133.

Bibliography

- [1] Halzen, F. and Martin, A. D., "Quarks & Leptons", John Wiley & Sons, 1984.
- [2] Perkins, D. H., "Introduction to High Energy Physics", Addison-Wesley, 1982.
- [3] Aitchison, I. J. R. and Hey, A. J. G., "Gauge Theories in Particle Physics", Adam Hilger Ltd., 1982.
- [4] Close, F. E., "An introduction to Quarks and Partons", Academic Press, 1979.
- [5] Okun, L. B., "Leptons and Quarks", North Holland, 1982.
- [6] Quigg, C., "Gauge Theories of the Strong, Weak and Electromagnetic Interactions", The Benjamin/Cummings Publishing Company, 1983.
- [7] Particle Data Group, Review of Particle Properties, Physics Letters, Vol 170B, 1986.
- [8] Clegg, A. B., "An Experimental View of Jets", Rep. Prog. Phys., Vol 45, 1982.
- [9] Hanson, G. et al., Physical Review Letters, 35(1975) 1609.
- [10] Dorfan, J. M., SLAC-PUB-3407(1984).
- [11] Hasert, F. J. et al., Phys. Lett. 46b(1973) 138.

- [12] UA1 Collab., Arnison, G. et al., *Phys. Lett.* 122b(1983) 103.
- [13] UA1 Collab., Arnison, G. et al., *Phys. Lett.* 126b(1983) 398.
- [14] SLC Conceptual Design Report, SLAC-Report-229(1980)
- [15] SLD Design Report, SLAC-Report-273(1984)
- [16] Fabjan, C. W., CERN-EP/85-54.
- [17] Rossi, B., "High-Energy particles", Prentice Hall, New York (1964)
- [18] Fernow, R. C., "Introduction to Experimental Particle Physics", Cambridge University Press, Cambridge (1986).
- [19] Segrè, E., "Nuclei and Particle", The Benjamin/Cummings Publishing Company, Inc, London (1980).
- [20] Amaldi, U., *Physica Scripta*, Vol. 23, 409-424, 1981.
- [21] Wigmans, R., CERN-EP/86-141.
- [22] Leroy, C. et al., CERN-EP/86-66.
- [23] Fabjan, C. W. et al., *Nucl. Instr. and Methods* **141**, 61 (1977).
- [24] Gabriel, T. A., *Nucl. Instr. and Methods* **150**, 145 (1978).
- [25] Gabriel, T. A. and Schmidt W., *Nucl. Instr. and Methods* **134**, 271 (1976).
- [26] Hitlin, D. et al., *Nucl. Instr. Methods* 137,225(1976).
- [27] Lutz, A. M., NA31 0005.
- [28] Sobol, I. M., "The Monte Carlo Method", The University of Chicago press, 1974.

- [29] Opat, G. I., "Monte Carlo Simulation of Experiment", TRIUMF PREPRINT, TRI-77-4.
- [30] James, F., "Monte Carlo Theory and Practice", CERN-DD-80-6.
- [31] Sjöstrand, T., The Lund Monte Carlo for Jet Fragmentation and e^+e^- Physics - JETSET version 6.2, LU TP 85-10, October 1985.
- [32] Brun, R. et al., GEANT 3, Data Handling Division DD/EE/84-1, May (1986)
- [33] Longo, E. and Sestili, I., Nucl. Instr. and Methods **128**,283(1975).
- [34] Aubert, B. et al., Nucl. Instr. and Methods **176**, 195(1980).
- [35] Bock, R.K. et al., Nucl. Instr. and Methods **186**,533(1981).
- [36] Private communication, Richard Dubois, SLAC, 1986.
- [37] TASSO Collaboration, Physics Letters, Vol 86B, number 2 , Sept 1979.

Vita

Surname: **Young**

Given Names: **Eric**

Place of Birth:

Trois-Rivières, Quebec

Date of Birth:

July 28, 1963

Educational Institutions Attended:

Université Laval, P.Q.

1982 to 1985

University of Victoria, B.C.

1985 to 1988

Degrees Awarded:

B.Sc. 1985

Université Laval

Partial Copyright License

I hereby grant the right to lend my thesis (the title of which is shown below) to users of the University of Victoria Library, and to make single copies only for such users, or in response to a request from the library of any other university or similar institution, on its behalf or for one of its users. I further agree that permission for extensive copying of this thesis for scholarly purposes may be granted by me or a member of the university designated by me. It is understood that copying or publication of this thesis for financial gain shall not be allowed without my written permission.

Title of Thesis:

**A Monte Carlo Simulation of the SLD Calorimeter
to Study the Decay of the Weak Neutral Boson**



Author Eric Young

May 31, 1988